Improving Stroke Treatment Using Active and Functional Magnetic Nanomotors

by

Weijie Huang

(Under the Direction of Yiping Zhao)

Abstract

Stroke ranks at the second leading cause of death and the leading cause of disability amongst adults worldwide according to the World Health Organization. During past several decades, the use of nanotechnology based method to improve stroke treatment has attracted a lot of research attentions. Up to now, tissue plasminogen activator (tPA) is the only Food and Drug Administration proved drug for the treatment of ischemic stroke. However, the side effects such as symptomatic intracranial hemorrhages showed on some patients during tPA treatment have brought major concerns about its safety and efficacy. This dissertation focuses on the fundamental study on how to reduce the risks associated with tPA treatment by improving tPA's effectiveness using magnetic nanomotors.

When the concentration of tPA is low ($\leq 60\,\mu g\,ml^{-1}$) which is common for clinic stroke treatment, the tPA mediated thrombolysis process is a diffusion limited bio-chemical reaction. By accelerating the diffusion of tPA with rotating Ni nanomotors, we have experimentally demonstrated that the thrombolysis rate can be doubled. A theoretical hydrodynamic model is developed to reveal the fundamental physical processes. To further reduce the risks of tPA treatment, Fe_3O_4 nanorods are fabricated and loaded with 6% mass ratio of tPA and

can release tPA in several hours, and the release rate can be further accelerated by an external rotating magnetic field. This method can significantly reduce the amount of tPA administrated in a stroke treatment.

This dessication work lay a solid foundation for using magnetic nanomotors to effectively treat stroke and may benefit people who suffering thrombotic diseases.

INDEX WORDS: Magnetic nanomotor, Stroke treatment, Blood clot, Magnetic manipulation, Tissue plasminogen activator

Improving Stroke Treatment Using Active and Functional Magnetic Nanomotors

by

Weijie Huang

B.S., Beihang University, China, 2011

A Dissertation Submitted to the Graduate Faculty of The University of Georgia in Partial Fulfillment of the Requirements for the Degree

Doctor of Philosophy

Athens, Georgia

2017

Improving Stroke Treatment Using Active and Functional Magnetic Nanomotors

by

Weijie Huang

Major Professor:	Yiping Zhao
Committee:	Zhengwei Pan Qun Zhao Heinz-Bernd Schüttler Leidong Mao

Electronic Version Approved:

Suzanne Barbour
Dean of the Graduate School
The University of Georgia
August 2017

Acknowledgments

First and foremost, I would like to express my deepest gratitude to my advisor Dr. Yiping Zhao for his invaluable advice, scientific insight, and patience throughout my Ph.D studies. Without him this work would not have been possible. I would also like to thank Dr. Leidong Mao, Dr. Zhengwei Pan, Dr. Heinz-Bernd Schüttler, and Dr. Qun Zhao for serving as my advisory committee.

Additionally, I am greatly obliged to Dr. Bo Yang, Dr. Kunlin Jin, Dr. Rui Qiao, Dr. Qichuan Zhuge, Mr. Fengchang Yang, Mr. Jiangnan Hu and Mr. Shengwei Huang for the collaboration and their invaluable contribution to my work.

I owe special thanks to my wife Shayi Zhang, lovely son Jason and my parents. For their love, sacrifice, patience and constant encouragement during the most difficult phase of my Ph.D.

Finally, I would like to acknowledge many of my colleagues, both past and present for the help and insights in the research: Dr. Rui Cheng, Dr. Yizhuo He, Dr. Whitney Ingram, Dr. George Larsen, Dr. Manoj Manjare, Dr. Pradip Basnet, Dr. Kun Yao, Mr. Layne Hyer Bradley, Ms. Lu Zhu, and Mr. Steven Larson.

Table of Contents

Page

Acknowledgments iv

List of Tables vii

List of Figures viii

Chapter

1. Introduction 1

1.1 Stroke 1

1.2 Magnetic nanoparticle for medical applications 8

1.3 Fabrication and synthesis of MNRs 28

1.4 Contents of dissertation 32

2. Manipulation of Magnetic Nanorod with a Nonuniform Alternating Magnetic Field 33

2.1 Introduction 33

2.2 Experiment methods 34

2.3 Translational motion under nuAMF 37

2.4 Theoretical explanations 47

2.5 Control of the MNR motion 54

2.6 Conclusions 60

3. Improving Stroke Treatment Through Enhanced Diffusion by Rotating Magnetic Nanorods 61

3.1 Introduction 61

3.2 Experiment methods 62
3.3 A simple reaction model on thrombolysis process 68
3.4 Enhanced tPA reaction by rotating MNRs 72
3.5 Conclusion 80
4. Targeted Delivery and Improving Stroke Treatment by Magnetic Nanorod Loaded with tPA 82
4.1 Introduction 82
4.2 Experiment methods 83
4.3 tPA release experiments 86
4.4 Thrombolysis experiment with tPA loaded Fe_3O_4 MNRs 89
4.5 Conclusion 94
5. Conclusions and Future Work 96
References 98
Appendix 113
A. Cluster Tracking Program 113
B. Manipulation by Keyboards 123

List of Tables

Page

Table 1.1: Typical Reynolds number values for self-propelled objects. 15

Table 1.2: Mathematical models used to describe drug release process. 28

List of Figures

Page

Figure 1.1: Illustration of ischemic stroke, which caused by blood clots. Reprint from [3]. 2

Figure 1.2: Illustration of using surgery based method to remove blood clot. A catheter with a stent placed on its end can be inserted in an artery to mechanically remove the blood clot. Reprint from [6]. 3

Figure 1.3: Example of non-magnetic tPA nanocarriers. (a) Microbubbles took on small smooth circles under light microscope. Reprint from [23]. (b) Red fluorescence emitted by 5FAM-labeled tPA carried by the microbubbles under fluorescence microscope. Reprint from [23]. (c) SEM images of the microscale (∼2 µm to 5 µm) shear-activated nanotherapeutics (left) and the PLGA NPs (∼180 nm) used to produce them (right). Scale bar, 2 µm. Reprint from [25]. (d) A microfluidic vascular stenosis model showing how shear-activated nanotherapeutics (large spheres) should remain intact in the prestenotic region but then break up into NPs (small spheres) when they flow through a constriction (90% lumen occlusion) and can accumulate in endothelial cells lining the bottom of the channel. Reprint from [25]. 6

Figure 1.4: Example of magnetic tPA nanocarriers. (A) Typical view of the smaller magnetic biodegradable carriers containing tPA. Reprint from [33]. (b) Large magnetic biodegradable microcarriers containing tPA. Reprint from [33]. (c) TEM images of Fe_3O_4/SiO_2 core/shell NPs. Reprint from [30]. (d) tPA coated Fe_3O_4/SiO_2 core/shell NPs. Reprint from [30]. (e) Schematic representation of tPA nanocube clusters (tPA–NCs) showing two main compartments: a cluster of iron oxide nanocubes forming the nanoconstruct core; a surface coating of tPA and serum albumin, forming the external nanoconstruct layer. Reprint from [29]. (d) SEM and TEM (insert) images of tPA–NCs demonstrating a characteristic size of $\sim 150\,\text{nm}$. Reprint from [29]. 7

Figure 1.5: The hysteresis loop and magnetic properties. Reprint from [34]. . . 9

Figure 1.6: The interaction between two magnetic dipoles (a) without an EMF and (b) with an EMF. 12

Figure 1.7: Manipulating magnetic particles, helixes and chains, by (a) a static magnetic field (b) a magnetic force microscopy, (c) a current network, (d) a rotational magnetic field in liquid, (e) a combination of alternating and static magnetic fields, and (f) a rotational magnetic field on a solid surface. 13

Figure 1.8: Schematic of an artificial magnetic swimmer with a magnetic head and a helical tail achieves (a) forward and (b) backward locomotion driven by a rotational magnetic field in the (c) clockwise and (d) counter-clockwise direction. Reprint from [59] 17

Figure 1.9: (a) The nanowire motor moving forward (top) and backward (bottom) under a RMF. Images marked with "a" are the optical images of the motor, "b" are the images after 15 sec and "c" are the schematic of the magnetic swimmer. Reprint from [62]. (b) 3 µm PS bead linked to a 150 nm MNP via a flagellar filament depicting dumbbell or double-bead microswimmers. The flagellar filament linking the two beads is indicated by the arrows. Reprint from [53]. (c) Schematic representation of a flexible magnetic filament. Reprint from [63]. 18

Figure 1.10: A experimental realization of "surface walkers". Reprint from [69]. (a) The geometry of "surface walkers". (b) The experimental and simulation results for a "surface walker" driven by a RMF of 5 Hz (top) and 7 Hz (bottom), notice the disassembly of the chain. 19

Figure 1.11: Different fluids A and B are mixed together at a T-junction to flow alongside each other down the channel. The width of the channel is L and the velocity of the flow is U. 22

Figure 1.12: Schematic illustration of the hydrodynamic induced mobility by rotating MNRs. When a MNR in solution is driven by a rotational magnetic field, it will induce a creepy Stokes' flow that enhance the mobility of chemical A and B. The flow has a cylindrical hydrodynamic influence. 24

Figure 1.13: GLAD method illustration and its mechanism. (a) Schematic of OAD/GLAD: θ the angle between the substrate surface normal $\vec{N}$ and the vapor direction. The surface rotating is controlled by Motor 1 and θ is controlled by Motor 2. (b) Illustration of shadowing growth. Left: vapor begins to deposit on a flat substrate to form nucleation points. Right: as more accumulation occurs, it is restricted to the points of nucleation due to the shadowing effect, and an array of NRs forms. 29

Figure 1.14: Nanostructures fabricated by GLAD method. (a) SEM image of Iron Oxide-Capped Janus magnetic particles. Reprint from [96]. (b) A cross-section view of the fabricated SiO_2 screw structures. Reprint from [97]. (c) SEM image of a individual SiO_2 screw. Reprint from [97]. 30

Figure 1.15: Fe_3O_4 NPs synthesized using hydrothermal method. Reprint from [102]. (a) With PEG in reaction. (b) Without PEG in reaction. 31

Figure 2.1: The manipulation of a MNR using a non-uniform alternating magnetic field near a substrate surface. 33

Figure 2.2: (a) The representative SEM image of Fe_3O_4 NRs. (b) The magnetic hysteresis loop of the Fe_3O_4 NRs. (c) The SEM image of a single Ni NR. (d) An optical microscope image of a single dispersed Ni NR and a Ni Janus NP in water. 35

Figure 2.3: The experiment setup of non-uniform alternating field experiment. 36

Figure 2.4: Magnetic field calibration curve for a solenoid with a $f_H = 10\,\text{Hz}$ AC. 37

Figure 2.5: The movie frames to show the motion of MCs when a solenoid is placed at the left-hand side. (a) The movie of MCs rotating and moving. The targeted MC is marked with a red circle. The time interval between adjacent frames is 0.2 s and the scale bar indicates 50 µm. (b) The corresponding SEM image of the targeted MC in (a). (c) The zoomed-in out-of-plane rotation of a MC during one period. The size of the images in (c) is $17\,\mu\text{m} \times 17\,\mu\text{m}$, and the frame interval is 0.02 s. The cartoon illustrates the out-of-plane rotation of a MC. 38

Figure 2.6: Movie chips that showing a single Ni MNR perform translation motion with out-of-plane rotations in a $f_H = 10\,\text{Hz}$ nuAMF. (a) to (d) The movie chips of the rotation of a Ni MNR and a half Ni coated Janus bead in one period (0.1 sec). The rod is preforming out-of-plane rotating and moving towards right hand side. While the Janus bead is rotating and moving in random direction due to Brownian motion. (e) Shows the movie chip after 4 sec. An arrow is drawn to indicate the moving direction of the rod. With in 4 sec, the rod has moved about 18 µm to the right hand side while the Janus bead almost stays at same place. The scale bar: 10 µm. . . . 39

Figure 2.7: Trajectories of the MCs at three different field configurations: (a) a uniform alternating magnetic field; (b) a nuAMF generated by a single solenoid; and (c) a nuAMF produced by two solenoids. 41

Figure 2.8: The detailed analysis of the trajectory of a single MC at $f_H = 5\,\text{Hz}$ and $I_0 = 2\,\text{A}$. (a) The plots of displacement $S(t)$ and the residual $\Delta S(t)$. The straight line is a linear fit. (b) The FFT of $\Delta S(t)$. The strongest peak is at $f = 5\,\text{Hz} = 2f_H$. 42

Figure 2.9: The FFT of the width W of a moving MC for fH = (a) 5 Hz, (b) 43 Hz, (c) 83 Hz, and (d) 127 Hz. Here $I_0 = 2\,\text{A}$. The frequency peaks are indicated by different symbols: O: $2nf_H$, Δ: 120 Hz, *: f_H 43

Figure 2.10: (a) The translational speed v of MCs and (b) a single Ni NR versus different I_0. Here $f_H = 10\,\text{Hz}$. 45

Figure 2.11: (a) The plot of the translational moving speed v of different sized MCs and (b) a single Ni NR as a function of nuAMF frequency f_H. Here $I_0 = 2\,\text{A}$. 46

Figure 2.12: Statistics of the MCs' moving direction for different f_H. Black: not moving; Blue: moving towards solenoid; Red: moving away from solenoid. Here $I_0 = 2\,\mathrm{A}$ and a cluster will be classified as not moving when its speed is smaller than $1\,\mu\mathrm{m\,s^{-1}}$. 47

Figure 2.13: The translational and rotational motion of a MC driven by low-frequency nuAMF. (a) External alternating magnetic field as a function of time. (b) Force and toque analysis of a MC in an nuAMF. (c1-2) Pressure distribution on the MC surface at $t = t_1$ and t_3 moments. Initially, the magnetic moment of the MC aligns with the external $\vec{H}$. By time instant t_1, $\vec{H}$ changes to the new orientation, which is opposite to its original orientation. The MC experiences a magnetophoresis force $\vec{F}_{mp}$ pointing toward the solenoid. This $\vec{F}_{mp}$ induces a weak hydrodynamic torque $\vec{T}_{mp}$ on the MC, which drives it to rotate in the clockwise direction. Once the MC deviates from its original orientation, it experiences a magnetic torque $\vec{T}_{mp}$ caused by $\vec{H}$, which further drives its clockwise rotation. Consequently, the MC shows persistent rotation and moves away from the solenoid ($t = t_3$ and c2) as a surface walker [69] until it fully aligns with the external magnetic field $\vec{H}(t = t_4)$. 48

Figure 2.14: Simulation results of the motion of a magnetic cluster in one period of low-frequency nuAMF. (a) The external nuAMF. (b) The angle between the cluster's magnetic moment and the horizontal plane. (c) The cluster's displacement. (d) The cluster's translational velocity. 51

Figure 2.15: Evolution of the width of a magnetic cluster projected onto the horizontal plane over several periods of AC magnetic field ($f_H = 5\,\mathrm{Hz}$ or $\tau = 0.2\,\mathrm{s}$). Inset (a) show the definition of the projected width of the cluster. Inset (b) is the representative experimental result compared with simulation data. The two downward spikes correspond to the rapid alignment of the cluster with the external magnetic field once it rotates away from the 0° or 0° orientation (see **Figure 2.14(b)**). The projected width maintains its maximal value most of the time, indicating that the cluster is fully aligned with the low-frequency magnetic field studied here. 53

Figure 2.16: Effects of the amplitude of current I_0 (a) and field frequency f_H (b) of nuAMF on the translational velocity obtained from simulations. . . 54

Figure 2.17: (a) Illustration of the trajectory of a MNR move under the nuAMF. (b) The definition of the directionality. 55

Figure 2.18: Experiment results of continues signal. (a) Histogram of the angle θ and the normal distribution fitting. (b) Plot of D_d verse f_H. 56

Figure 2.19: (a) Simulation of the D_d at different v. (b) Experiment result of D_d (black), and translational motion speed v (blue) verse f_H. 57

Figure 2.20: Theoretical estimation of the manipulation resolution under different f_H. 58

Figure 2.21: Motion study with noncontinuous nuAMF signal. (a) Illustration of the noncontinuous sinusoidal signal by applying a window function to a continues sinusoidal signal. (b) Plot of the motion speed v verse the duration of the signal t_s. 59

Figure 2.22: Write letters using program controlled signals with $f_H = 20\,\mathrm{Hz}$, $t_s = 0.2\,\mathrm{s}$, and $t_0 = 0.5\,\mathrm{s}$. 60

Figure 3.1: Schematic view of nanorod enhanced thrombolysis in fluidic channels. The Nickel MNR are dispersed in tPA solution and activated by a rotational magnetic field at the vicinity of a clot in a PDMS channel. The mass transport of tPA molecules are directly accelerated by the hydrodynamic flows induced by rotating MNRs. 61

Figure 3.2: Nickel rods fabrication process using OAD and convective self-assembly methods. (a) Schematic process of fabrication indicated in clockwise direction: self-assembled monolayer of polystyrene beads on a cleaned silicon wafer; uniform nickel rods grown on beads using OAD method; rods washed into suspension of PVP. (b) Side view of nanorods on silicon substrate; (c) A single nanorod with a polystyrene bead; (d) Rods suspended in PVP (MW = 40 kDa) solution, forming a matrix of known concentration. 63

Figure 3.3: Left: *In-vitro* experimental setup consisting of the magnetic field generator, light pad, PDMS plate, and a microscope. Right: a zoom in image of a PDMS channel with clot in experiment. 64

Figure 3.4: Fabricating clot inside PDMS channels. (a) PDMS channels plugged with clot, shown as light-yellow segments. (b) A clot pricked from a PDMS channel after fully reacted. 65

Figure 3.5: Data treatment process of *in-vitro* experiments. (a) Original image of a Dye+MNR channel at the beginning of the experiment with x-y coordinate definition. (b) The individual RGB color channel of the original image. (c) The calibration curve of the grayscale of the green channel G *vs.* RDB concentration c. 67

Figure 3.6: Simplified schemes of tPA mediated thrombolytic reaction on clot surface: (i) tPA and plasminogen molecules (PLG) diffuse to clot surface and bind to lysine sites. (ii) PLG molecules on the fibrin surface are activated into plasmin (PLM) by the neighboring tPA molecules. PLM molecules start to cleave the local fibrin fiber into soluble products (P). (iii) Lysis molecules P leave fibrin surface and expose new lysine sites. 69

Figure 3.7: The clot boundary moving speed v_{T} versus the tPA concentration C_{tpa} 70

Figure 3.8: Results of *in-vitro* experiments: (a) A representative PDMS channel structure, where "X" represent different mixture. (b) Video clips of green-channel images at the liquid/clot interface in "D", "R", "T", "R+T" channels (from top to bottom), at different thrombolysis time t = 40, 80, 120, and 160 min (from left to right), respectively. (c) The plot of gray scale versus PDMS channel location in (b). (d) Clot boundary moving speed v_T and v_{R+T} versus MNR concentration C_{Rod}. The blue solid square represents v_T and the red solid circle represents v_{R+T}. The pink dash line is a guide to eyes, and black dash-point curve is a fitting curve based on the proposed theoretical model. 73

Figure 3.9: Mechanical interaction between MNRs and clot. (a) Change rate of dye concentration along the clot region. (b) Plot of the position of clot interface versus time t. 75

Figure 3.10: Locally enhanced thrombolysis through concentrating Nanorods: (a) Video clips of dye-solution/clot interface evolution in one "T" and two "R+T" channels with $C_{\mathrm{Rod}} = 1\,\mathrm{mg\,ml^{-1}}$ with a nail presented in the magnetic field. Red circles indicate locations of the concentrated MNRs. (b) Each channel is horizontally divided into 5 sub-channels of equal width, and the moving speed of liquid/clot interface in each sub-channel is labeled as v_1, v_2, v_3, v_4, and v_5, from bottom to top. (c) The local clot lysis rate of three channels. Due to the conjugation of MNR at the top right corner in two "R+T" channels, the lysis rate is increased from v_1 to v_5. The enhanced thrombolysis factor β can be up to 1.75 which is comparable to at $C_{\mathrm{Rod}} = 5\,\mathrm{mg\,ml^{-1}}$ shown in **Figure 3.8(d)**. 77

Figure 3.11: *In-vivo* experimental setup. (a) Schematic illustration of the apparatus. (b) Magnetic field distribution between two permanent magnets at different separations marked on the top of each image. 79

Figure 3.12: Enhanced thrombolysis by active MNRs is demonstrated in mice embolism model. (a) *In-situ* experimental setup; (b) Thrombolysis evaluation in the right femoral vessels of mice belonging to three groups associated with different administrations. The green arrows indicate the inducted region in the femoral vessels of C57/BL6 mice. 80

Figure 4.1: Schematic illustration of using biocompatible Fe_3O_4-MNRs conjugated tPA (MNR-tPA) to target blood clots under magnetic guidance. Blood clots can be mechanically pored and loosened by the Fe_3O_4-MNRs under a RMF, and lysed biochemically by tPA released from MNRs, which thus improve thrombolysis beyond the efficiency currently observed for tPA. . . . 82

Figure 4.2: (a) A representative SEM image of as-deposited Fe_2O_3 nanorods. (b) A SEM image of an individual Fe_3O_4 nanorod obtained after annealing. Insert: a TEM image of a Fe_3O_4 nanorod. (c) The XRD pattern of Fe_3O_4 nanorods. (d) A magnetization curve of Fe_3O_4 nanorods. 84

Figure 4.3: A schematic diagram showing the surface modification of Fe_3O_4 MNRs with APTES (step 1), activation with glutaraldehyde (step 2), and immobilization of tPA (step 3). 85

Figure 4.4: The plot of the accumulated tPA concentration C_{tPA} versus release time t. $C_{\mathrm{Rod}} = 1\,\mathrm{mg\,ml^{-1}}$ for all experiments. Each data point was an average from 3 repeated experiments. 87

Figure 4.5: The plot of clot lysis speed v_T versus the MNR concentration $C_t extrod$ with and without a RMF (20 Hz, 3 mT). The dashed line represents the reference tPA speed v_T^R at $C_{\mathrm{tPA}} = 20\,\mu\mathrm{g\,ml^{-1}}$ and the shadow area represents the standard derivation, and the dash-dotted line represents the maxima saturated tPA speed v_T^M at $C_{\mathrm{tPA}} = 180\,\mu\mathrm{g\,ml^{-1}}$. Each data point was an average from 3 repeated experiments. 90

Figure 4.6: The plot of clot lysis time T_l versus the tPA loaded MNR concentration C_{rod} using PE50 catheter based blood clot model under a RMF (20 Hz, 40 mT). 92

Figure 4.7: The plot of lysis efficiency in the PE 50 catheter-based blood clot model under different thrombolytic condition for 60 min under a RMF (20 Hz, 40 mT): A - normal saline, B - $400\,\mu\mathrm{g\,ml^{-1}}$ MNRs in normal saline, C - $40\,\mu\mathrm{g\,ml^{-1}}$ tPA solution, and D - $400\,\mu\mathrm{g\,ml^{-1}}$ tPA loaded MNRs in normal saline. The insert shows a photo after 60 min in the PE50 catheter-based blood clot model. 93

Figure A.1: (a) The example of a tracked movie frame with a $f_H = 5\,\mathrm{Hz}$, $I_0 = 2\,\mathrm{A}$ driven field. (b) Tracked trajectories for selected clusters. The black circle marks the initial position. 114

Figure B.1: Illustration of motion control system. Orange color marks the components that are activated when user press 'Up' key. 123

Figure B.2: The flow chart of motion control program. 124

Chapter 1

Introduction

1.1 Stroke

1.1.1 What is stroke

Stroke is a disease that occurs when the supply of blood to an area of brain is either interrupted or reduced. It has ranked to be the second leading cause of death and the leading cause of adult disability worldwide according to the World Health Organization [1]. There are two types of stroke, hemorrhagic and ischemic. Hemorrhagic strokes are less common, they contribute to about 15% of all strokes, but are responsible for about 40% of all stroke deaths. A hemorrhagic stroke is most commonly caused by a blood vessel inside the brain that bursts and leaks blood into surrounding brain tissue. The leaked blood causes part of the brain functions incorrectly and puts pressure on brain cells. People with high blood pressure and aging blood vessels are more likely to suffer from this type of stroke. Ischemic stroke, as an illustration shown in **Figure 1.1**, is the most common form of stroke, accounting for around 85% of strokes. This type of stroke is caused by blockages or narrowing of the arteries that provide blood to the brain. When this happens, brain cells are deprived of oxygen and begin to die. The blockage is usually caused by obstructive blood clot made of aggregated platelets and blood cells surround with meshes of cross-linked fibrin protein [2]. In this dissertation work, we will focus on this type of stroke only.

Strokes need to be diagnosed and treated as quickly as possible in order to minimize brain damage. This is because neurons and other brain cells require oxygen and glucose delivered through the blood in order to function and survive. A few minutes of oxygen deprivation is enough to kill millions of neurons. Statistically, when stoke occurs, about one-

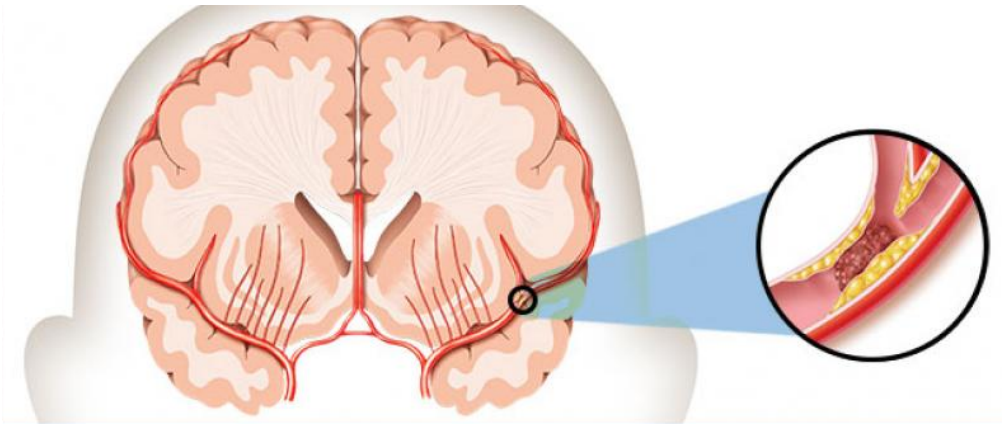

Figure 1.1: Illustration of ischemic stroke, which caused by blood clots. Reprint from [3].

third of patients fail to survive the event, and even among those who survive stroke, 90% of them suffer permanent deficits [4].

1.1.2 Challenges for current ischemic stroke treatment

The key to treat ischemic stroke, which is most likely caused by a blood clot, is to break apart the blocking clot within the first few hours after stroke has occurred. For the blood clot formed in relatively large blood vessels, such as an artery, surgery based endovascular mechanical thrombectomy has been used to mechanically remove the clot. For example, the intra-arterial fibrinolysis as shown in **Figure 1.2**, which is done by inserting a stent placed on the end of a catheter threaded through an artery to the clot site. When the catheter reaches the clot, the stent is opened and inserted in the clot. And once the stent grabs the clot, the catheter is removed along with the attached clot. This method has been found to significantly improve outcomes in patients with acute ischemic stroke [5].

Besides mechanically remove the blood clot, another acute therapy of ischemic stroke requires infusion of a thrombolysis drug named tissue plasminogen activator (tPA or alteplase) through a catheter placed within the blocked vessel. This drug, tPA, is initially used to treat heart attacks. In the late 1980s, the National Institute of Neurological Diseases and Stroke laid the plans for the first trial of using tPA to treat acute ischemic stroke. This is because

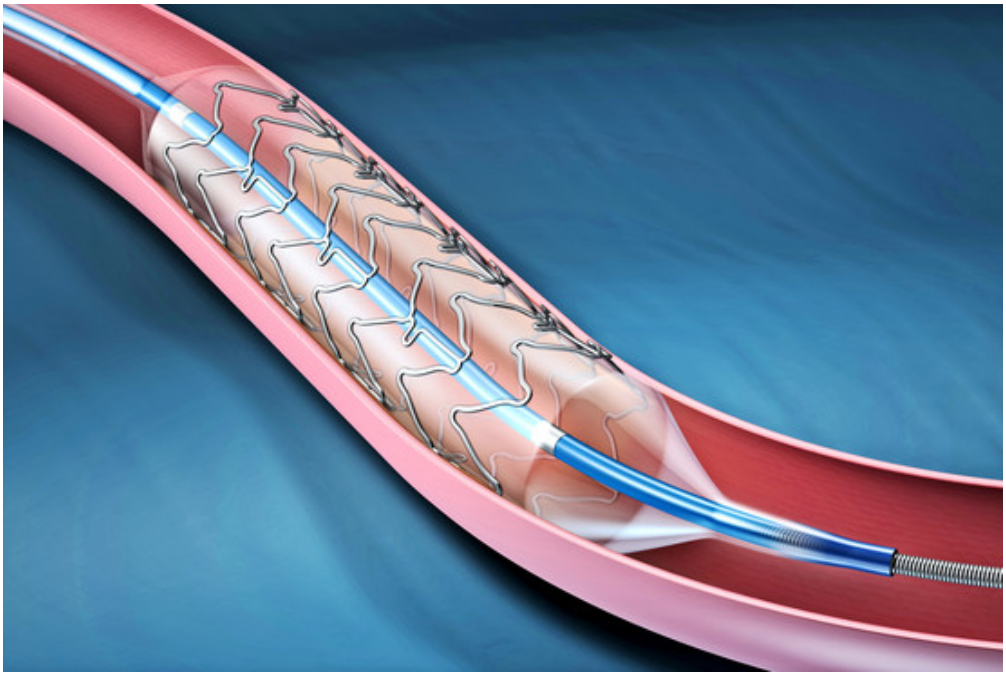

Figure 1.2: Illustration of using surgery based method to remove blood clot. A catheter with a stent placed on its end can be inserted in an artery to mechanically remove the blood clot. Reprint from [6].

tPA can activate plasminogen to plasmin, which then break the cross-linked fibrins that provide mechanical strength to maintain the structure of a blood clot. After testing over 70 agents in clinical trials, the Food and Drug Administration (FDA) finally approved tPA for use against acute stroke in 1996. Till today, tPA is the only FDA approved thrombolytic agent to treat stroke and has been successfully used in many clinical applications. While the tPA treatment of blood clot is considered safe, side effects showed on some patients have brought the major concerns about the safety and the efficacy of tPA treatment. It has been reported that, in about 6-7% cases, the usage of tPA can cause symptomatic intracranial hemorrhages (SIH) because tPA is free to diffuse throughout the body [7]. SIH may lead to death if it is left unattended. And in about half cases, the tPA fails to lyse the clot and recanalize the middle cerebral artery [8]. As a result, tPA treatment is rarely suitable for ischemic stroke patients and is used only on about 1% to 2% of them [9]. Furthermore, the

intravenous use of tPA to dissolve clots appears to be effective only within about the first 4 - 5 hours after the initial onset of symptoms [10, 11]. The risk of tPA-related hemorrhage is significantly increased if tPA is administrated over 3 hours after stroke, which limits the use of this drug in therapeutics [11, 12]. Furthermore, these methods are only for intracranial large-vessel occlusion and unable to remove more distal clots, and therefore are unable to be applied to the majority of stroke patients. In addition, they require special equipment and technical expertise that exists only in major medical centers. Clearly, in order to improve the tPA therapy, new strategies with better drug safety and improved drug effectiveness are needed.

1.1.3 Nanotechnology for stroke treatment

So far, dose control and effectiveness promotion of tPA are the main approaches to reduce the risks of SIH associated with the stroke treatment. This is because according to the guidelines for the management of patients with acute ischemic stroke published by the American Heart Association Stroke Council (2007) [11], the dosing regimen of intravenous tPA treatment is $0.9\,\mathrm{mg\,kg^{-1}}$ (maximum of 90 mg per treatment) [13]. And the ratio of blood volume to body weight ranges 62-86 $\mathrm{ml\,kg^{-1}}$ [14]. Thus, the average tPA concentration used for acute stroke treatment is ranging from 10.5 to 14.5 $\mathrm{\mu g\,ml^{-1}}$ during the intravenous administration, which is consistent to the statistic results [15, 16]. According to previous studies [17–22], the clot lysis process under usual clinically administrative tPA concentration is a diffusion-limited process or a mass-transport limited process depending closely on the tPA bulk concentration. Thus, by improving tPA's effectiveness, less tPA would be administrated in a stroke treatment which then reduces the risks associated with tPA.

A few promising approaches have been developed recently. In particular, nanocarrier drug delivery is the most widely used method because of its advantages in accurate dose control by nano synthesis and precise target by dynamic delivery system [11]. For example, studied have shown that biodegradable nano-liposomes capsuled with tPA are able to control the

drug dosage, prolong the circulation lifetimes of tPA [23], and even enhance the thrombolysis with the help of ultrasound [24] as shown in **Figure 1.3(a)** and **(b)**. tPA-loaded liposomes offer several unique advantages including cheap, easy to fabricate, and high tPA loading ratio. Clinic trials showed that tPA liposomes injected into the upper blood stream of the clot site were able to target the clot and release tPA locally. Beside liposomes, another nano drug carrier called "shear-active nanotheraputics" has been developed to target delivery of tPA by taking the advantage of the distortion of blood stream caused by the clot itself [25]. This drug carrier is a biocompatible and biodegradable poly-lactic-co-glycolic-acid (PLGA) micro aggregates that composed of tPA-coated nanoparticles (NPs) as shown in **Figure 1.3(c)**. The micro aggregates are able to hold the NPs together in normal blood stream; while under high shear-rate blood flow, they break and release NPs due to the presence of the clot as illustrated in **Figure 1.3(d)**. However, there are a few limitations of the method, just like other organic nanocarrier based methods. First is the lack of active targeting strategies since the transportation of drug carriers is depend on the blood flow. If the blood vessel is completely blocked and no blood can flow though, the efficiency of these methods would be greatly compromised. Second is unable to enhance the clot lysis rate unless increasing local tPA concentration. In addition, non-magnetic NPs coated by both thrombolytic enzymes and fibrin-specific ligands not only can deliver the drug to the fibrin, but also can cover the clotting surface to form a thrombin inhibiting coating that could theoretically further reduce thrombus formation as the particles continues to bind onto the thrombin [26].

To overcome those limitations, inorganic nanocarriers, especially magnetic nanocarriers, have been developed to target deliver thrombolysis drug to the clot site and interact with the fibrins locally with the help of an external magnetic field (EMF). In most cases, Fe_3O_4 or γFe_2O_3 NPs are preferred due to their strong magnetic properties and good biocompatibility [27, 28]. Several studies reported that Fe_3O_4-based nanocarriers were able to load and deliver tPA [29–32]. For instance, the magnetic nanocarriers were synthesized by encapsulating

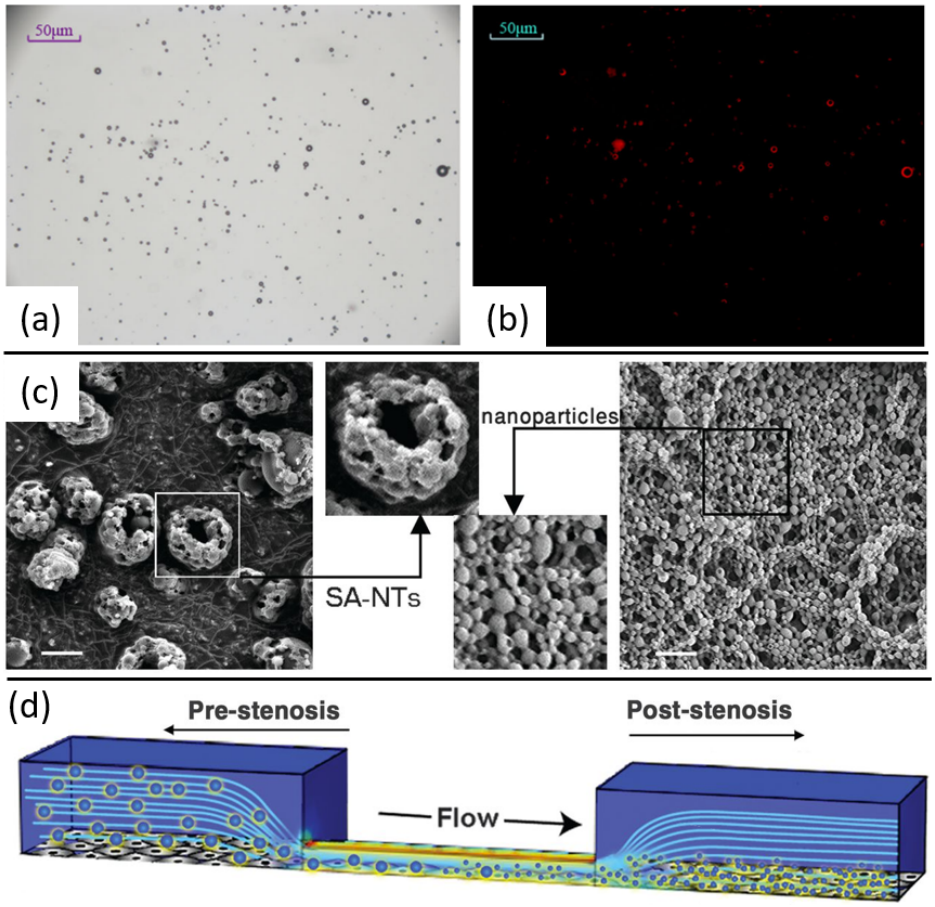

Figure 1.3: Example of non-magnetic tPA nanocarriers. (a) Microbubbles took on small smooth circles under light microscope. Reprint from [23]. (b) Red fluorescence emitted by 5FAM-labeled tPA carried by the microbubbles under fluorescence microscope. Reprint from [23]. (c) SEM images of the microscale (∼2 µm to 5 µm) shear-activated nanotherapeutics (left) and the PLGA NPs (∼180 nm) used to produce them (right). Scale bar, 2 µm. Reprint from [25]. (d) A microfluidic vascular stenosis model showing how shear-activated nanotherapeutics (large spheres) should remain intact in the prestenotic region but then break up into NPs (small spheres) when they flow through a constriction (90% lumen occlusion) and can accumulate in endothelial cells lining the bottom of the channel. Reprint from [25].

both Fe_3O_4 and tPA using biodegradable matrix, such as polyethylene glycol–polylactic acid copolymer [33] as shown in **Figure 1.4(a)** and **(b)**. One advantage of Fe_3O_4 nanocarriers is that their surfaces can be functionalized or modified by drugs. Chen, *et al.* reported the Fe_3O_4/SiO_2 core/shell NPs loaded with tPA possessed an improved environmental stability and biocompatibility due to the SiO_2 coating [30] as shown in **Figure 1.4(c)** and **(d)**. Their

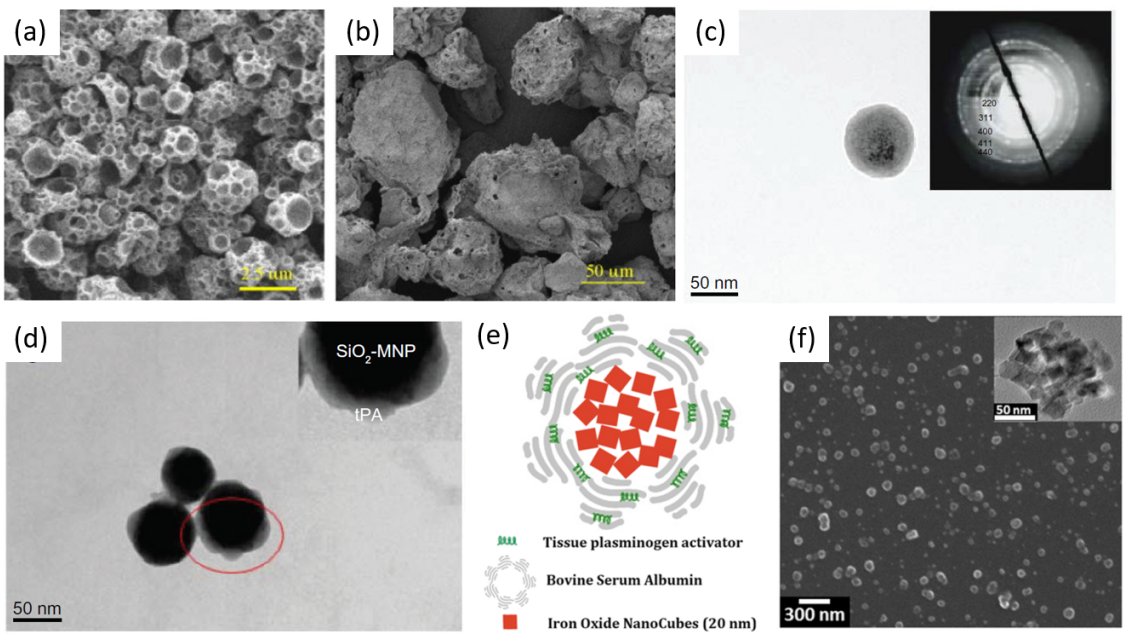

Figure 1.4: Example of magnetic tPA nanocarriers. (A) Typical view of the smaller magnetic biodegradable carriers containing tPA. Reprint from [33]. (b) Large magnetic biodegradable microcarriers containing tPA. Reprint from [33]. (c) TEM images of Fe_3O_4/SiO_2 core/shell NPs. Reprint from [30]. (d) tPA coated Fe_3O_4/SiO_2 core/shell NPs. Reprint from [30]. (e) Schematic representation of tPA nanocube clusters (tPA–NCs) showing two main compartments: a cluster of iron oxide nanocubes forming the nanoconstruct core; a surface coating of tPA and serum albumin, forming the external nanoconstruct layer. Reprint from [29]. (d) SEM and TEM (insert) images of tPA–NCs demonstrating a characteristic size of $\sim 150\,\text{nm}$. Reprint from [29].

ex-vivo study suggested that when an external rotating magnetic field (RMF) was applied, NPs could penetrate into blood clots to enhance the thrombolytic efficiency. However, *in-vivo* thrombolysis remains largely unexplored. Recently Decuzzi's group found that superparamagnetic Fe_3O_4 nanocube coated with a mixture layer containing tPA and bovine serum albumin could improve clot dissolution rate by ∼100-fold increase in , when a 259 kHz high frequency magnetic field was applied [29] as shown in **Figure 1.4(e)** and **(f)**. This is because of the local heating effect of the nanocubes after absorbing the energy provided by the alternating magnetic field. However, it remains unclear whether this approach can be applied in clinic.

Compared to normal clinic surgery treatments, the nanocarrier method can be applied

to small brain blood vessels and only requires a much smaller amount of tPA drug because the drug can be greatly localized. As a result, the drug's side-effect is expected to be reduced.

1.2 Magnetic nanoparticle for medical applications

As we have just discussed, Magnetic nanoparticle (MNP) can be used as drug carrier to target deliver drug. Compare to non-magnetic drug carriers, the MNP drug carrier has a advantage that can be controlled using an EMF. Such control can offer extra mechanisms to enhance the drug's efficiency. For example, by enhancing diffusion or generating heat locally. Thus, it is very important to understand the fundamental physics of a MNP moving under a EMF in a liquid environment. This section will briefly introduce the magnetic interaction between MNPs and their hydrodynamics in a liquid environment.

1.2.1 Magnetic nanoparticle property and applications

Magnetic materials can be magnetized due to the alignment of their net magnetic moments along the direction of an EMF $\vec{B}$,

$$\vec{B} = \mu_0(\vec{H} + \vec{M})\,, \tag{1.1}$$

where μ_0 is the magnetic permeability of vacuum, $\vec{H}$ is the magnetic field, and $\vec{M}$ is the magnetization (magnetic moment per volume). Generally, the magnetic materials can be divided into two categories: paramagnetic and ferromagnetic due to the coupling strength between the neighboring magnetic moments. For paramagnetic materials, the coupling is weak so that the degree of the alignment of the magnetic moments decreases due to the thermal agitation when the magnetic field is removed. It's magnetization $\vec{M}$ is linearly proportional to the applied EMF,

$$\vec{M} = \chi\vec{H}\,, \tag{1.2}$$

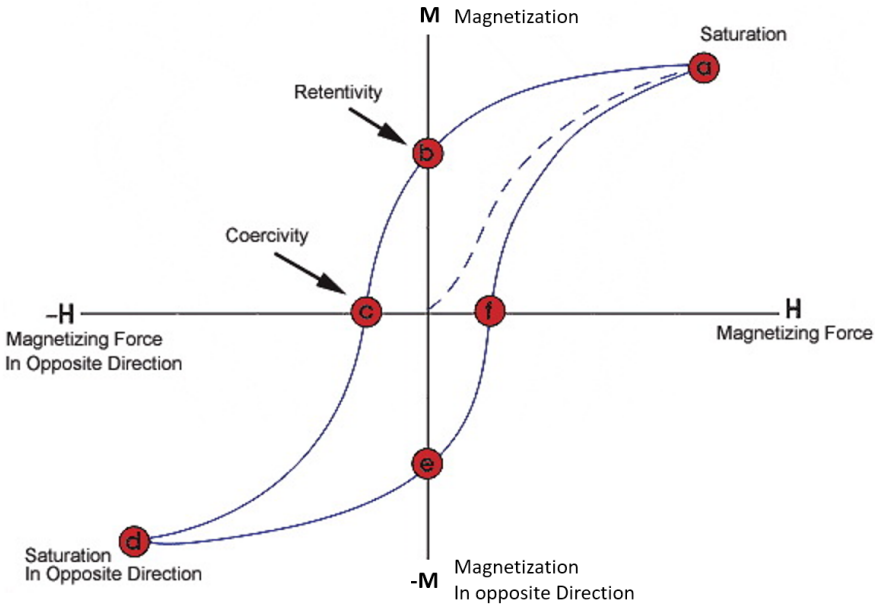

Figure 1.5: The hysteresis loop and magnetic properties. Reprint from [34].

where χ is a dimensionless parameter known as the magnetic susceptibility. Combining Equations (1.1) and (1.2), one can have,

$$\vec{B} = \mu \vec{H}\,, \tag{1.3}$$

where $\mu = \mu_0(1+\chi)$ is the magnetic permeability of the material. Equation (1.3) gives the relationship between two notations of the magnet field: $\vec{B}$ in a unit of magnetic flux density (teslas, symbol: T) and $\vec{H}$ in a unit of magnetic field strength (amperes per meter, symbol: $\mathrm{A\,m^{-1}}$).

For ferromagnetic materials, the coupling effect is strong so that the magnetic moments remain aligned even if the magnetic field is removed. Apparently, χ of both materials is larger than zero, but ferromagnetic materials normally have a larger χ. The relationship between $\vec{M}$ and EMF $\vec{H}$ is not linear when the field strength is a hysteresis loop is observed as **Figure 1.5**. The dashed line from origin to point (a) represents the initial magnetization, (a)-(b)-(c)-(d) represents the demagnetization, and (d)-(e)-(f)-(a) represents the magnetization

of a ferromagnetic material. The absolute value of the magnetization $\vec{M}$ at point (a) or (d) is called the saturated magnetization M_s. $m_s = M_s/m$ is the saturated magnetization per unit mass which is often used to characterize the magnetic property of materials during the magnetization and demagnetization process. When the EMF is zero, for example at points (b) and (e), the magnetization remained in a material is known as the residual magnetization M_0. The EMF at points (c) and (f), known as the material's coercivity H_c, represents the amount of magnetic field in reverse direction which must be applied to flip the magnetization of a magnetic material. The slope of the curve at these two points is the magnetic susceptibility χ. The ferromagnetic materials, such as iron, nickel, cobalt and some rare earths like gadolinium, are most widely used for the fabrication of magnetic particles in a colloidal system.

When the particles made of ferromagnetic materials (such as iron oxide) are small enough ($< 10\,\text{nm}$), their magnetizations can be continuously flipped up and down in an extremely short period of time due to the influence of thermal fluctuation in the absence of an EMF. On average, the residual magnetization of the particles appears to be zero. When an EMF is applied, the particles will be magnetized with the same χ as the ferromagnetic material. Such a phenomenon is called "superparamagnetic" and a more elaborate discussion can be found in Ref. [35].

When an EMF is applied to a magnetic particle (MP), both magnetic force $\vec{F}_m$, and the magnetic torque $\vec{\Gamma}_m$ could be created. A general expression for the magnetic force $\vec{F}_m$ on a suspended MP subjected to a magnetic field $\vec{B}$ is [36],

$$\vec{F}_m = V\left[\left(\vec{M}_p - \vec{M}_f\right)\cdot\nabla\right]\vec{B}\,, \tag{1.4}$$

where V is the volume of the particle, $\vec{M}_p$ is the magnetization of the particle, $\vec{M}_f$ is the magnetization of the carrier liquid surrounding the particle if the liquid can also be magnetized, such as a ferrofluid or a magnetic salt solution. According to Equation (1.4), the magnetic

force induced by a magnetic field on a single particle is always parallel (or anti-parallel) to the field gradient depending on the sign of $\vec{M}_p - \vec{M}_f$. When $\vec{M}_p - \vec{M}_f > 0$, the direction of $\vec{M}_f$ is pointing towards the field maxima and the associated motion of the particle induced by this force is known as "positive magnetophoresis". When $\vec{M}_p - \vec{M}_f < 0$, the direction of $\vec{M}_f$ is pointing towards the field minima and the motion of the particle is known as "negative magnetophoresis". There is no magnetic force induced on the particle when $\vec{M}_p - \vec{M}_f = 0$.

For a ferromagnetic particle that has a residual magnetization due to the strong coupling effect between neighboring magnetic moments, when applying a magnetic field in an arbitrary direction the MP has a tendency to rotate to align its magnetic moment towards the direction of the magnetic field, which is driven by a magnetic torque $\vec{\Gamma}_m$,

$$\vec{\Gamma}_m = V\vec{M}_p \times \vec{B}\,. \tag{1.5}$$

Here, we assume $\vec{M}_f = 0$. Thus, the magnetic torque drives the particle to rotate until $\vec{M}_p$ is aligned with $\vec{B}$.

MPs will also attract each other to form magnetic clusters (MCs) due to the strong magnetic dipole-dipole interaction. **Figure 1.6** illustrates the interactions between two identical MPs of magnetic moment $\vec{m}_1$ and $\vec{m}_2$ ($m_1 = m_2 = VM_p$) with and without an EMF. When the magnetic field is off (**Figure 1.6(a)**), the magnetic energy E_m between two MPs is given by [36],

$$E_m = -\frac{\mu_0 m_1 m_2}{4\pi r^3}\left[\frac{1}{2}\cos\left(\theta_1 - \theta_2\right) + \frac{3}{2}\cos\left(\theta_1 + \theta_2\right)\right], \tag{1.6}$$

where $\mu_0 = 4\pi \times 10^{-7}\,\mathrm{H\,m^{-1}}$ is the permeability of free space, θ_1 and θ_2 are the included angle of $\vec{m}_1$, $\vec{m}_2$ with respect to $\vec{r}$. From Equation (1.6), the sign of E_m depends on the relative orientation of m_1 and m_2, and the system is most stable for $\theta_1 = \theta_2 = 0$ since E_m reaches its minimal value. Once the magnetic moments are aligned, *i.e.*, $\theta_1 = \theta_2 = 0$,

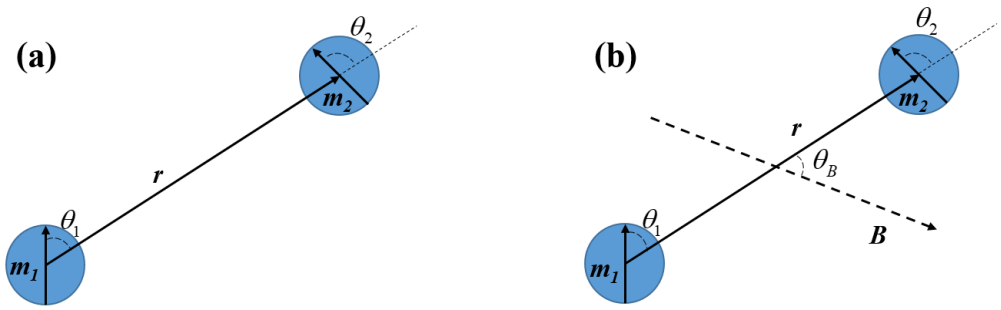

Figure 1.6: The interaction between two magnetic dipoles (a) without an EMF and (b) with an EMF.

E_m decreases rapidly with r, which suggests an irreversible aggregating process between two particles. However, without any other external stimulation, in a liquid environment this magnetic interaction can be counter-balanced by the thermal fluctuation of the particle system, *i.e.*, the Brownian motion. A dimensionless parameter λ, defined as the ratio of the magnetic energy to the thermal energy of the particle system, is used to characterize the possibility of MP aggregation [36],

$$\lambda = \frac{\mu_0 V M_p^2}{12 k_B T} \,. \tag{1.7}$$

Here, T is the temperature and k_B is the Boltzmann constant. When $\lambda > 1$, the system is not stable since the MPs will start to aggregate due to the relatively strong magnetic interaction. When $\lambda < 1$, the magnetic interaction between particles is relatively weak, then the particle system could be stable. Apparently, the stability of the MPs increases when the volume of the individual particles decreases.

When subjected to a uniform EMF in the direction of θ_B, as shown in **Figure 1.6(b)**, there is an additional magnetic energy E_B of the system induced by the magnetic interaction between the magnetic moments (m_1 and m_2) and $\vec{B}$,

$$E_B = \sum_{k=1}^{2} m_k B \left[1 - \cos\left(\theta_B - \theta_k\right)\right] . \tag{1.8}$$

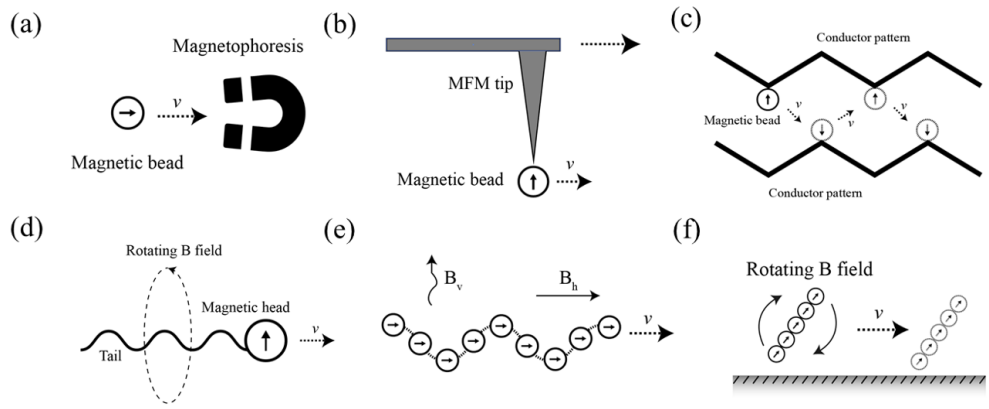

Figure 1.7: Manipulating magnetic particles, helixes and chains, by (a) a static magnetic field (b) a magnetic force microscopy, (c) a current network, (d) a rotational magnetic field in liquid, (e) a combination of alternating and static magnetic fields, and (f) a rotational magnetic field on a solid surface.

According to Equation (1.8), E_B decreases to 0 when both the m_1 and m_2 align with $\vec{B}$.

The EMF can be used to manipulate MNPs. Such a manipulation method is called magnetophoresis [37]. Compare to other manipulation mechanism, for example dielectrophoresis [38–40], magnetophoresis is a safer and better choice for manipulating biological MNPs because the magnetic field can easily permeate most mediums, including animal tissues, without causing trouble. Due to this fact, magnetic manipulation is suitable in many biological applications such as drug, gene, and radionuclide delivery [41, 42]. Depending on the magnetic field properties, magnetophoresis can be categorized as static field manipulation (SFM) or dynamic field manipulation (DFM). SFM utilities the magnetic force on a magnetic particle generated by a magnetic field gradient as shown in **Figure 1.7(a)** to **(c)**. The mechanism of SFM is through the magnetic interaction between the MNP and the EMF (Equation (1.4)). For example, Nam, *et al.* have reported the usage of a non-uniform static magnetic field to manipulate MNPs bonded with prostate-specific antigen to achieve high sensitivity of protein detection as shown in **Figure 1.7(a)** [43]. A tip of magnetic force microscope (MFM) [44–46] or similar devices can generate a static local non-uniform magnetic field to trap a magnetic object in fluids as shown in **Figure 1.7(b)**. The object can be transported by moving the

MFM tip and then released by turning off the magnetic field when it arrives at the target location. The other SFM approach which is suitable for "lab-on-a-chip" devices is to generate a series of patterned magnetic field gradients by micro-scaled current conductors (zig-zag patterns or O-ring grids) with a programmed sequence of current signals (**Figure 1.7(c)**) [47–51]. The magnetic object could be transported from one field gradient to its neighbor by a sequence of trap-release steps. In addition, due to a coupling between the rotation of a gourd-shaped magnetic particle around its short axis and the translational displacement along the vertical direction in cholesteric liquid crystal, the height of the particle can be manipulated via a static magnetic field [52].

1.2.2 Low Reynolds number hydrodynamics

One disadvantage of SFM is that the devices are usually costly and complicated. To overcome this limitation, DFM has been developed in recent years as shown in **Figure 1.7(d)** to **(f)**. This manipulation method is based on the fact that a magnetic dipole will be aligned almost instantaneously with the EMF. Thus, a magnetic particle will rotate under a low frequency rotary or oscillating magnetic field. With a specifically designed particle shape and field configuration, the induced hydrodynamic effect of the magnetic induced rotation/oscillation could be converted into a translational motion [53–56]. To understand the mechanism of DFM manipulation, we need first to understand the hydrodynamics of a particle in low Reynolds number environment. The governing equation to describe the velocity field of a viscous incompressible fluid (a Newtonian fluid) is the Navier-Stokes equations:

$$\begin{aligned} \nabla \cdot \vec{u} &= 0\,, \\ \rho\left(\frac{\partial \vec{u}}{\partial t} + (\vec{u}\cdot\nabla)\,\vec{u}\right) &= -\nabla p + \eta\nabla^2\vec{u} + \vec{f}\,. \end{aligned} \tag{1.9}$$

The first equation represents the conservation of mass and the second equation essentially is the continuum version of Newton's second law $\vec{F} = m\vec{a}$ on a unit volume element of an

Table 1.1: Typical Reynolds number values for self-propelled objects.

	Reynolds number
A large whale swimming at $10\,\mathrm{m\,s^{-1}}$	300 000 000
An adult swimming at $1\,\mathrm{m\,s^{-1}}$	1 800 000
A tuna swimming at $1\,\mathrm{m\,s^{-1}}$	200 000
A larva, 0.3 mm long, swimming at $1\,\mathrm{mm\,s^{-1}}$	0.3
A bacterium swimming at $10\,\mu\mathrm{m\,s^{-1}}$	0.000 01

incompressible fluid with a moving velocity $\vec{u}$, pressure p, viscosity η, fluid mass density ρ, and external force (for example, gravity) per unit volume $\vec{f}$. The left hand side of the second equation is the acceleration terms and forces are on the right hand side.

Reynolds number (Re) is a dimensionless number that measuring the relative importance of the inertial term $\rho(\vec{u}\cdot\nabla)\vec{u}$ and viscous term $\eta\nabla^2\vec{u}$ in Equation (1.9), which is defined as,

$$\frac{\rho(\vec{u}\cdot\nabla)\vec{u}}{\eta\nabla^2\vec{u}} \sim \frac{UL\rho}{\eta} \equiv Re\,, \tag{1.10}$$

where L is a typically length scale over which the flow varies, and U is a typical scale of the velocity. The typical Reynolds number values for self-propelled objects in water are shown in **Table 1.1**. If $Re \ll 1$, and the velocity of flow is slow, then we can neglect the inertial terms and drop the external force, Equation (1.9) will reduce to:

$$\begin{aligned} \nabla\cdot\vec{u} &= 0\,, \\ -\eta\nabla^2\vec{u} + \nabla p &= 0\,. \end{aligned} \tag{1.11}$$

Equation (1.11) is called Steady Stokes equations and flows governed by Equation (1.11) are also called creeping flows. In such liquid environment, a moving particle will experience a hydrodynamic drag force $\vec{F}_h$ or/and torque $\vec{\Gamma}_h$. Differing from the volume dependent $\vec{F}_m$

and $\vec{\Gamma}_m$, the $\vec{F}_h$ and $\vec{\Gamma}_h$ are surface effects induced by the interactions between the particle and the fluid. Thus, the shape of the particle has a great effect on $\vec{F}_h$ and $\vec{\Gamma}_h$. By solving Equation (1.11), the hydrodynamic force and torque on a spherical particle can be expressed as [57],

$$\begin{aligned} \vec{F}_h &= -\,3\pi\eta D_p \left(\vec{U}_p - \vec{U}_f\right) , \\ \vec{\Gamma}_h &= -\,\pi\eta D_p^3 \vec{\Omega} , \end{aligned} \tag{1.12}$$

where D_p is the diameter of the particle, $\vec{U}_p$ and $\vec{U}_f$ are the translational velocity of the particle and the fluid, and $\vec{\Gamma}$ is the angular velocity of the particle. Since in most cases the translational and the rotational speed of the particle is small, and the Reynolds number of the particle-fluid system $Re \ll 1$, the inertia effect can be neglected. Therefore, the translational and rotational motions of the particle are determined by the balance between magnetic and hydrodynamic forces and torques. Force and torque on a spherical particle can be expressed as [57],

$$\begin{aligned} \vec{F}_h + \vec{F}_p &= 0 , \\ \vec{\Gamma}_h + \vec{\Gamma}_p &= 0 . \end{aligned} \tag{1.13}$$

Based on Equations (1.4), (1.5), (1.12) and (1.13), a magnetic particle can either experience a translational motion due to $\vec{F}_m$, or perform a rotational motion due to $\vec{\Gamma}_m$. Besides the magnetic and hydrodynamic forces and torques, there are other interactions such as surface DLVO (Derjaguin-Landau-Verwey-Overbeek) force, Brownian motion, particle and fluid interactions, and inter-particle effects affecting the motion of the magnetic particles. Some will be considered under specific conditions in the following sections and some of them can be considered as a secondary effect and will be neglected [58].

MPs with certain special shapes can be driven by an alternating or rotational magnetic field. The force induced rotation or the torque is possible to induce translational motion when the magnetic part of a MP is designed or attached to a complex structure and subjected to

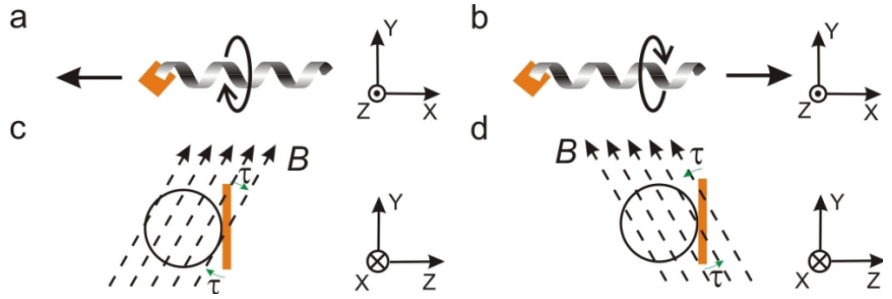

Figure 1.8: Schematic of an artificial magnetic swimmer with a magnetic head and a helical tail achieves (a) forward and (b) backward locomotion driven by a rotational magnetic field in the (c) clockwise and (d) counter-clockwise direction. Reprint from [59]

a viscous liquid as shown in **Figure 1.7(d)**. For example, **Figure 1.8** illustrates one typical design of a magnetic helical motor, consisting of a nonmagnetic helical tail and a soft magnetic head [59]. Under a rotational magnetic field, the magnetic head is driven to rotate in the y-z plane, and the helical tail follows. The thrust in the axial direction (x-axis) is mainly obtained from the hydrodynamic interaction between the helical tail and the carrier liquid. As a result, the helix moves forward along its axial direction. While experiencing an opposite magnetic torque, the helix is driven backward along the axis. In fact, the helical motor can only be driven by the magnetic torque and its locomotion can be precisely controlled by three orthogonal Helmholtz-coil pairs without any field gradient [60]. In addition, Choi *et al.* has shown that the magnetic helix can also be driven by three pairs of saddle coils, which give the same functions as the Helmholtz-coil pairs but with a smaller volume and less power consumption [61]. Gao, *et al.* fabricated a flexible Pt-Au-Ag_{flex}-Ni nanowire motor where the Ni section was connected to the end of a flexible Ag nanowire as shown in **Figure 1.9(a)** [62]. When a RMF was applied, the Ni section started to rotate, thus acting as a propeller to push the Ag nanowire forward. The moving direction could be adjusted by applying a constant magnetic field. Kim *et al.* fabricated a double-bead microswimmer that could be driven using a 100 Hz homogeneous RMF as shown in **Figure 1.9(b)** [53]. The double-bead microswimmer consisted of a 3 µm polystyrene (PS) microbead conjugated to a 150 nm MNP

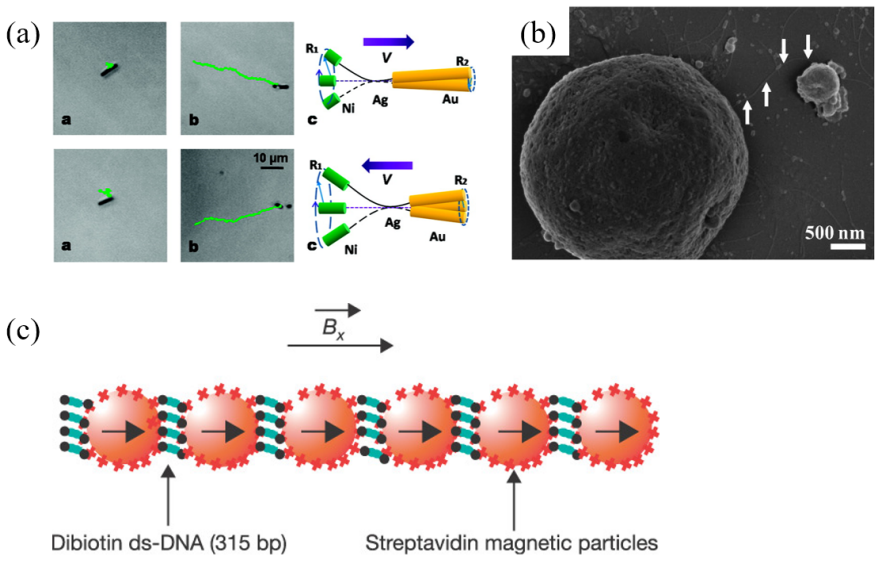

Figure 1.9: (a) The nanowire motor moving forward (top) and backward (bottom) under a RMF. Images marked with "a" are the optical images of the motor, "b" are the images after 15 sec and "c" are the schematic of the magnetic swimmer. Reprint from [62]. (b) 3 µm PS bead linked to a 150 nm MNP via a flagellar filament depicting dumbbell or double-bead microswimmers. The flagellar filament linking the two beads is indicated by the arrows. Reprint from [53]. (c) Schematic representation of a flexible magnetic filament. Reprint from [63].

via an avidin-biotin linker. It could rotate under a RMF and the small magnetic bead would act as a propeller similar to the nanowire motor. The reversible locomotion associated with an axial rotation is described by a mechanical principle that is known as "drag-based thrust" [64]. The physical origin of this kind of motion is the anisotropic hydrodynamic interaction between the solid body and the carrier liquid so that the net force of the hydrodynamic drag on the microswimmer acts as the propulsion force in the direction of the locomotion [59, 60, 62, 65]. Similar swimming motion can also be observed in nature, such as prokaryotic and eukaryotic microorganisms [64, 66, 67], persistently harvesting thrust energy from the surrounding fluids with the movement of its flagella or cilia. For such a complex-shaped particle, the translational velocity and rotational angular velocity $\vec{U}_p$ through the hydrodynamic interaction $\vec{F}_h$ and

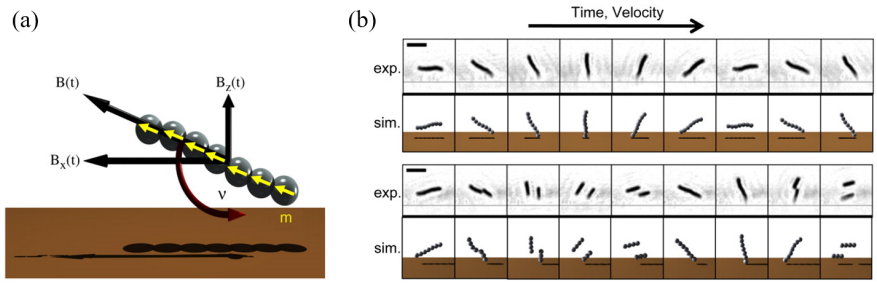

Figure 1.10: A experimental realization of "surface walkers". Reprint from [69]. (a) The geometry of "surface walkers". (b) The experimental and simulation results for a "surface walker" driven by a RMF of 5 Hz (top) and 7 Hz (bottom), notice the disassembly of the chain.

torque $\vec{\Gamma}_h$ can be related by a "resistance" matrix M_h [64],

$$\begin{bmatrix} \vec{F}_h \\ \vec{\Gamma}_h \end{bmatrix} = M_h \begin{bmatrix} \vec{U}_p \\ \vec{\Omega} \end{bmatrix}, M_h = \begin{bmatrix} e_1 & e_2 \\ e_2^T & e_3 \end{bmatrix}, \tag{1.14}$$

where e_1, e_2 and e_3 are the hydrodynamic elements of M_h. The resistant matrix M_h has to be symmetric according to the reciprocal theorem of Stokes flow [68].

Besides helix microswimmers, chain-like microswimmers made of linked magnetic beads using DNA could be driven to move by an alternating magnetic field as shown in **Figure 1.7(e)**. The chain swimmer was linked by DNAs (**Figure 1.9(c)**) and was first aligned horizontally by a 9 mT constant magnetic field and then a 14 mT sinusoidal magnetic field was applied in the vertical direction. The frequency of the sinusoidal magnetic field was in the range of 10 to 20 Hz. Under the combined fields, the magnetic bead chain would move like a flagella in the horizontal direction [63]. The last kind of DFM we will discuss in the section (**Figure 1.7(f)**) is the "surface walker". Sing, *et al.* reported a experimental realization of such manipulation method as shown in **Figure 1.10** [69]. The "surface walkers" is made of linked magnetic beads and is able to move translationally near a substrate surface under a RMF. Its moving speed v is related to the rotating frequency f, and the total length

of the chain,

$$v \sim faN\,, \tag{1.15}$$

where a is the radius of the beads and N is the total number of the beads. This equation is obtained by simply assume the chain is rotating on the surface with non-slip condition. An very interesting phenomena that the chain will break apart and moving individually can be observed when the rotating frequency f is high. The critical frequency f_c is given by,

$$f_c \sim \frac{B^2}{N^2\eta}\,, \tag{1.16}$$

where B is the magnetic field and η is the viscosity of the water.

1.2.3 Diffusion and reaction

As we have previously introduced, the magnetic manipulation of MNPs can provide the mechanisms to enhance drug's effectiveness. One of the mechanism is enhancing the diffusivity of the drug's molecules. Such an enhancement will result in a enhanced reaction rate thus improving the drug's efficiency. In this section, we will first discuss the diffusion phenomenon and the relationship between diffusion and reaction to understand the fundamental physics process of enhanced diffusion mechanism.

Diffusion is a mass transfer phenomenon that causes the distribution of a chemical species to become more uniform in space as time passes. In a microscopic point of view, the diffusion is caused by the random movement of media molecules pushing a particle to preform random-walk motion. To mathematically describe the random-walk motion, we can think there is a one-dimensional "walker" stay at position x and will move backward or forward one step with equal probability. The simplest random walk model treat the length of step as a constant Δx and it takes a constant Δt time to move. If we define the number of walkers

at position x_0 at time t_0 is $C(x_0, t_0)$, then we should have,

$$C(x_0, t_0 + \Delta t) = \frac{1}{2}C(x_0 - \Delta x, t_0) + \frac{1}{2}C(x_0 + \Delta x, t_0)\,. \tag{1.17}$$

This is because at $t = t_0 + \Delta t$, walkers located at x_0 are the walkers traveling from $x_0 - \Delta x$ and $x_0 + \Delta x$ at time t, with equal probability of 0.5. Now, if we take the Taylor expansion on the both side of Equation (1.17):

$$C(x_0, t_0 + \Delta t) = C(x_0, t_0) + \frac{\partial C(x_0, t_0)}{\partial t}\Delta t + \frac{1}{2}\frac{\partial^2 C(x_0, t_0)}{\partial t^2}(\Delta t)^2 + \cdots\,, \tag{1.18}$$

$$\frac{1}{2}C(x_0 - \Delta x, t_0) = \frac{1}{2}C(x_0, t_0) + \frac{1}{2}\frac{\partial C(x_0, t_0)}{\partial x}(-\Delta x) + \frac{1}{4}\frac{\partial^2 C(x_0, t_0)}{\partial x^2}(-\Delta x)^2 + \cdots\,, \tag{1.19}$$

$$\frac{1}{2}C(x_0 + \Delta x, t_0) = \frac{1}{2}C(x_0, t_0) + \frac{1}{2}\frac{\partial C(x_0, t_0)}{\partial x}\Delta x + \frac{1}{4}\frac{\partial^2 C(x_0, t_0)}{\partial x^2}(\Delta x)^2 + \cdots\,. \tag{1.20}$$

And substituting Equations (1.18) to (1.20) back into Equation (1.17), we have,

$$\frac{\partial C(x_0, t_0)}{\partial t}\Delta t + \cdots = \frac{1}{2}\frac{\partial^2 C(x_0, t_0)}{\partial x^2}(\Delta x)^2 + \cdots\,. \tag{1.21}$$

If $\Delta t \longrightarrow 0, \Delta x \longrightarrow 0$, and define $D \equiv \dfrac{(\Delta x)^2}{2\Delta t}$. Equation (1.21) reduces to,

$$\frac{\partial C(x_0, t_0)}{\partial t} = D\frac{\partial^2 C(x_0, t_0)}{\partial x^2}\,, \tag{1.22}$$

which is known as the one-dimensional diffusion equation. C is also known as the concentration of the chemical molecules, and D is the diffusivity. For a small particle with radius r in a low Reynolds number environment, its diffusivity can be estimated by the Stokes–Einstein equation:

$$D = \frac{k_B T}{6\pi\eta r}\,, \tag{1.23}$$

where k_B is the Boltzmann constant and T is the temperature. The diffusion can cause two

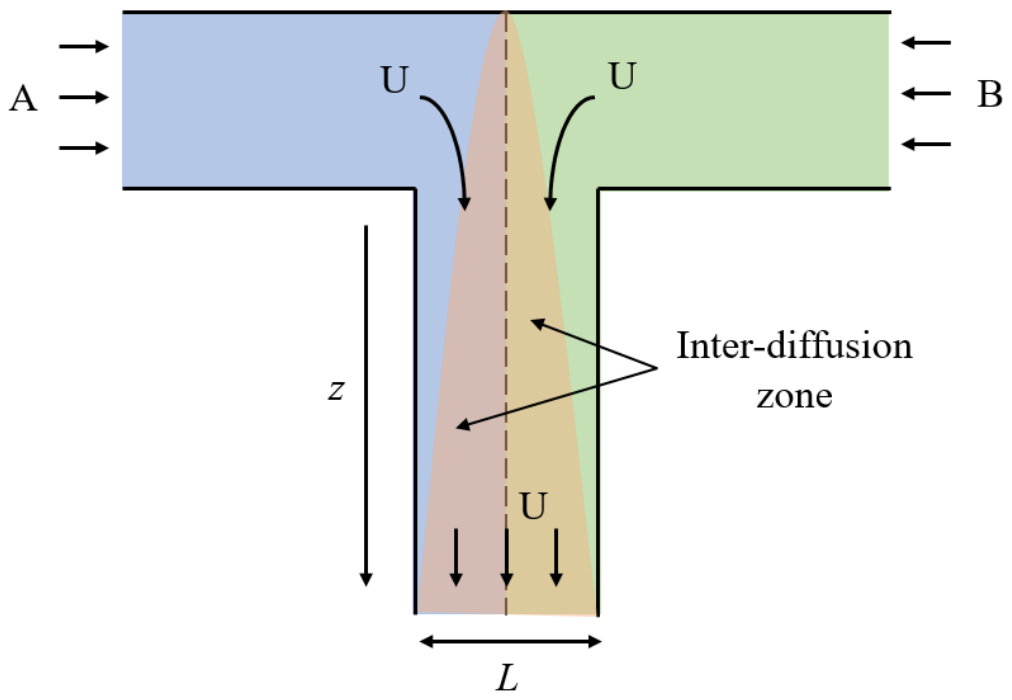

Figure 1.11: Different fluids A and B are mixed together at a T-junction to flow alongside each other down the channel. The width of the channel is L and the velocity of the flow is U.

chemical species mixed together. Pure diffusive mixing is usually very slow. In microfluidics, one common way to accelerate this process is using a T-junction to quickly mix chemical A and B as shown in **Figure 1.11**.

If the diffusivity of the particles or molecules is D. The time to complete mixing is equal to the time that particles/molecules require to diffuse across the entire channel, which can be written as $t_D \sim L^2/D$. During this time, the flow has move forward with a distance $z \sim Ut_D = UL^2/D$. The radio between z and L represents the relative importance of convection to diffusion and is known as the Péclet number Pe,

$$\frac{z}{L} \sim \frac{UL}{D} \equiv Pe\,, \tag{1.24}$$

where U and L are also known as the local flow velocity and the characteristic length, respectively.

It is well known that the actual mass transport of passive particles or molecules can be enhanced by convective flows. The enhanced diffusivity D^* is a function of the Péclet number. When Pe is small ($Pe < 3$), one can have [70],

$$D^* = D(1 + aPe^2)\,, \tag{1.25}$$

where a is a constant depending on the shape of the flow. When Pe is large, the analysis shows that enhanced diffusion varies as,

$$D^* = cD\sqrt{Pe}\,, \tag{1.26}$$

where c is a constant [70]. According to the collision theory, the rate of a chemical reaction is positively related to the collision frequency between two reactive molecules. So, for the reaction in a liquid environment, higher diffusivity will result in a higher mass transportation rate and also a higher chemical reaction rate. Chemical reactions follow this rule is called diffusion-limited reactions and according to the von Smoluchowski's equation, the reaction's kinetic rate k_D can be expressed as [71],

$$k_D = 4\pi(D_A + D_B)(R_A + R_B)\,, \tag{1.27}$$

where D_A and D_B are the diffusivity, R_A and R_B are the radius of the reactive molecules A and B, respectively.

Equation (1.27) gives us an idea that it is possible to accelerate the reaction rate of a diffusion-limited reaction by enhancing the reactant's diffusivity. This could be achieved by using active particles, such as rotating magnetic nanorods (MNRs), to enhance the mass transport of reactant as illustrated in **Figure 1.12**. Theoretical analysis indicated that the hydrodynamic enhanced diffusivity D can be expressed in the sum of two parts: $D = D^T + D^C$,

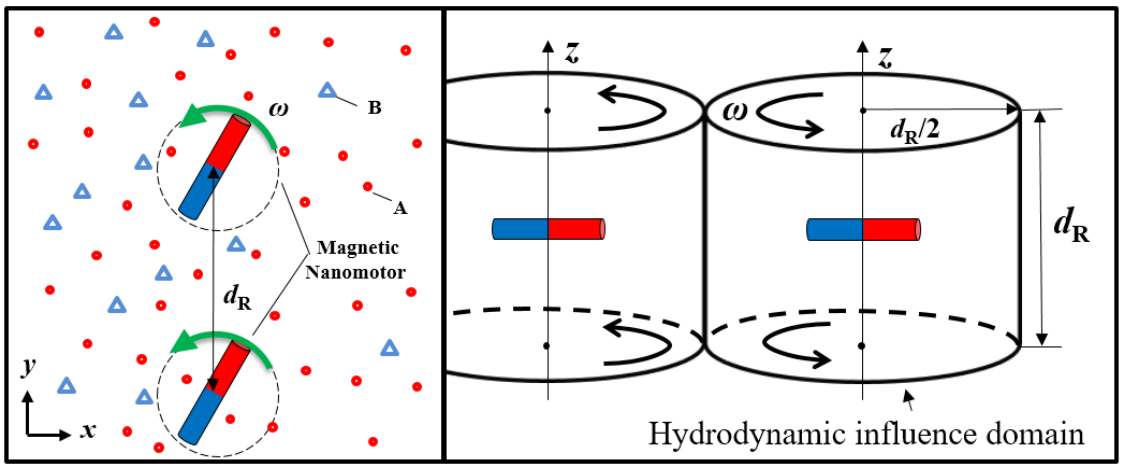

Figure 1.12: Schematic illustration of the hydrodynamic induced mobility by rotating MNRs. When a MNR in solution is driven by a rotational magnetic field, it will induce a creepy Stokes' flow that enhance the mobility of chemical A and B. The flow has a cylindrical hydrodynamic influence.

where D^T is the thermally induced diffusion coefficient given by the Einstein's equation (Equation (1.23)). D^C is convectional flow enhanced diffusion by rotating MNRs. The detailed expression for D^C is determined by Pe,

$$Pe = \frac{\overline{u} d_R}{D_T}, \tag{1.28}$$

where $d_R = C_{NR}^{-1/3}$ is the size of each cellular flow induced by a rotating MNR, C_{NR} is the number concentration of the rods, and $\overline{u}$ is the average velocity of the flow field induced by the MNRs as shown in **Figure 1.12**. Due to the low speed and small size, the rotating rods are modeled as concentrated torques inducing a Stokes' creeping flow at low Reynolds number. For a singular point torque $\vec{M}_t$ at the origin, the strength of rotlet $\vec{\gamma}$ in a closed control surface is [72],

$$\vec{\gamma} = \frac{\vec{M}_t}{8\pi\eta}, \tag{1.29}$$

while the velocity of a point on the surface positioning of vector $\vec{r}$ equals to,

$$\vec{u} = \frac{\vec{\gamma} \times \vec{r}}{|\vec{r}|^3} \,. \tag{1.30}$$

Thus, the velocity field $\vec{u}$ induced by a rotating MNR can be expressed as,

$$\vec{u} = \frac{\vec{M}_t \times \vec{r}}{8\pi\eta|\vec{r}|^3} \,. \tag{1.31}$$

Obviously, the hydrodynamic volume of a single rod is cylindrically symmetric with induced velocity decaying as r^2. If more than one rod are put in the liquid with a uniform distribution and an equal driven torque M_t is applied, the flow velocity $\overline{u}$ by multi-rotating rods can be averagely estimated as,

$$\overline{u} = \frac{\sum_{i=1}^{n} \int |\vec{u}| \, d\Omega}{V_L} = \frac{\left|\vec{M}_t\right| (\chi C_R)^{2/3}}{4\eta} \ln\left(1+\sqrt{2}\right) \,, \tag{1.32}$$

where $\Omega_i = \pi d_R^3/4$ is the hydrodynamic volume of a single rod, V_L is the total volume of the liquid, χ is a conversion factor that convert MNR mass concentration C_R to number concentration. At the low Reynolds number, the singular point torque $\left|\vec{M}_t\right|$ by a rotating MNR equals to the hydrodynamic drag torque on it,

$$\vec{M}_t = \int_0^{L/2} \left(\vec{D}_i \times \vec{l}\right) dl = \frac{-2\pi^2\eta\varepsilon L^3 f}{3} \,, \tag{1.33}$$

where $\vec{D}_i = 4\pi\varepsilon\eta U(l)$ is the Lamb drag per unit length of rod, and is proportional to the distribution of flow velocity along the rod $U(l) = 2\pi f l$, and the shape determined constant $\varepsilon = \left(\ln\left(\frac{L}{d}\right) - 0.66\right)^{-1}$. By combining Equations (1.28) to (1.33), one can estimate the constant Pe if detailed experiment conditions are known. Depending on the value of Pe,

using Equation (1.25) or Equation (1.26), the enhanced diffusion constant as well as the reaction rate can be calculated.

1.2.4 Theory of drug releasing

The controlled release of drug is crucial for drug delivery in medical applications. The general purpose of controlled release is to reduce the free diffusion of drug molecules through out the patient's body and maintain the drug concentration at a desired level locally as long as possible [73]. As we have discussed previously, the traditional tPA treatment can be greatly improved if tPA could be target delivered and then released locally with a controllable rate. Thus, it is very important to understand how the drug release rate is associated with experimental conditions. In this section, we will briefly introduce the theory of drug release from a spherical particle.

The drug molecules can be immobilized on a solid carrier's surface chemically (through covalent bond) or physically (through Coulomb force). Depending on the loading mechanism, the drug's releasing behavior will be different. For the chemically loaded drug, covalent bond will prevent the release of drug molecules unless the covalent bond is cleaved. In other words, the chemically loaded drug need a "trigger" to stimulate its release. This "trigger" could be a specific enzyme [74], light [75], pH value [76–78] or even temperature [79]. The detailed release behavior of chemically loaded drug is complicated and strongly dependent on the linking polymer and its cleavage mechanism [80]. Here, we will not discuss this type of release in detail.

The physically loaded drug usually can be released through a diffusion process. The fundamental principle for such releasing was first studied by Noyes and Whitney in 1897 [73]. The changes of drug concentration can be expressed as,

$$\frac{dC_t}{dt} = K_C(C_{sat} - C_t)\,, \tag{1.34}$$

where C_t is the concentration of drug at time t, K_C is a releasing constant, C_{sat} is the solubility (saturated concentration under the current condition) of the drug. For the drug that releases slowly and does not decompose, and when $C_{sat} \gg C_t$, Equation (1.34) is reduced to,

$$C_t = C_0 + K_0 t\,, \tag{1.35}$$

where C_0 is the initial consecration of drug, and K_0 is the releasing constant. The drug release process governed by Equation (1.35) is called the zeroth order release equation. It describes a system that the drug release rate is independent of its concentration [81–86]. However for some drugs, one has to consider the re-absorption of the drug molecules during their releasing process. The release of the drug is governed by the first order release equation. By solving Equation (1.34), we can have,

$$\ln C_t = \ln C_0 + K_1 t\,, \tag{1.36}$$

where K_1 is the first order release constant. Equation (1.36) can be used to describe the releasing of some water-soluble drugs from porous drug carriers [87–89].

Beside the zeroth and first order release models, another commonly seen release model is the Hixson-Crowell model which describes the drug release by dissolution, and with the changes of the carrier's surface area and diameter [90]. The mathematical equation is,

$$\sqrt[3]{W_0} - \sqrt[3]{W_t} = K_{HC} t\,, \tag{1.37}$$

where W_0 and W_t are the initial and the remaining amount of drug at time t, K_{HC} is the Hixson-Crowell constant. However, most drug release process is complicated and cannot be simply modeled using above three models. **Table 1.2** summarizes other mathematical models that are used to describe the drug release process under specific satiations.

Table 1.2: Mathematical models used to describe drug release process.

Model name	Mathematical equation*	Ref of example
Zero order	$Q_t = Q_0 + K_0 t$	[81]
First order	$\ln Q_t = \ln Q_0 + K_1 t$	[73]
Hixson-Crowell	$\sqrt[3]{W_0} - \sqrt[3]{W_t} = K_{HC} t$	[90]
Korsmeyer-Peppas	$\frac{Q_t}{Q_\infty} = K_{KP} t^n$	[91]
Weibull	$Q_t = Q_\infty \exp[1 - \exp[-\frac{(t-T)^b}{a}]]$	[92]
Higuchi	$Q_t = K_h \sqrt{t}$	[93]
Hopfenberg	$\frac{Q_t}{Q_\infty} = 1 - [1 - K_0 t / C_0 a_0]^n$	[94]
Baker–Lonsdale	$\frac{3}{2}[1 - (1 - \frac{Q_t}{Q_\infty})^{2/3}] - \frac{Q_t}{Q_\infty} = K_{BL} t$	[95]

* Q stands for the amount of drug released at certain time t indicated by the subscript. K is the kinetic rate of the model. Other symbols are experimental determined constants.

1.3 Fabrication and synthesis of MNRs

One of the major challenges in using MNRs to improve stroke treatment is the fabrication of small MNRs with the ability to control their sizes and magnetic properties. Two major methods will be used in this dissertation: the glancing angle deposition (GLAD) method and the hydrothermal based chemical synthesis process.

1.3.1 Glancing angle deposition

GLAD is a physical vapor deposition based technique in which the substrate is rotated in the polar and azimuthal directions by two stepper motors programmed by a computer. The GLAD method can effectively fabricate nanostructures with different shapes and a simple schematic illustration of GLAD technique is shown in **Figure 1.13(a)**. By tilting the

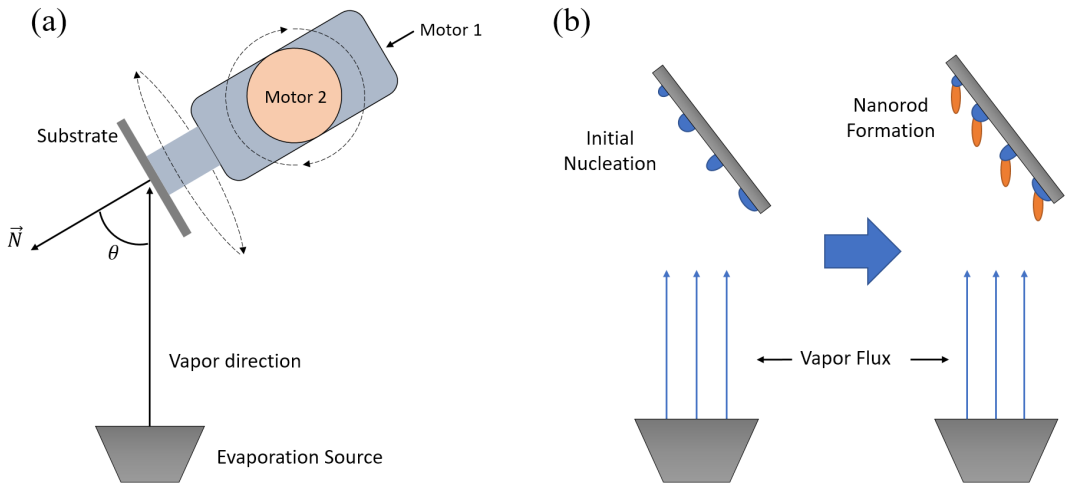

Figure 1.13: GLAD method illustration and its mechanism. (a) Schematic of OAD/GLAD: θ the angle between the substrate surface normal $\vec{N}$ and the vapor direction. The surface rotating is controlled by Motor 1 and θ is controlled by Motor 2. (b) Illustration of shadowing growth. Left: vapor begins to deposit on a flat substrate to form nucleation points. Right: as more accumulation occurs, it is restricted to the points of nucleation due to the shadowing effect, and an array of NRs forms.

substrate to a large angle with respect to surface normal ($\theta > 70^\circ$) during vapor deposition, an array of nanostructures grows on the surface of the substrate. If Motor 1 is not rotating, and because of the large vapor incident angle, this configuration is known as the oblique angle deposition (OAD). If Motor 1 is on and the substrate is rotating, further control over nanostructure geometry is possible which is a process known as the GLAD.

The mechanism of GLAD is mainly determined by the shadowing growth. Specifically, when the vapor flux approaches the substrate at a large angle, randomly nucleated islands will be formed on the surface initially and serve as seeds for later growth. Further accumulation of the vapor on the surface after the formation of the islands is restricted to these sites, leading to the formation of an array of NRs. This phenomenon is called the shadowing effect, and the process is shown in **Figure 1.13(b)**. The GLAD method has several advantages compared to other nanofabrication techniques [98]. First, the length, separation, and density of the NRs can be easily controlled by the vapor incident angle θ and the deposition duration.

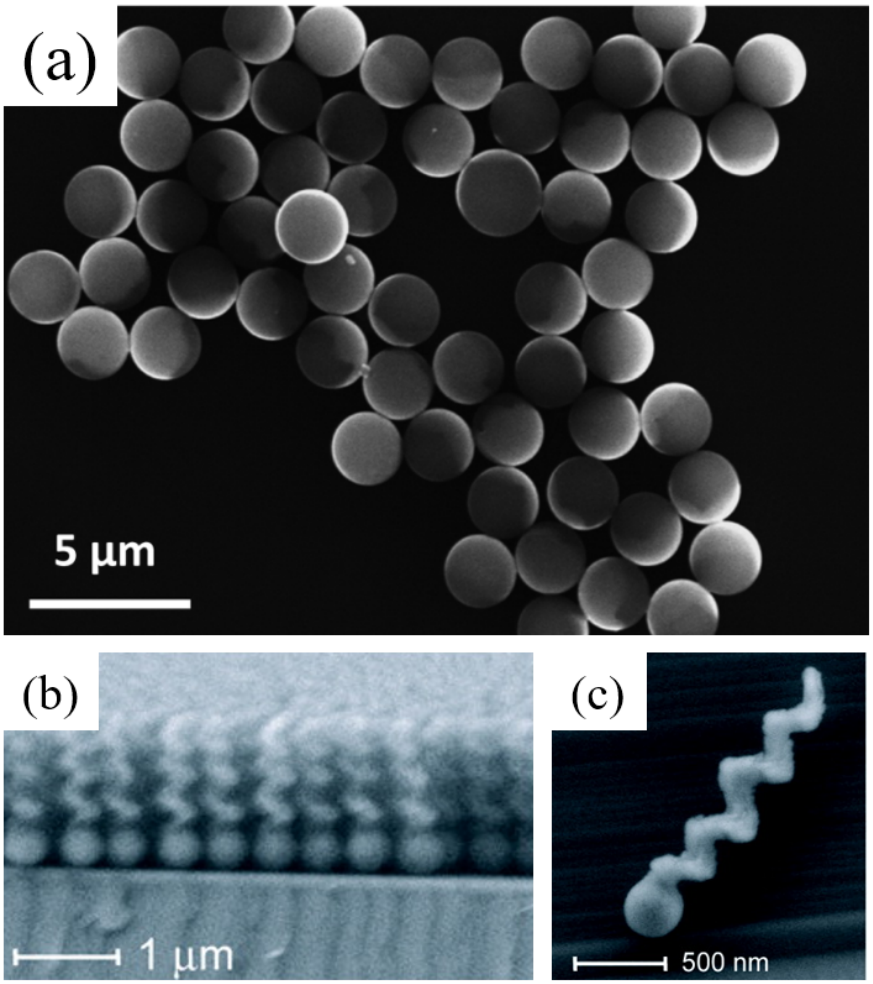

Figure 1.14: Nanostructures fabricated by GLAD method. (a) SEM image of Iron Oxide-Capped Janus magnetic particles. Reprint from [96]. (b) A cross-section view of the fabricated SiO_2 screw structures. Reprint from [97]. (c) SEM image of a individual SiO_2 screw. Reprint from [97].

For example, three-dimensional NR structures can also be sculptured by programming the rotation of the two motors. As shown in **Figure 1.14(a)**, if $\theta = 0^\circ$ and Motor 2 is off. Janus particles are fabricated [96]. When $\theta = 87^\circ$ and the substrate is rotated by a speed of $\sim 0.07\,\text{rpm}$, screw-like structures can be fabricated [97] as shown in **Figure 1.14(b)**. Second, by using a two-sources GLAD method, the fabricated MNRs' magnetic prosperities such as the magnetization and the coercivity can be systematically controlled by adjusting the relative rates of the two sources [99]. Finally, the GLAD method is capable for large

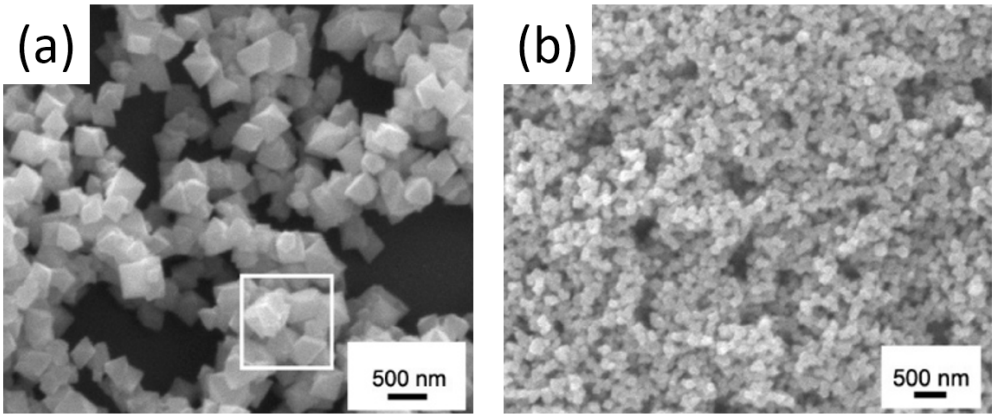

Figure 1.15: Fe_3O_4 NPs synthesized using hydrothermal method. Reprint from [102]. (a) With PEG in reaction. (b) Without PEG in reaction.

quantity production because physical vapor deposition is a very popular technique for thin film coating.

1.3.2 Hydrothermal synthesis

The hydrothermal synthesis method is one of the most popular wet chemical approaches for the synthesis of inorganic nanocrystals, especially for metals and metal oxides [100]. Iron oxide NPs, for both Fe_2O_3 [101] and Fe_3O_4 [102] can be synthesized using this method. The detailed experiment conditions such as temperature and iron salt may varies and different product will be obtained. For example, Qin, *et al.* synthesized α-Fe_2O_3 nanocubes using iron (III) nitrate ($Fe(NO_3)_3 \cdot 9\,H_2O$) and triethylamine at 160 °C for 24 hours in a teflon-lined autoclave [101]. The nanocubes were 100 to 200 nm in width. Generally, α-Fe_2O_3 is not magnetic. But by annealing Fe_2O_3 in a N_2 and ethanol environment at 350 °C, Fe_2O_3 can be reduced to Fe_3O_4 with about 1 hour. Zhang, *et al.* has reported a method that using $FeSO_4 \cdot 7\,H_2O$, NaOH, and KNO_3 to directly synthesize Fe_3O_4 NPs at 90 °C [102]. The

formation process of Fe_3O_4 nuclei contains three steps:

$$Fe_2^+ + OH^- \longrightarrow Fe(OH)_2$$

$$Fe(OH)_2 + H_2O + NO_3^- \longrightarrow Fe(OH)_3 + NO_2^-$$

$$Fe(OH)_2 + Fe(OH)_3 \longrightarrow Fe_3O_4\downarrow + H_2O$$

It is discovered that adding polyethylene glycol-6000 (PEG-6000) can increase the size of Fe_3O_4 NPs. SEM observation shows that octahedral crystals with sizes ranging from 200 to 300 nm dominate the sample prepared with PEG (**Figure 1.15(a)**), while quasi-spherical crystals in the size range of 100 to 150 nm overwhelm the sample prepared without PEG (**Figure 1.15(b)**).

1.4 Contents of dissertation

This dissertation consists of five chapters. Chapter 1 gives the general information about stroke and an updated review of recent developments of using nanotechnology to improve stroke treatment and the motivation of this dissertation. Then the properties of magnetic NPs and their medical applications are discussed, and the fabrication of both Ni and Fe_3O_4 MNRs using OAD or hydrothermal method is also elaborated. Chapter 2 focus on the manipulation of MNR clusters using a non-uniform alternating magnetic field. This manipulation method doesn't require complex and expensive instruments while can achieve micrometer scale precision. Chapter 3 describes how to use rotating MNRs to directly enhanced the diffusion of tPA molecules which can improve the effectiveness of tPA. A theoretical enhance diffusion model is also introduced. In Chapter 4, we manage to immobilize tPA onto Fe_3O_4 NRs and study how tPA release from these NRs. A tPA release model is given in this chapter. At last, Chapter 5 gives the conclusion of the work done in this dissertation, and possible future experiments and applications.

Chapter 2

Manipulation of Magnetic Nanorod with a Nonuniform Alternating Magnetic Field

2.1 Introduction

Understand and explore high-precision manipulation of MNRs in liquid environments could help us to develop new methods to improve stroke treatment. For example, in biomedical applications, NPs usually act as carriers to load drugs [103] or other cargo [104] and are specifically delivered to target locations. In addition, MNRs driven by a RMF can induce active flow to enhance thrombolysis efficiency [105, 106]. There are many different ways to use EMF to manipulate MNPs or MNRs as summarized in **Figure 1.7**, with pros and cons. In this chapter, we discover a different and very simple method for manipulating MNR clusters using a non-uniform alternating magnetic field (nuAMF) as shown in **Figure 2.1**. Under the

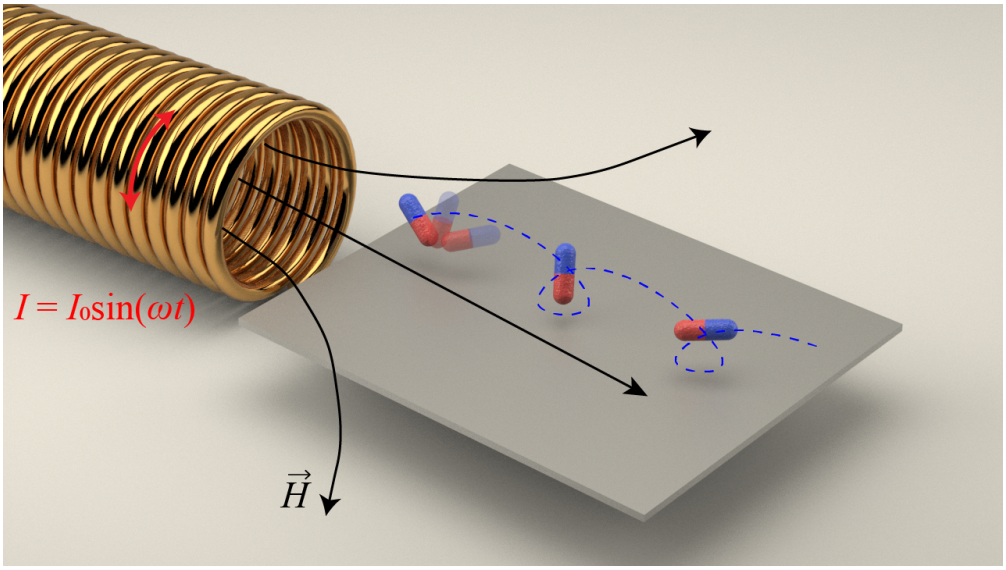

Figure 2.1: The manipulation of a MNR using a non-uniform alternating magnetic field near a substrate surface.

nuAMF generated by a single solenoid driven by an alternating current, we have achieved precise actuation of a single MNR and an arbitrary anisotropic shaped magnetic clusters (MCs) that are spontaneously formed by the aggregation of ferromagnetic Fe_3O_4 NRs near solid substrates. Importantly, facile actuation has been realized using magnetic fields that are orders of magnitude weaker than those used in typical magnetic manipulation methods. Through synergistic integration of systematic experiments and simulations, we show that the actuation originates from the subtle interactions between classical magnetophoresis and the surface walker mechanism, and develop design rules for such actuations.

2.2 Experiment methods

We used three kinds of MNPs in the experiments: Fe_3O_4 NRs, Ni NRs, and Ni Janus microspheres. The hydrothermal method introduced in **Section 1.3.2** was used to synthesize the Fe_3O_4 NRs [107]. Briefly, a mixture of 75 ml, 0.02 M $FeCl_3 \cdot 6\,H_2O$ and 0.45 mM NaH_2PO_4 aqueous solution was transferred into a 100 ml autoclave and heated at 160 °C in an oven for 12 hours. When the autoclave was cooled down to room temperature, the resulting Fe_2O_3 NRs were collected by centrifugation at a speed of 12000 rpm and washed twice with deionized (DI) water. After drying in an oven at 80 °C overnight, the Fe_2O_3 NRs were then annealed in N_2 carried ethanol flow with a flow rate of 50 sccm at 350 °C for 1 hour to obtain the Fe_3O_4 NRs. **Figure 2.2(a)** shows a representative SEM image of the Fe_3O_4 NRs used in our experiments. These are uniform ellipsoid rods with an average length of 300±40 nm and an average diameter of 51 ± 7 nm. The magnetic hysteresis loop of these NRs were characterized by a vibrating sample magnetometer (VSM, MicroSence EZ7) and is shown in **Figure 2.2(b)** indicating that the Fe_3O_4 NRs are ferromagnetic with a residual magnetization $m_r \approx 25\,\mathrm{emu\,g^{-1}}$ and a coercivity $H_c \approx 300$ Oe. The saturated magnetization $m_s \approx 80\,\mathrm{emu\,g^{-1}}$.

Both the Ni NRs/Janus particles were fabricated by the OAD method [108]. A monolayer of 2 µm diameter PS bead was first prepared on Si substrates using an air-liquid interface method [109]. To fabricate uniform Ni NRs, the bead-coated Si substrates were loaded into a

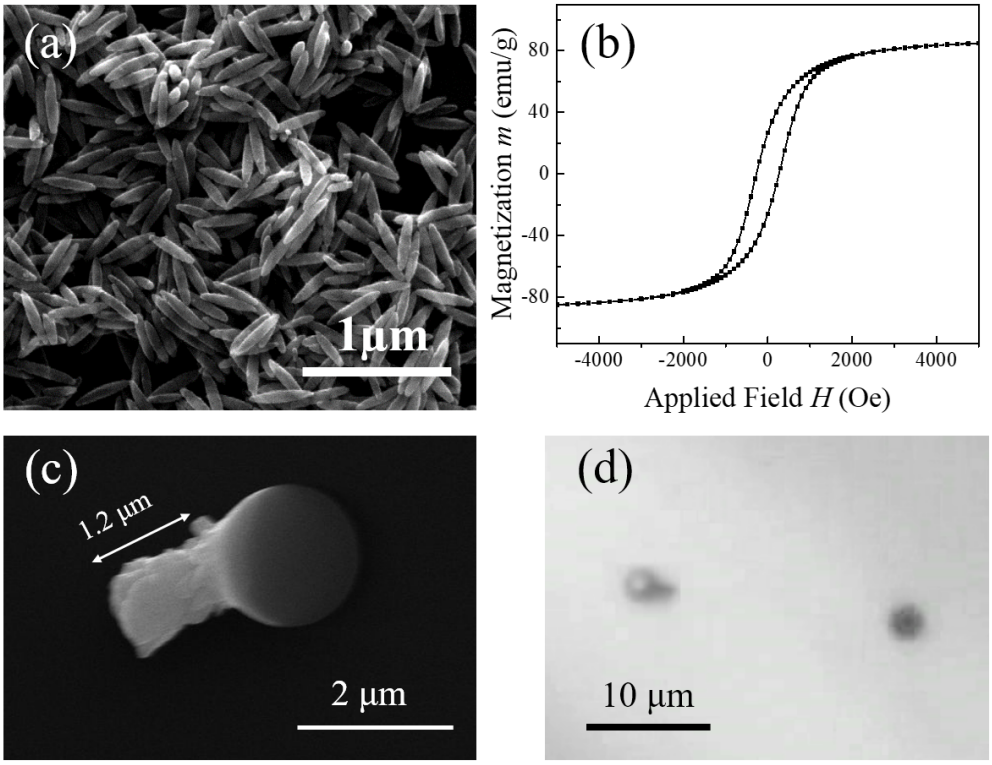

Figure 2.2: (a) The representative SEM image of Fe_3O_4 NRs. (b) The magnetic hysteresis loop of the Fe_3O_4 NRs. (c) The SEM image of a single Ni NR. (d) An optical microscope image of a single dispersed Ni NR and a Ni Janus NP in water.

custom-built electron beam evaporation chamber. Nickel (Ni, 99.95%, Alfa Aesar, Ward Hill, MA) was deposited at a vapor incident angle of 86° and at a rate of $\sim 0.5\,\mathrm{nm\,s^{-1}}$, monitored by a quartz crystal microbalance (QCM) facing directly toward the incident vapor. Ni NRs of length $\sim 1\,\mu\mathrm{m}$ were obtained when the QCM reading reached $2\,\mu\mathrm{m}$. A representative SEM image of a fabricated Ni NR is shown in **Figure 2.2(c)**. To fabricate the Janus particles, the same strategy was used except the vapor incident angle was set to be 0° and the deposition was stopped when the QCM reading reached 200 nm [110]. The Fe_3O_4 NRs and Ni NRs/Janus particles were dispersed in DI water with the help of sonication. The Fe_3O_4 NR suspension was diluted to a mass concentration of $0.1\,\mathrm{mg\,ml^{-1}}$ and Ni NR/Janus particle suspension was diluted to a mass concentration of $0.01\,\mathrm{mg\,ml^{-1}}$. During the dispersion, due to the relatively high concentration and ferromagnetic property of Fe_3O_4 NRs, they naturally form small

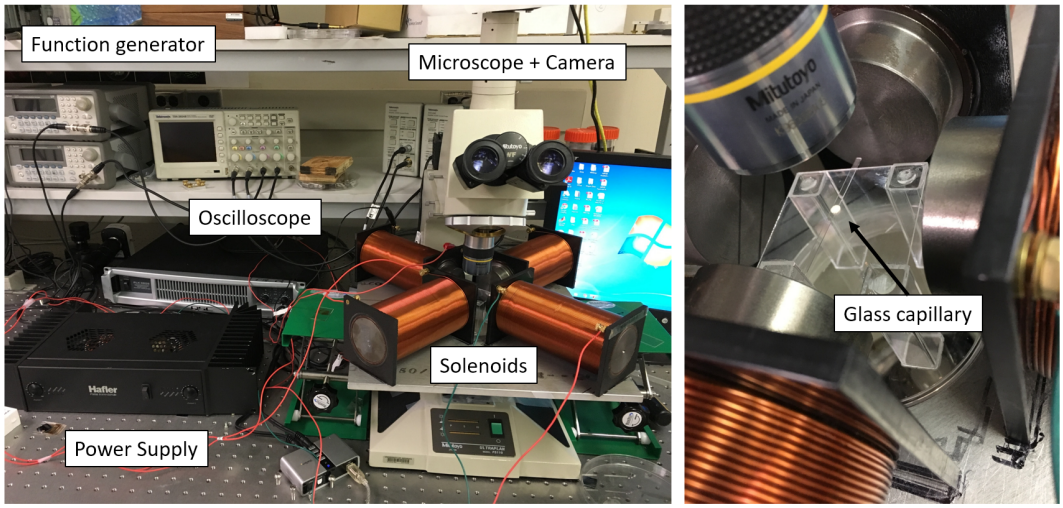

Figure 2.3: The experiment setup of non-uniform alternating field experiment.

MCs as shown in **Figure 2.5(a)**. Under our current experiment conditions, the width of most of these Fe_3O_4 MCs range from 10 µm to 20 µm . All of the MCs are stable enough to maintain their shapes during experiments unless a collision happens. For the suspension of Ni NRs/Janus particles, they were single dispersed because of the much lower mass concentration as shown in **Figure 2.2(d)**. The suspension was carefully transported into a rectangular glass capillary tube (height: 100 µm and width: 2 mm).

The tube was placed in the center of four identical solenoids under a large-working distance optical microscope (Mitituya FS110) as shown in **Figure 2.3**. The solenoids were driven by two dual channel power supplies that were modulated by two function generators (Agilent 33220A) to generate a nuAMF of a specific frequency f_H from 5 to 160 Hz. The magnetic field was a function of distance L from the solenoid's front surface and was measured for different input currents as shown in **Figure 2.4**.

The sample was placed at $\sim L = 4.5$ cm away from the front face of the solenoid and, according to the calibration curve, the maxima magnetic field generated at $I_0 = 2$ A was 4.2 mT and the field gradient was $\sim 0.13\,\mathrm{mT\,mm^{-1}}$ measured by Gauss meter (Model 5080, F. W. BELL). The movies of the MCs were obtained by a fast CCD camera (Phantom

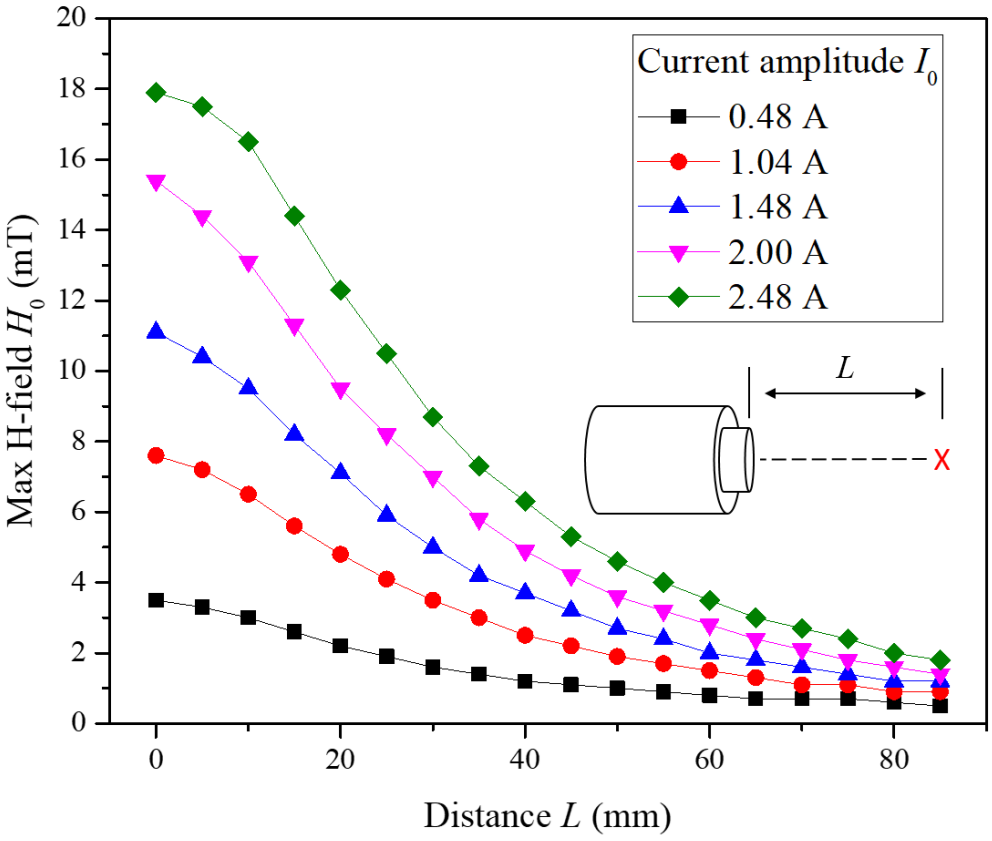

Figure 2.4: Magnetic field calibration curve for a solenoid with a $f_H = 10\,\text{Hz}$ AC.

v9.1) through the microscope with a 10X or 50X objective lens. During the experiments, the camera recording speed was set to be at least 10 times the frequency f_H. Then the movies were analyzed using an in-house cluster tracking Matlab program. The program could track the trajectory of clusters with an area larger than $40\,\mu\text{m}^2$ and record the cluster's center coordinates (x, y), width W (the length of cluster projected in x-direction) and height (the length of cluster projected in y-direction) of the cluster for each movie frame (See **Appendix A** for details).

2.3 Translational motion under nuAMF

As an example, **Figure 2.5(a)** shows several representative movie frames of a MC in water under a nuAMF generated by an alternating current (AC) with a frequency $f_H = 10\,\text{Hz}$ and a current amplitude $I_0 = 2\,\text{A}$. **Figure 2.5(b)** is the corresponding SEM image of the

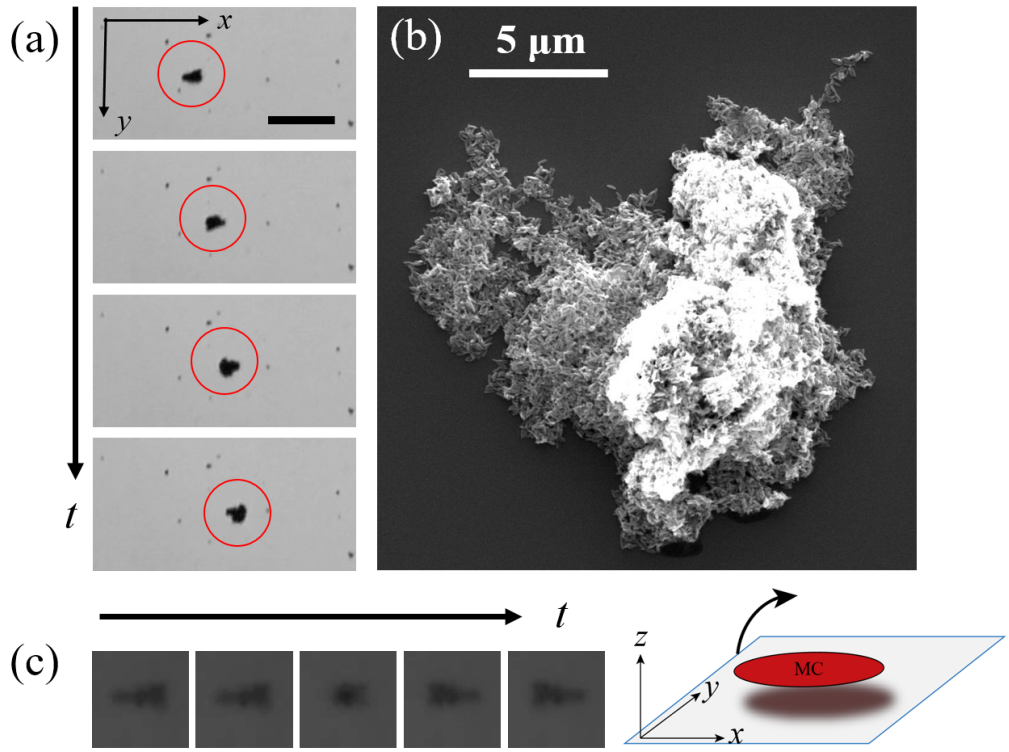

Figure 2.5: The movie frames to show the motion of MCs when a solenoid is placed at the left-hand side. (a) The movie of MCs rotating and moving. The targeted MC is marked with a red circle. The time interval between adjacent frames is 0.2 s and the scale bar indicates 50 µm. (b) The corresponding SEM image of the targeted MC in (a). (c) The zoomed-in out-of-plane rotation of a MC during one period. The size of the images in (c) is 17 µm × 17 µm, and the frame interval is 0.02 s. The cartoon illustrates the out-of-plane rotation of a MC.

indicated MC. The projected area of the MC is $A \approx 160\,\mu m^2$ and the MC consists of thousands of NRs. During this experiment, the solenoid was placed at the left-hand side. The time interval Δt between adjacent images in **Figure 2.5(a)** is 0.2 sec. One can observe that when the nuAMF is applied, the MC starts to flip in and out of the x-y plane while performing a translational motion toward the right side. The induced translational motion is mostly along the x-direction with a large x-component speed $v_x = 77\,\mu m\,s^{-1}$ and a small y-component speed $v_y = 8.8\,\mu m\,s^{-1}$. Images of a MC flipping in and out of the x-y plane under a $f_H = 5\,Hz$ magnetic field are shown in **Figure 2.5(c)** with a frame interval $\Delta t = 0.02\,s$. Most MCs observed perform a translation motion with out-of-plane rotations while a few

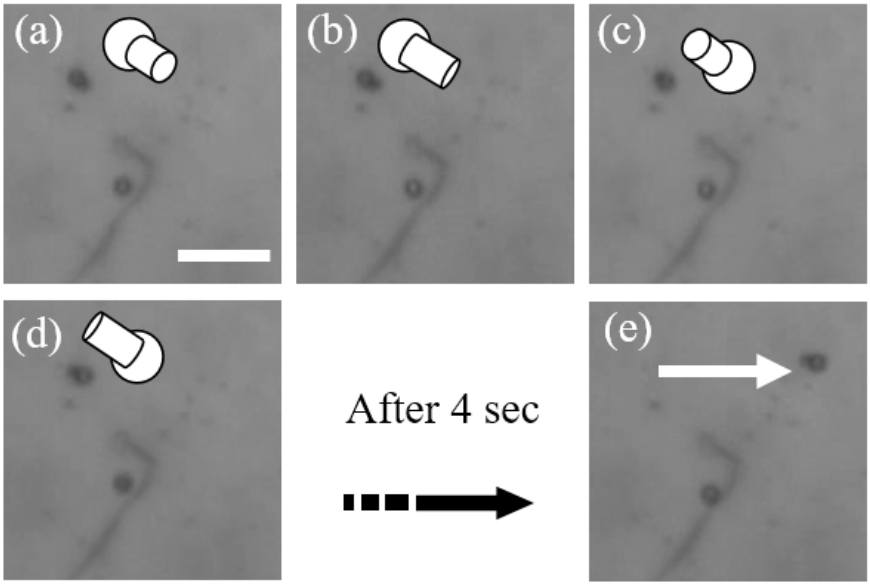

Figure 2.6: Movie chips that showing a single Ni MNR perform translation motion with out-of-plane rotations in a $f_H = 10\,\text{Hz}$ nuAMF. (a) to (d) The movie chips of the rotation of a Ni MNR and a half Ni coated Janus bead in one period (0.1 sec). The rod is preforming out-of-plane rotating and moving towards right hand side. While the Janus bead is rotating and moving in random direction due to Brownian motion. (e) Shows the movie chip after 4 sec. An arrow is drawn to indicate the moving direction of the rod. With in 4 sec, the rod has moved about 18 µm to the right hand side while the Janus bead almost stays at same place. The scale bar: 10 µm.

carry out in-plane oscillation, which means the long axes of MCs is moving back and forth periodically in the x-y plane. We have performed the same experiments using individual Ni NRs instead of Fe_3O_4 MCs, and similar behaviors have been observed, *i.e.*, even for a single Ni NR, when it is driven by a nuAMF, it also rotates out-of-plane and moves translationally as shown in **Figure 2.6**. However, since the Brownian motion would play a more important role for small Ni NRs, we will focus on MCs in this paper. Unlike a permanent magnet pulling a magnetic object, the MCs move away from the solenoid, and the speed of the translation motion is closely related to the size of the MC. More detailed experimental data show that the shape of the MC, as well as the magnetic field properties such as its frequency f_H, strength $|\vec{H}|$, and gradient $\nabla|\vec{H}|$, also affect the behavior of the translational motion. The detailed relationships are summarized below.

The necessary conditions for the translational motion. The rotation of MCs cannot always induce translational motions. Our experimental results indicate that there are three necessary conditions for the translational motion to occur: (a) The MCs must locate near a substrate surface. Otherwise, the MCs will be attracted by the EMF moving slowly towards the solenoid. (b) The magnetic field must be alternating and strong enough to induce a rotation; (c) The magnetic field must be non-uniform. In addition, the translational motion of a MC is stronger if it has a more anisotropic shape as **Figure 2.6** showing the difference between a MNR and a magnetic Janus particle under a 20 Hz nuAMF. A constant and strong enough magnetic field will pull the MCs towards the solenoid, which is opposite to the phenomena we observed. Also, the field strength $|\vec{H}|$ must exceed a critical value for the MCs to rotate. For the experiments we performed, when the field frequency $f_H = 10\,\mathrm{Hz}$, we found that the minimum amplitude of current I_0 needed to move the MCs was about 0.5 A. A detailed relationship between the motion of MCs and I_0 will be discussed later. The second condition, the need of non-uniform magnetic field, is validated by experiments with three field configurations as shown in **Figure 2.7**.

First, a pair of solenoids were used to produce a uniform alternating magnetic field as shown in **Figure 2.7(a)**. The currents passing through the two solenoids had the same amplitude $I_0 = 2\,\mathrm{A}$, and they were in-phase. According to our measurements and the calculation of the solenoid's magnetic field shown in **Figure 2.4**, the center between the two solenoids has no field gradient. The trajectories of MCs are plotted in **Figure 2.7(a)**. Most MCs perform random motion, but a few MCs move towards one solenoid. However, when the left solenoid was removed, all of the MCs started to move away from the right solenoid as shown by the trajectories in **Figure 2.7(b)**. According to our measurement, there is a field gradient of $-0.26\,\mathrm{mT\,mm^{-1}}$ in this case. Numerical calculation also verified this fact. In addition, if the left solenoid was placed back, but an out-of-phase current was applied as shown in **Figure 2.7(c)**, all MCs moved toward the upper left corner. This is possibility because the

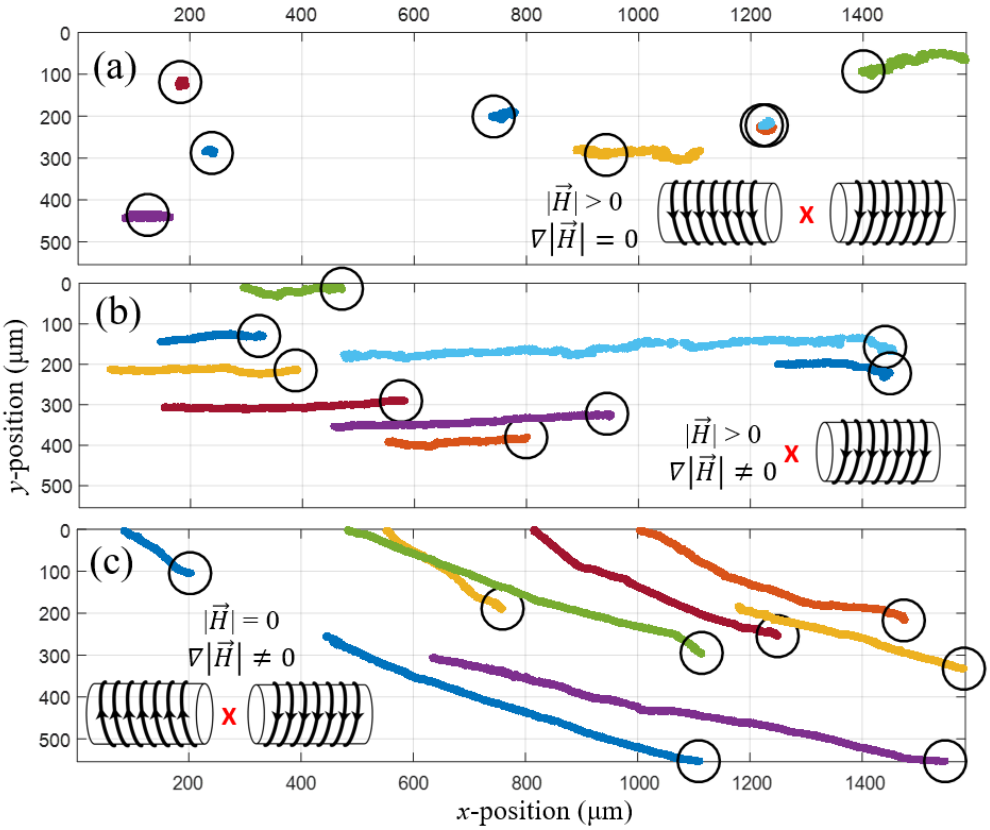

Figure 2.7: Trajectories of the MCs at three different field configurations: (a) a uniform alternating magnetic field; (b) a nuAMF generated by a single solenoid; and (c) a nuAMF produced by two solenoids.

sample might not be exactly placed at the center of solenoids. The shape of the MCs also plays an important role in the observed phenomena. For all the MCs spontaneously formed in the suspension, they have irregular shape, thus most of them can be driven by the nuAMF to move. We also tested the behavior of magnetic Janus particles. After being dispersed in water, under the same field conditions as those MCs in **Figure 2.7(b)**, we observed that the Ni rods rotated and moved translationally while the spherical Janus particles mainly performed random walk. Therefore, we conclude that a more anisotropic shape of the MCs helps enhance their translational motion under a nuAMF.

Double frequency effect. In order to understand the detailed motion behavior of MCs under a nuAMF, we have performed systematic analysis on the motion trajectories of

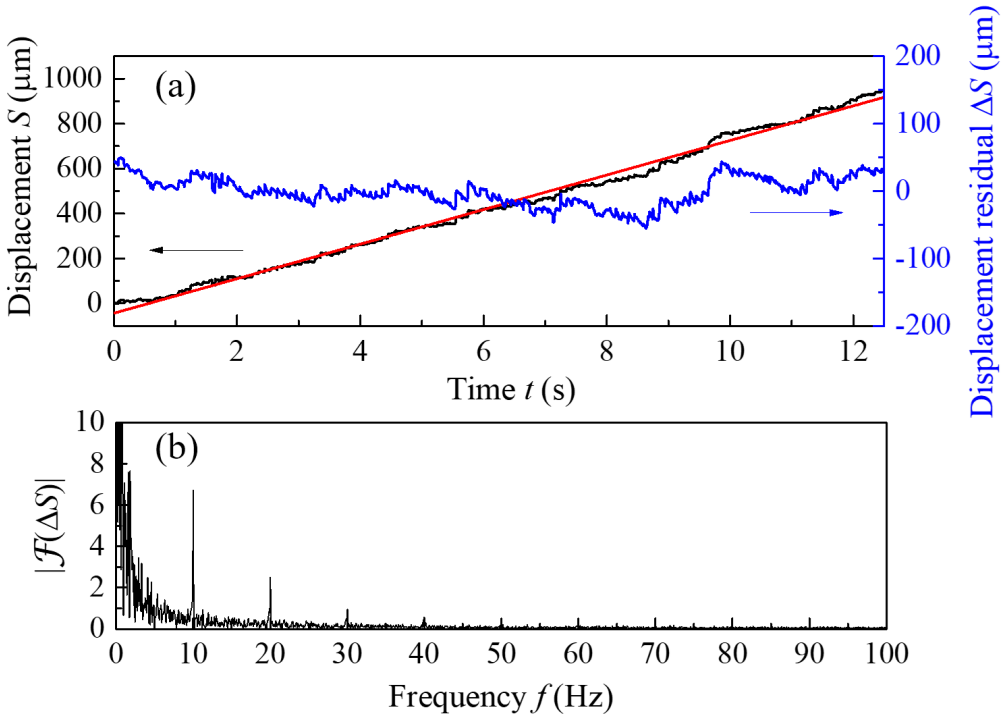

Figure 2.8: The detailed analysis of the trajectory of a single MC at $f_H = 5\,\text{Hz}$ and $I_0 = 2\,\text{A}$. (a) The plots of displacement $S(t)$ and the residual $\Delta S(t)$. The straight line is a linear fit. (b) The FFT of $\Delta S(t)$. The strongest peak is at $f = 5\,\text{Hz} = 2f_H$.

selected MCs. All of the results indicate that at low field frequency, the movement of the MCs exhibits periodic behavior, and the period is closely related to f_H. **Figure 2.8(a)** shows a representative displacement curve $S(t)$ of a MC driven by a $f_H = 5\,\text{Hz}$ magnetic field. $S(t)$ increases almost linearly with respect to t but also with notable fluctuations. By fitting the data with a linear relationship $S(t) = v_t + S_0$, we observe that the MC was moving at a speed $v = 76.9 \pm 0.1\,\mu\text{m}\,\text{s}^{-1}$ and $S_0 = 43.6 \pm 0.8\,\mu\text{m}$. The residual $S(t) = S(t) - v_t - S_0$ represents the position fluctuation of the cluster and is plotted in **Figure 2.8(a)**. A close inspection of $\Delta S(t)$ indicates that it has a periodic behavior. To better understand this behavior, a fast Fourier transform (FFT) was used to analyze S(t), and the FFT amplitude (denoted as $|\mathcal{F}|$) is plotted as a function of frequency f in **Figure 2.8(b)**. A very interesting phenomenon is observed; at $f = 2nf_H$, where n is a positive integer, such as f =10 Hz, 20 Hz and 30 Hz ..., *etc.*, sharp spectral peaks appear, indicating that the fluctuation in the MC's motion is

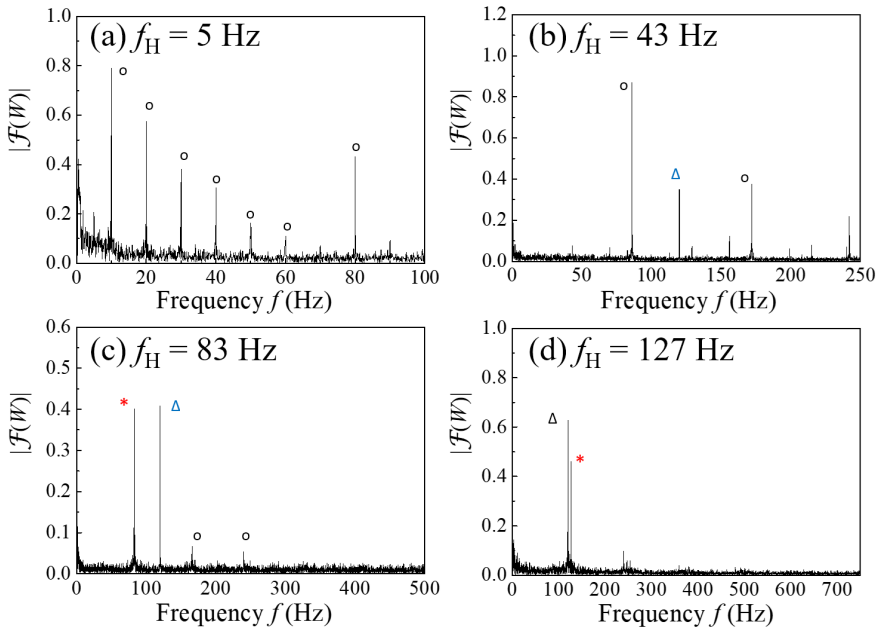

Figure 2.9: The FFT of the width W of a moving MC for fH = (a) 5 Hz, (b) 43 Hz, (c) 83 Hz, and (d) 127 Hz. Here $I_0 = 2$ A. The frequency peaks are indicated by different symbols: O: $2nf_H$, Δ: 120 Hz, *: f_H

related to the harmonics of the applied magnetic field. In particularly, at $f = 2f_H = 10$ Hz, the spectral peak is the highest and sharpest, indicating that the MC's motion has a strong $2f_H$ component. The FFT analysis of other MCs at this frequency also confirmed that the nuAMF-induced motion exhibits a fluctuation with a major frequency twice that of the field frequency f_H. Such a displacement is consistent with the MC's width fluctuation due to the out-of-plane rotation. For this reason, the MC's width shares exactly the same behavior with the $S(t)$.

However, as the f_H increases, the FFT spectral peaks of the fluctuation start to change slightly: a sharp peak at the base frequency $f = f_H$ appears in addition to its higher order harmonics. **Figure 2.9** shows the FFT spectrum of the width W of the MCs from four independent experiments. Most of the applied frequencies f_H are chosen to be prime numbers to avoid any interference from the line frequency. When $f_H < 60$ Hz, the strongest FFT peak is located at $f = 2f_H$. However, when $f_H > 60$ Hz, the position of the strongest FFT peak

shifts from $2f_H$ to f_H. In the FFT spectrum of the $f_H = 43\,\text{Hz}$, $83\,\text{Hz}$ and $127\,\text{Hz}$ cases, a peak at $f = 120\,\text{Hz}$ is shown and this may due to the contamination from the illumination light.

The effect of the driving current I_0, field frequency f_H, and cluster size A. Since the magnetic field generated by one solenoid is a function of the distance L and the driving current I_0 as shown in **Figure 2.4**, it is not easy to keep either $|\vec{H}|$ or $|\nabla\vec{H}|$ fixed while changing the other. Instead, we performed a systematic experiment with different I_0 for a fixed $f_H = 10\,\text{Hz}$ at the same location to investigate how MCs move under different field conditions. Four different MCs with projected areas A =$30\,\mu\text{m}^2$, $36\,\mu\text{m}^2$, $140\,\mu\text{m}^2$ and $160\,\mu\text{m}^2$, were chosen to be tracked and analyzed. The resulting translational speed v *vs.* I_0 is plotted in **Figure 2.10(a)**.

When I_0 is low ($I_0 < 0.5\,\text{A}$), the MCs would not move but only vibrate. As I_0 increases, all MCs start to move and the moving speed v increases monotonically with I_0. When I_0 reaches a relatively large value, v approaches a constant. When the cluster's projected area A is larger, the saturation speed v is greater. In the FFT analysis, we show that the motion of the MCs is closely related to the out-of-plane rotation and the applied field frequency f_H plays a decisive role. Such a rotation must be induced by the interaction of $\vec{H}$ and the MC via the magnetic torque $\mu_0\vec{H} \times \vec{M}$. Clearly such a torque will be balanced by an induced hydrodynamic torque to keep a constant rotational frequency. Note that increasing $|\vec{H}|$ would not change the rotational frequency of the MC. Rather in our experiment, since the change of I_0 simultaneously increases $|\vec{H}|$ as well as $\nabla|\vec{H}|$, we suggest that the change of $\nabla|\vec{H}|$ plays a critical role for **Figure 2.10**, for both MCs and single NR. This is confirmed in our theoretical model below.

Since the motion of the MCs is closely related to the applied f_H, it is important to systematically understand how f_H changes the motion speed v. By systematically increasing f_H while keeping $I_0 = 2\,\text{A}$, we obtained the relationship between v and f_H as shown in

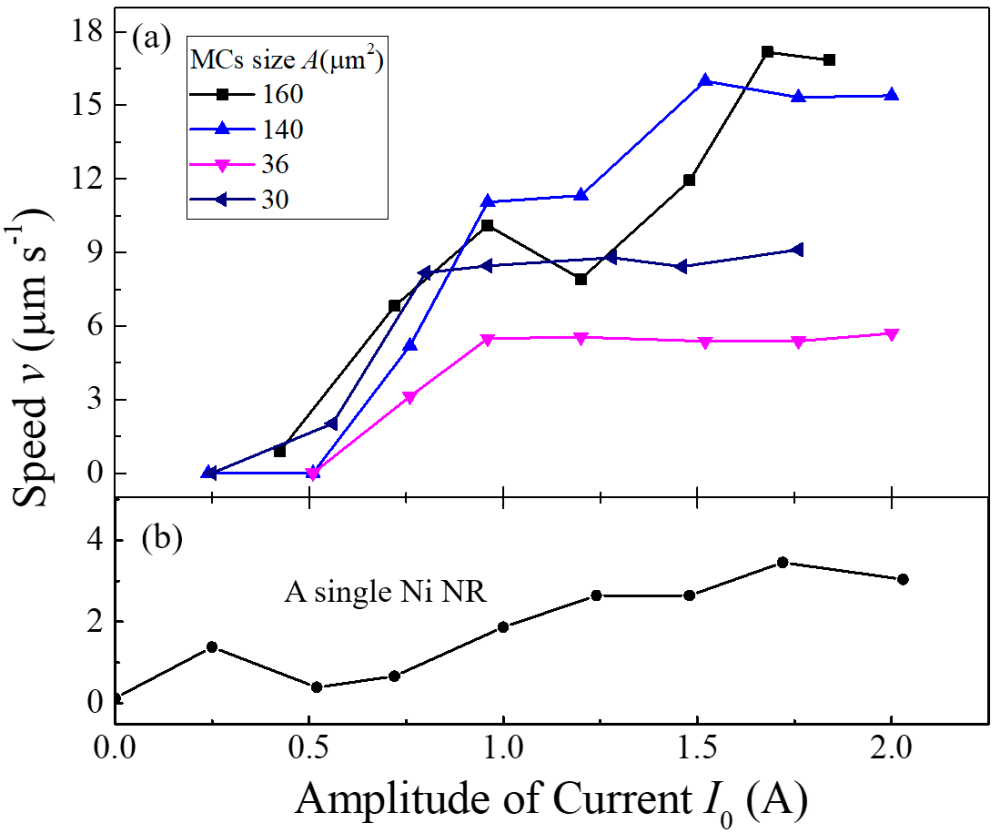

Figure 2.10: (a) The translational speed v of MCs and (b) a single Ni NR versus different I_0. Here $f_H = 10\,\text{Hz}$.

Figure 2.11. We find that such a relationship depends on the MC size. A statistical plot of v versus f_H for different sized MCs is shown in **Figure 2.11(a)**. For different sized MCs, the v verses f_H relationship follows a similar trend: when f_H increases initially, v increases dramatically; then v reaches a maximum value when f_H increases to a threshold value f_H^m; when f_H increases further, v gradually decreases, till it approaches to zero when $f_H > 140\,\text{Hz}$. The threshold frequency f_H^m depends on the MC's area A: f_H^m decreases when A increases. A similar relationship is also observed from a single magnetic NR as shown in **Figure 2.11(b)**. Though the speed of the magnetic NR is significantly smaller than that of the MCs. Such a frequency dependent relationship is closely related to how the MC could follow the change of the applied field, *i.e.*, how fast the magnetization $\vec{m}$ of the MC can follow $\vec{H}(t)$. We find that

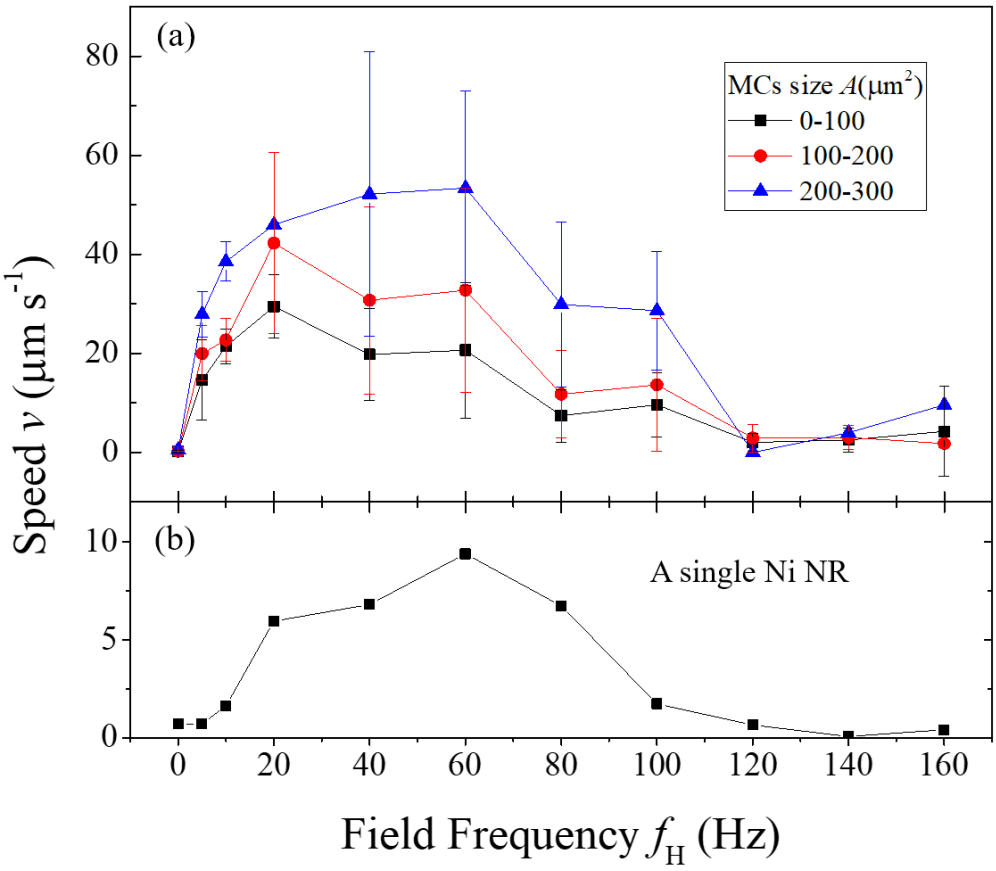

Figure 2.11: (a) The plot of the translational moving speed v of different sized MCs and (b) a single Ni NR as a function of nuAMF frequency f_H. Here $I_0 = 2\,\mathrm{A}$.

when f_H increases, especially when f_H is in the range of 100 Hz to 200 Hz, not all of the MCs are moving away from the solenoid. A large percentage of the MCs actually moves to the opposite direction. Statistics have been calculated on the moving direction of MCs, as shown in **Figure 2.12**. When the f_H is low ($f_H < 100\,\mathrm{Hz}$), most MCs (80% - 95%) are moving away from solenoid. When $f_H > 120\,\mathrm{Hz}$, the amount of MCs moving away from solenoid and the amount moving towards solenoid is about the same, $\sim 33\%$, while the other 33% MCs remain stationary. This statistic clearly demonstrates that at high f_H, MCs can hardly react to the field change.

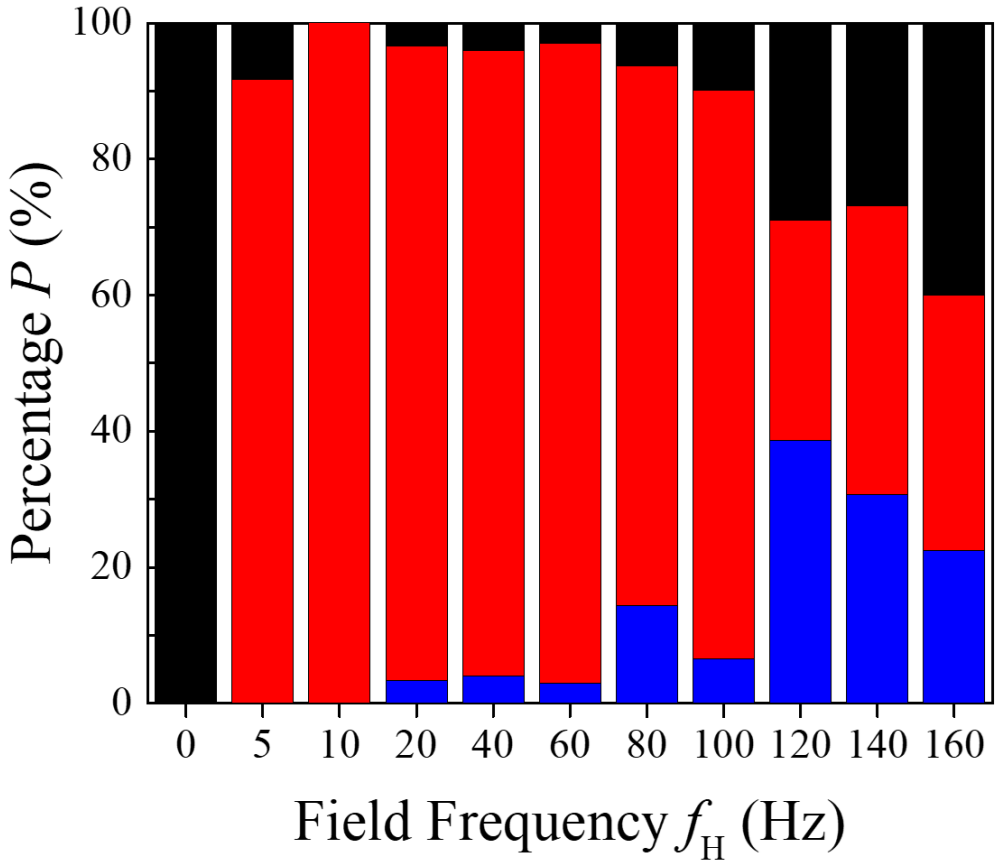

Figure 2.12: Statistics of the MCs' moving direction for different f_H. Black: not moving; Blue: moving towards solenoid; Red: moving away from solenoid. Here $I_0 = 2\,\mathrm{A}$ and a cluster will be classified as not moving when its speed is smaller than $1\,\mu\mathrm{m\,s^{-1}}$.

2.4 Theoretical explanations

According to classic hydrodynamic theory, if a MC is performing a rotational motion in a bulk solution, due to the small Reynolds number (the maximum Reynolds number is calculated to be less than 0.01 based on the cluster velocity shown in **Figure 2.11(a)**) and the symmetry of its rotation, its rotation should not induce a translational motion. However, if such a rotation occurs near a wall, the wall will break the rotational symmetry, and could induce a translational motion [69, 111]. According to our experiments, the MCs are very close to the bottom substrate (within $10\,\mu\mathrm{m}$ distance). Hence, the substrate is very likely to play an important role in the MCs' translational motion. Therefore, we hypothesize that such a

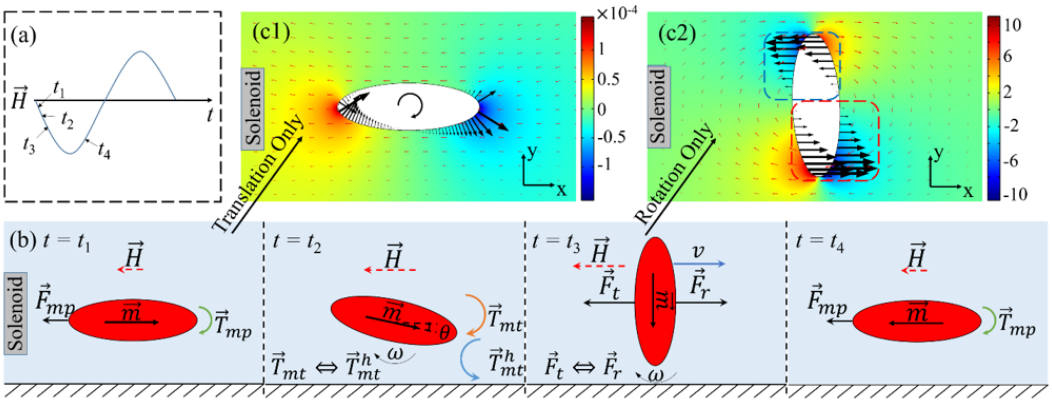

Figure 2.13: The translational and rotational motion of a MC driven by low-frequency nuAMF. (a) External alternating magnetic field as a function of time. (b) Force and toque analysis of a MC in an nuAMF. (c1-2) Pressure distribution on the MC surface at $t = t_1$ and t_3 moments. Initially, the magnetic moment of the MC aligns with the external $\vec{H}$. By time instant t_1, $\vec{H}$ changes to the new orientation, which is opposite to its original orientation. The MC experiences a magnetophoresis force $\vec{F}_{mp}$ pointing toward the solenoid. This $\vec{F}_{mp}$ induces a weak hydrodynamic torque $\vec{T}_{mp}$ on the MC, which drives it to rotate in the clockwise direction. Once the MC deviates from its original orientation, it experiences a magnetic torque $\vec{T}_{mp}$ caused by $\vec{H}$, which further drives its clockwise rotation. Consequently, the MC shows persistent rotation and moves away from the solenoid ($t = t_3$ and c2) as a surface walker [69] until it fully aligns with the external magnetic field $\vec{H}(t = t_4)$.

translational motion is caused by the nuAMF induced persistent out-of-plane rotation of the MC near a wall as shown in **Figure 2.13**.

A key observation from our experiments is that most of the MCs rotate in the same direction during their out-of-plane rotation. Typically, to induce persistent out-of-plane rotation of a magnetic cluster or chain in one direction, a rotating magnetic field is required. Non-rotating uniform alternating magnetic fields generally cannot independently induce persistent rotation in any direction. This is because once the MC becomes aligned with the external field, the magnetic torque exerted on it vanishes and the cluster maintains its orientation. When the alternating magnetic field reverts its direction, the MC can rotate either forward or backward depending on the thermal noise. However, the alternating magnetic field (non-rotating) used in our experiments is not uniform and has a non-zero gradient along its center axis. The symmetry of the rotation direction in an alternating magnetic field could

be broken by the non-uniformity of the field and cause persistent out-of-plane rotation of the MCs. Such a persistent rotation can be induced jointly by the magnetic torque and the magnetophoresis force in a nuAMF. To simplify the problem, we approximate the MC as a rigid ellipsoid with a permanent magnetic moment $\vec{m}$. **Figure 2.13(a)** shows the strength of the nuAMF used in the experiments during one period of AC input. When the MC is placed in an external magnetic field, it experiences a magnetic torque,

$$\vec{T}_{mt} = \mu_0 \vec{m} \times \vec{H} \,, \tag{2.1}$$

where μ_0 is the magnetic permeability of vacuum. Driven by this torque, the cluster will rotate till $\vec{m}$ is aligned with $\vec{H}$. As mentioned before, once the cluster is fully aligned with $\vec{H}$, $\vec{T}_{mt}$ will become zero. At this very moment, the out-of-plane rotation is driven by the magnetophoresis force and the hydrodynamic interactions between the MC and substrate, as shown in **Figure 2.13(b)**. The magnetophoresis force $\vec{F}_{mp}$ can be expressed as [112, 113],

$$\vec{F}_{mp} = \frac{1}{2}\mu_0 \chi_m V_p \nabla |\vec{H}|^2 \,, \tag{2.2}$$

where χ_m is the volume-averaged susceptibility. The direction of this magnetophoresis force is independent of the direction of the magnetic field and always points toward the solenoid as shown in **Figure 2.13(b)**. Because of the small magnetic fields applied in the experiments, this force is so small that the associated magnetophoresis velocity is at least an order of magnitude smaller than the translational velocity caused by the rotation. However, it can introduce a torque to rotate the MC through the hydrodynamic interactions between the MC and the substrate. As shown in **Figure 2.13(c1)**, when the cluster moves toward the solenoid, the pressure on the left side is higher than that on the right side. This unbalanced pressure induces a clockwise net torque $\vec{T}_{mp}$ on the cluster, thus forcing it to rotate in the clockwise direction. Hence, for an aligned cluster, when the magnetic field changes direction, the subtle

magnetophoresis force effectively steers the cluster to rotate in the clockwise direction and outweighs the effect of thermal noise. As a result, the cluster exhibits a persistent out-of-plane clockwise rotation.

Once we understand the cause of the MC's persistent out-of-plane rotation, we can analyze their translational motion as shown in **Figure 2.13(b)**. When $t < 0\,\mathrm{s}$, the cluster is fully aligned with the external magnetic field. By the moment of $t = t_1$, the direction of the external nuAMF changes by 180°, but the magnetic torque $\vec{T}_{mt}$ is close to zero. As explained above, steered by the magnetophoresis force $\vec{F}_{mp}$, the cluster slowly rotates in the clockwise direction. Once the cluster deviates from its original orientation ($t = t_2$), $\vec{T}_{mt}$ increases dramatically. This $\vec{T}_{mt}$ further drives the cluster to rotate in the clockwise direction, which tends to realign its $\vec{m}$ with the external $\vec{H}$. The hydrodynamic torque associated with this rotation (denoted by $\vec{T}^h_{mt}$) balances $\vec{T}_{mt}$ and the cluster is torque-free overall. During this realigning rotation ($t = t_3$), the hydrodynamic interactions between cluster and substrate generate a force $\vec{F}_r$ on the cluster due to the imbalance of the x-component of the pressure forces on the left and right portion of the MC's surface (see **Figure 2.13(c2)**). This $\vec{F}_r$ drives the MC to move away from the solenoid. The cluster's translational speed v is determined by the balance between the drag force $\vec{F}_t$ (induced by the translational motion of the MC), and the force $\vec{F}_r$ because the cluster is force-free overall. This translational motion of the cluster lasts until the cluster becomes fully aligned with the external $\vec{H}$ ($t = t_4$).

To validate our hypothesis, we simulated the actuation of an ellipsoidal magnetic rod by a nuAMF in two-dimensional space. For the low-frequency situation, a rigid elliptical magnetic rod with a major radius $R_a = 15\,\mu\mathrm{m}$ and a minor radius $R_b = 5\,\mu\mathrm{m}$ is placed $35\,\mu\mathrm{m}$ above the substrate. An external nuAMF is applied by a solenoid placed on the left-hand side with an input AC with the amplitude I_0. Initially, the $\vec{m}$ of the rod is aligned with $\vec{H}$, pointing in the positive x-direction, and the liquid around it is stationary. **Figure 2.14** shows the simulation results of cluster motion in one period of a nuAMF with $f_H = 20\,\mathrm{Hz}$

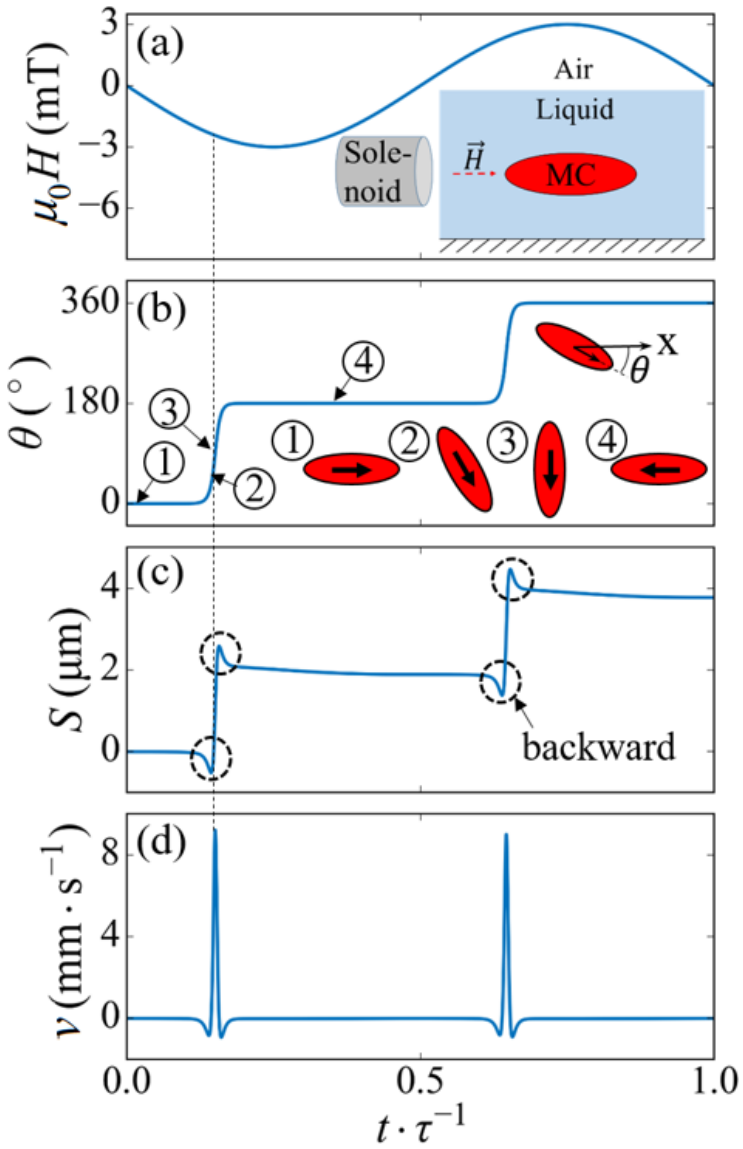

Figure 2.14: Simulation results of the motion of a magnetic cluster in one period of low-frequency nuAMF. (a) The external nuAMF. (b) The angle between the cluster's magnetic moment and the horizontal plane. (c) The cluster's displacement. (d) The cluster's translational velocity.

and $I_0 = 2\,\mathrm{A}$. In one AC period τ (0.05 s), the MC rotates 360° in a clockwise direction to realign itself with $\vec{H}$. **Figure 2.14(b)** shows the orientation of the rod as a function of the rotation time (the orientation angle θ is defined in **Figure 2.14(b)**). The rod shows two sharp angular changes in the clockwise direction near $t = 0.15\tau$ and 0.65τ, each corresponding

to a rotation of the rod by 180° to realign with the magnetic field $\vec{H}$. Note the duration of these rotations of the rod is short compared to the period of nuAMF $\vec{H}$. **Figure 2.14(c)** shows the x-direction displacement S of the rod from its original position during one period of nuAMF. The increase/decrease of S means the rod moves away/toward the solenoid. It is interesting to note that S only changes when θ changes, *i.e.*, the rod translates only when it rotates. During each clockwise rotation of the rod, the rod generally moves away from the solenoid (sharp increase of S) due to the hydrodynamic interaction between the rod and the substrate. Such rotation-depended translation of the rod exhibits a fluctuation in S with a $2f_H$ frequency similar to the experimental observation. Moreover, we note that the rod moves toward the solenoid with a small back step (see the decrease of S near $t = 0.15\tau$ and 0.65τ) at the beginning and end of each rotation process. Such a weak backward movement is caused by the imbalance of the pressure distribution on the rod's surface. This $2f_H$ translational movement of the rod also generates two spikes of translational velocity v in one period τ, as shown in **Figure 2.14(d)**.

Figure 2.15 shows the width W of the rod projected on the horizontal plane as predicted by our simulation and measured experimentally. Both results from simulation and experiment show two sharp downward spikes in one period of nuAMF, each corresponding to one 180° out-of-plane rotation of the rod. In contrast, when the rod is aligned with $\vec{H}$ its projected width remains close to the major diameter of the rod, similar to the observation from experiments (see **Figure 2.15(b)**'s inset).

The effects of current amplitude I_0 and field frequency f_H on the average translational speed v of the magnetic rod have also been studied. The simulation results of the translational speed v for different I_0 show a similar trend as the experimental observation as shown in **Figure 2.10**. **Figure 2.16(a)** shows that, when I_0 is small ($I0 \leq 0.5\,\mathrm{A}$), the rod exhibits no translational motion. This is because $\vec{H}$, and hence $\vec{F}_{mp}$, generated by the current is too weak to ensure that the rod keeps rotating in the same direction when the direction of the

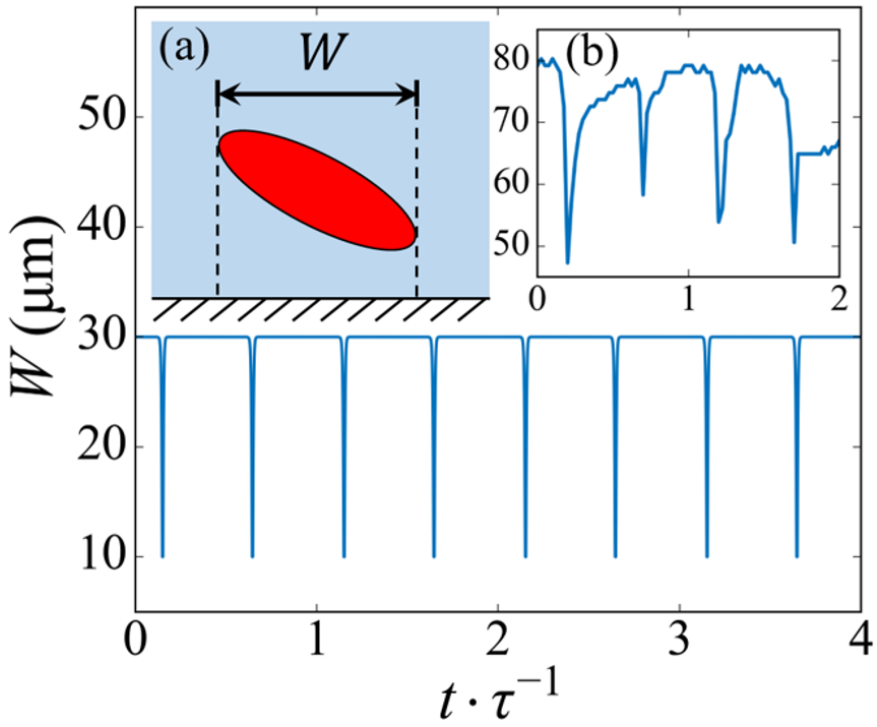

Figure 2.15: Evolution of the width of a magnetic cluster projected onto the horizontal plane over several periods of AC magnetic field ($f_H = 5\,\text{Hz}$ or $\tau = 0.2\,\text{s}$). Inset (a) show the definition of the projected width of the cluster. Inset (b) is the representative experimental result compared with simulation data. The two downward spikes correspond to the rapid alignment of the cluster with the external magnetic field once it rotates away from the 0° or 0° orientation (see **Figure 2.14(b)**). The projected width maintains its maximal value most of the time, indicating that the cluster is fully aligned with the low-frequency magnetic field studied here.

magnetic field changes. Once I_0 is large enough ($I_0 > 0.5\,\text{A}$), the rod starts to exhibit a persistent out-of-plane rotation and translates away from the solenoid. As the I_0 increases further, v deceases slightly due to the increase of $\vec{F}_{mp}$, which tends to drive the rod toward the solenoid. As shown in **Figure 2.16(b)**, the translational speed v of the rod increases linearly in the low to intermediate frequency regime ($0\,\text{Hz} < f_H < 60\,\text{Hz}$). Such a rapid raise of v is expected as higher f_H means more out-of-plane rotations of a cluster in the same time period. When f_H is too high, the translational motion of the cluster becomes weak, similar to the experimental observation as shown in **Figure 2.11**. This can be understood as follows.

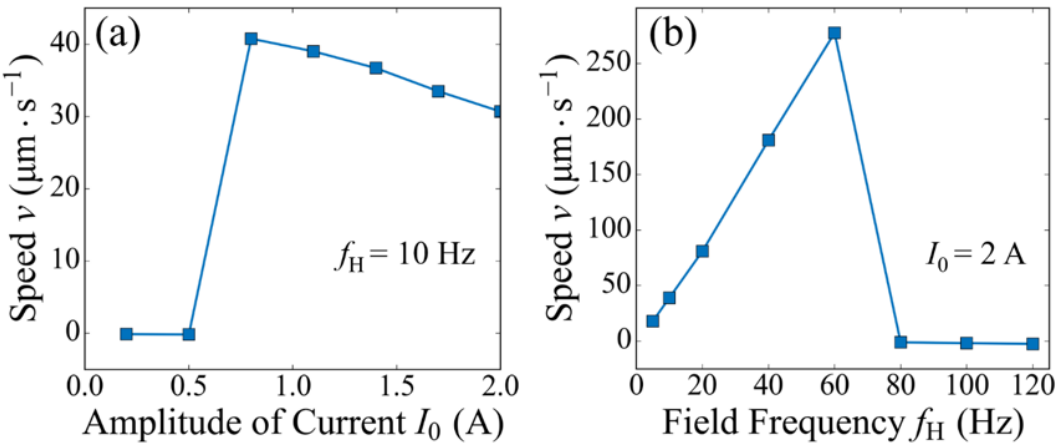

Figure 2.16: Effects of the amplitude of current I_0 (a) and field frequency f_H (b) of nuAMF on the translational velocity obtained from simulations.

In a nuAMF $\vec{H}$ with a sufficiently high frequency ($f_H \geq 80\,\text{Hz}$), the period of the nuAMF $\vec{H}$ is too short for the cluster to realign itself with the magnetic field. Specifically, before the cluster rotates 180° in a clockwise direction, it is forced to rotate back (counter-clockwise) toward its original orientation by the changing direction of $\vec{H}$. Hence, the cluster can no longer persistently rotate in one direction and its net translational motion is eliminated.

2.5 Control of the MNR motion

Previous sections discussed basic performance and mechanism of how the nuAMF can drive the translational motion of MCs. Since the MC can be controlled to move in one direction, it is possible to use 4 solenoids to control the motion of a MC in a 2D plane. Here, we will study the how the signal of nuAMF will control the translational motion of a single Ni MNR. A representative SEM image of such a Ni MNR is shown in **Figure 2.2(c)**. The motion control experiments were performed using a motion control system described in **Appendix B** with a fixed current amplitude $I_0 = 2\,\text{A}$. The effect of the nuAMF is characterized by two parameters: the translational motion's directionality and precision.

Based on previous sections, the MCs/MNRs will not exactly move along a single direction due to influence of Brownian motion (**Section 1.2.3**) and other unexpected fluctuation

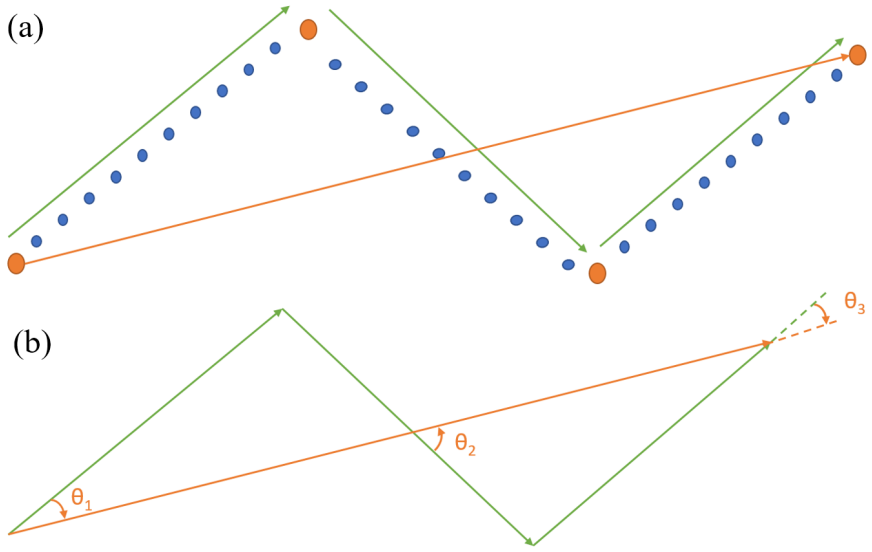

Figure 2.17: (a) Illustration of the trajectory of a MNR move under the nuAMF. (b) The definition of the directionality.

in the nuAMF signal. **Figure 2.17(a)** shows a small section of a MNR's trajectory data obtained from an experiment. Each blue data point represents a location of a MNR in a movie frame while the orange data points mark the locations separated by one nuAMF period ($1/f_H$). Direction of the EMF is represented using a orange vector ($\vec{B}$) and the green vectors ($\vec{s}$) represent the MNR's displacement during one nuAMF period. The angles between each green vector with respect to the orange vector are noted as $\theta_1, \theta_2, \cdots, \theta_n$, as shown in **Figure 2.17(b)**. The directionality D_d is defined as,

$$D_d = \frac{\cos\theta_1 + \cos\theta_2 + \cdots + \cos\theta_n}{n}\,. \tag{2.3}$$

When the MNR's translational motion exactly follows the direction of nuAMF, $D_d = 1$, indicating a prefect directionality. When the MNR preforms a random motion, $D_d = 0$.

2.5.1 The effect of continuum nuAMF signal

One immediate relationship we can build is to see how a continuum sinusoidal nuAMF signal affects the directionality of the MNR's motion. Since I_0 is fixed, the only parameter

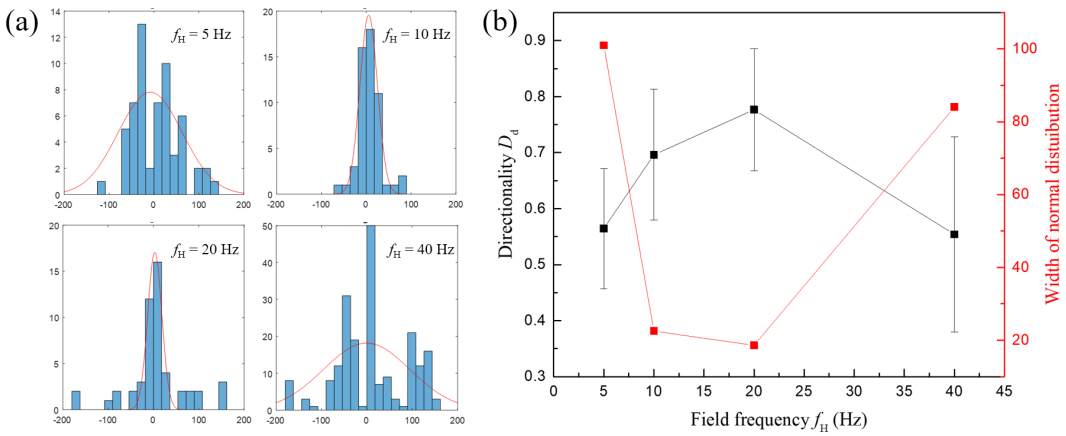

Figure 2.18: Experiment results of continues signal. (a) Histogram of the angle θ and the normal distribution fitting. (b) Plot of D_d verse f_H.

that can affect D_d is f_H. To study the relationship between D_d and f_H, we analyzed 10-second MNR trajectories under the nuAMF with $f_H = 5, 10, 20, 40$ Hz. **Figure 2.18(a)** shows the histogram of θ angle and the normal distribution fitting for each f_H. Over all, the average θ is around 0°, which is expected for a directional translational motion. However, the width of the distribution is different. It seems that the $f_H = 10$ Hz and 20 Hz situation give the smallest distribution width, which indicates the two cases result in better directionality. **Figure 2.18(b)** shows the relationships of the width of the θ distribution $\Delta\theta$ and D_d verse f_H. The result indicates that $\Delta\theta$ decreased while D_d increases when f_H increases from 5 Hz to 20 Hz, then $\Delta\theta$ increases and D_d decreases when $f_H > 20$ Hz. Clearly, $f_H = 20$ Hz gives the best directionality, $D_d = 0.8 \pm 0.1$. In fact, directionality D_d is also closely related to the moving speed v of the MNR. The displacement $\vec{s}$ of the MNR can be divided into two parts,

$$\vec{s} = \vec{s}_T + \vec{s}_B \,, \tag{2.4}$$

where $\vec{s}_T = vt$ is the displacement driven by the nuAMF and shall be parallel to direction of $\vec{B}$, while $\vec{s}_B = \sqrt{4Dt}$ is the displacement caused by Brownian motion and is randomly orientated. If $v = |\frac{d\vec{s}}{dt}|$ is very large, i.e. $|\vec{s}_T| \gg |\vec{s}_B|$, one can ignore the effect of Brownian motion and

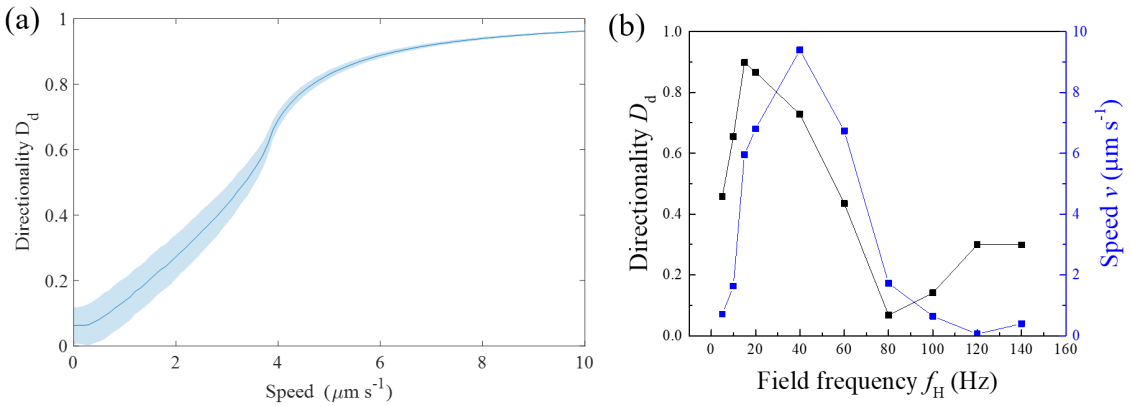

Figure 2.19: (a) Simulation of the D_d at different v. (b) Experiment result of D_d (black), and translational motion speed v (blue) verse f_H.

conclude that D_d approaches to 1. However, when $|\vec{s}_T| \ll |\vec{s}_B|$, D_d will approaches to 0. The relationship between D_d and v can be simulated using a Matlab program by assuming the MNR as a sphere, and the result is shown in **Figure 2.19(a)**. In the simulation, the directional motion parameters are taken from the experimental data of $f_H = 20\,\text{Hz}$, i.e., one period $t = 0.05\,\text{s}$, the diffusivity $D = 1.85 \times 10^{-1}\,\mu\text{m}^2\,\text{s}^{-1}$ is calculated using Equation (1.23) with a particle radius $r = 1.6\,\mu\text{m}$ at room temperature in water. The speed v is changed from 0 to $10\,\mu\text{m}\,\text{s}^{-1}$. The averaged D_d is taken from 1000 simulations, with each simulation consisting of 200 steps (so the total duration is 10 sec). Clearly, the directionality D_d is positively related to the MNR motion speed v. **Figure 2.19(b)** shows the experimental plots of D_d and v versus f_H for a Ni MNR, and D_d and v show a positive relationship with a small discrepancy. The optimal D_d is obtained at $f_H = 20\,\text{Hz}$, but the fastest moving speed v is located at $f_H = 60\,\text{Hz}$.

2.5.2 The effect of noncontinuous nuAMF signals

In order to control a MNR to move in a 2D-space, a discretized motion of a MNR in x-direction and y-direction is needed. In this case, a minimum moving distance in either x-direction or y-direction, i.e., the resolution of the translational motion, is critical. Since the discretized motion is controlled by an on/off signal of the driven nuAMF, the relative on/off

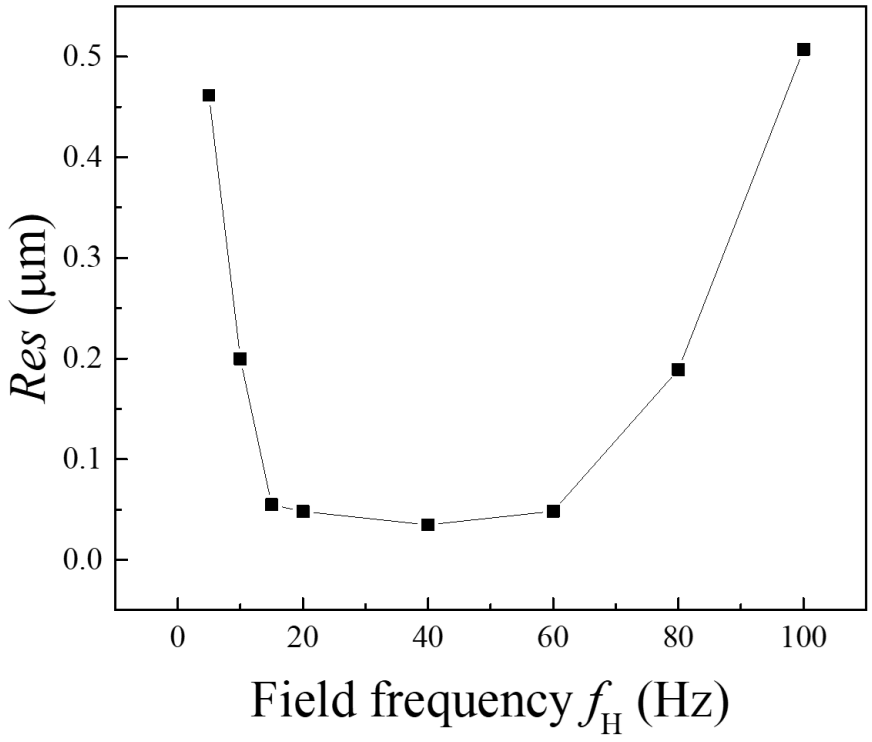

Figure 2.20: Theoretical estimation of the manipulation resolution under different f_H.

time of the signal becomes important. Equation (2.4) shows that the motion of the MNR is a combination of a translation motion and a Brownian motion. When these two kinds of motions contribute equally ($|\vec{s}_T| =< |\vec{s}_B| >$), one can obtain a critical time $t_c = \frac{4D}{v^2}$, in which a linear motion turns into a random motion. And the resolution of a linear motion could be defined as,

$$Res = t_c v = \frac{4D}{v}\,. \tag{2.5}$$

Figure 2.20 shows the theoretical estimation of the *Res* based on the experimental data in **Figure 2.19(b)**. The data points beyond 100 Hz are not showing here because the v approaches to 0.

The noncontinuous nuAMF signal was generated by applying a window function on a sinusoidal wave of frequency $f_H = 20$ Hz as shown in **Figure 2.21(a)**. The duration of the signal step is noted as t_s and the break between two steps is noted as t_0. To study how t_s

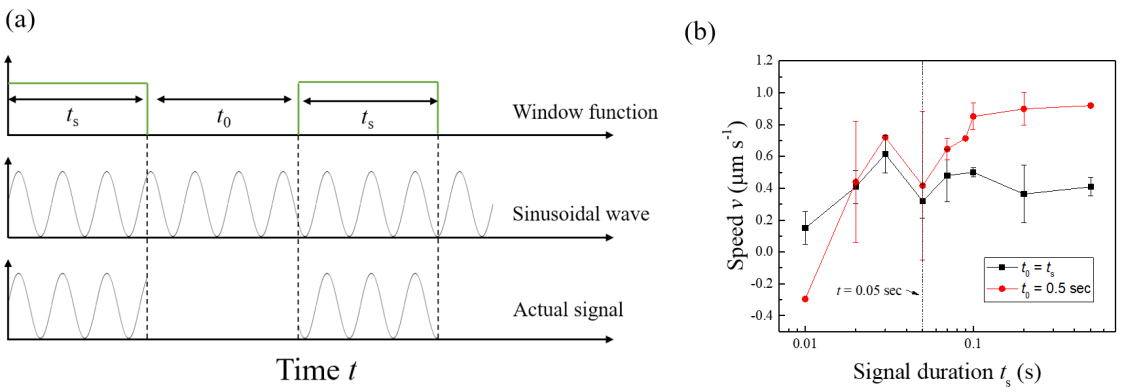

Figure 2.21: Motion study with noncontinuous nuAMF signal. (a) Illustration of the noncontinuous sinusoidal signal by applying a window function to a continues sinusoidal signal. (b) Plot of the motion speed v verse the duration of the signal t_s.

and t_0 would affect the translation motion, we performed experiments with: (1) $t_0 = t_s$. (2) $t_0 = 0.5\,\text{s}$. Experiment results of the speed v verse different signal duration t_s are shown in **Figure 2.21(b)**. One can see that when $t < 0.1\,\text{s}$, the speed v is closely depend on t_s. A local minimal was achieved at $t = 1/f_H = 0.05\,\text{s}$. In order to use the noncontinuous nuAMF signals to control the motion of a MNR, it would be best that the MNR's translational motion speed v is only depend on field frequency f_H. Thus, we concluded that both t_s and t_0 are need to be great than 0.1 s in order to achieve a stable translational motion.

2.5.3 Drawing letters using nuAMF

The ability of control a single MNR motion was experimentally demonstrated by drawing "UGA" letters with program-controlled signals as shown in **Figure 2.22**. The up-right corner shows the user pre-designed pattern which is a 32×32 pixel black-white image. A lab-developed Matlab program was used to read the pattern and generate appropriate noncontinuous step signals. Each pixel represents one $t_s = 0.2\,\text{s}$ signal with $f_H = 20\,\text{Hz}$ and the break between two steps is set to be $t_0 = 0.5\,\text{s}$. These parameters are choose because $f_H = 20\,\text{Hz}$ gives best directionality (**Figure 2.19(b)**) and $t_s = 0.2\,\text{s}, t_0 = 0.5\,\text{s}$ gives stable translational motion.

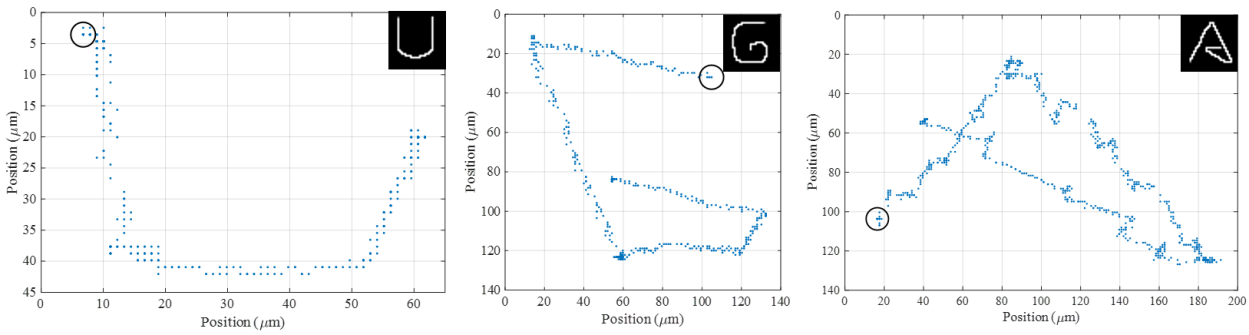

Figure 2.22: Write letters using program controlled signals with $f_H = 20\,\text{Hz}$, $t_s = 0.2\,\text{s}$, and $t_0 = 0.5\,\text{s}$.

2.6 Conclusions

In conclusion, we discovered a novel method to manipulate magnetic clusters near a solid surface using a nuAMF. Experiments show that MCs will move away from the solenoid, which is different from the case of a magnetic particle pulled toward a permanent magnet. Our systematic experimental results show that there are two necessary conditions for such a directional movement to happen. First, the magnetic field must be strong enough to rotate the MC. Second, the magnetic field must be non-uniform. The movement can be easily induced for geometrically more anisotropic particles. With further analysis, we found that the MCs' time dependent displacements show periodic behaviors and such behavior is closely related to twice the frequency of the driving field. The moving speed of the MCs also depends on the strength and gradient of the driving magnetic field, the frequency of the driving magnetic field, and the size of the MCs. A hydrodynamic model is developed to understand the mechanisms of the MCs' behaviors and the theoretical predications match our experimental results quite well. This directional manipulation method has advantages when compared to other manipulation methods. For example, it is easy and cheap to implement and requires much weaker magnetic field strength than traditional magnetic field manipulation methods. Such a simple particle manipulation method has a great potential in applications such as cell biology and microfluidics.

Chapter 3

Improving Stroke Treatment Through Enhanced Diffusion by Rotating Magnetic Nanorods

3.1 Introduction

As discussed in **Section 1.2.3**, when a RMF is applied, MNRs can be used to directly enhance the mass transportation (diffusion) of drug molecules in solution. For drugs that require bio-chemical reactions to function and the reactions are diffusion limited, such an enhanced diffusion is a practical way to improve the efficiency of the drug. This is because when the MNRs start rotating in solution, they can act as "stirrers" to stir surrendering fluid and accelerate the mobility of the reactant of reaction (drug) molecules as well as that of the reaction product. According to the collision theory, such a hydrodynamic effect will result in

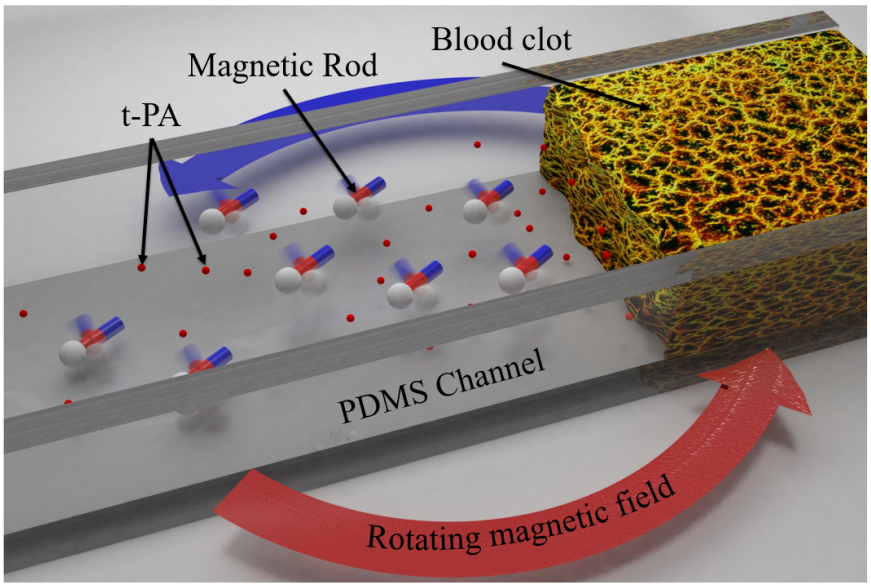

Figure 3.1: Schematic view of nanorod enhanced thrombolysis in fluidic channels. The Nickel MNR are dispersed in tPA solution and activated by a rotational magnetic field at the vicinity of a clot in a PDMS channel. The mass transport of tPA molecules are directly accelerated by the hydrodynamic flows induced by rotating MNRs.

an accelerated reaction rate to increase the effectiveness of the drug. The use of tPA to lysis blood clot is a good example since the blood clot lysis process (thrombolysis) by tPA is a diffusion limited chemical reaction.

In this chapter, we first confirm that under the normal administration of the tPA for a stroke patient, the thrombolysis process is a diffusion limited process at low tPA concentration ($C_{\mathrm{tPA}} \leq 60\,\mu\mathrm{g\,ml^{-1}}$). Therefore, in order to enhance the thrombolysis but keep the tPA concentration low, it is important to improve the mass transport process during thrombolysis. Such a mass transport enhancement can be achieved by rotating MNRs. Based on this idea, we have systematically designed experiments to study how MNRs can help tPA lysis blood clots as schematically illustrated in **Figure 3.1**.

3.2 Experiment methods

3.2.1 Fabrication of Ni nanorods

Here we used the magnetic Nickel nanorods fabricated by the OAD method to perform the enhanced diffusion experiments [106] as discussed in **Section 1.3.1**. Experimentally, a 500 nm diameter PS bead monolayer was formed on Si substrate using convective self-assembly method [114]. The coated beads were used as the nucleation site for the growth of Ni NRs. The bead-coated substrates were loaded into a custom built electron beam evaporation chamber. Nickel (Ni, 99.95%, Alfa Aesar, Ward Hill, MA) was deposited at a vapor incident angle of 86° and at a rate of $\sim 0.5\,\mathrm{nm\,s^{-1}}$, monitored by a QCM facing directly toward the incident vapor. Ni nanorods of length $\sim$1 µm were obtained when the QCM reading reached 2 µm, as shown in **Figure 3.2(a)**. The SEM image of the cross-section and an individual Nickel nanorod is shown in **Figure 3.2(b)** and **Figure 3.2(c)**, respectively. To prevent the aggregation of the nanorods in solution, the Ni rods on substrates were dipped in PVP (Polyvinylpyrrolidone, MW = 360 kDa, Sigma-Aldrich, St. Louis, MO) solution (w/w = 10%) for 24 hours. Then the substrates were sonicated for 1 min in another PVP (Polyvinylpyrrolidone, MW = 40 kDa, Sigma-Aldrich, St. Louis, MO) solution (w/w = 10%) for 30 sec. During the sonication, most

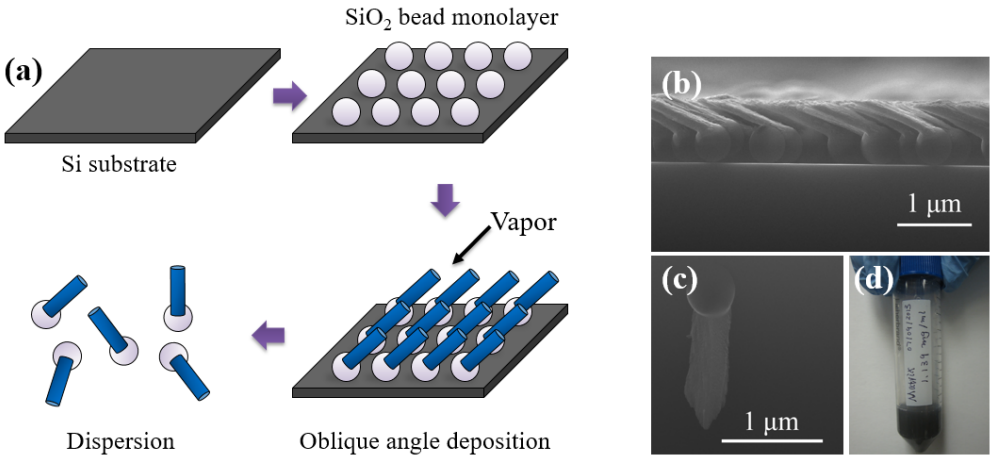

Figure 3.2: Nickel rods fabrication process using OAD and convective self-assembly methods. (a) Schematic process of fabrication indicated in clockwise direction: self-assembled monolayer of polystyrene beads on a cleaned silicon wafer; uniform nickel rods grown on beads using OAD method; rods washed into suspension of PVP. (b) Side view of nanorods on silicon substrate; (c) A single nanorod with a polystyrene bead; (d) Rods suspended in PVP (MW = 40 kDa) solution, forming a matrix of known concentration.

of the rods were released from the substrates and suspended in PVP solution to form a stable matrix as shown in **Figure 3.2(d)**.

The final concentration of the nanorods was determined by the weight difference of substrates before and after the sonication. Before each experiment, the rods in matrix were extracted by a strong permanent magnet, washed by water for 2-3 times and prepared to be mixed with reaction solutions.

3.2.2 *In-vitro* experiment setup

As shown in **Figure 3.3**, the *in-vitro* experiment setup consists of a magnetic field generator, a polydimethylsiloxane (PDMS) plate with test samples inside, a light pad, and a data acquisition system. Particularly, the RMF was generated by four solenoids (Air-core Solenoid #14825, Science Source, Waldoboro, ME), which were connected to two independent power supplies and controlled by a computer. The PDMS plate was suspended in the center of the solenoids by a glass slide with printed scales (green-dash lines), and was placed above

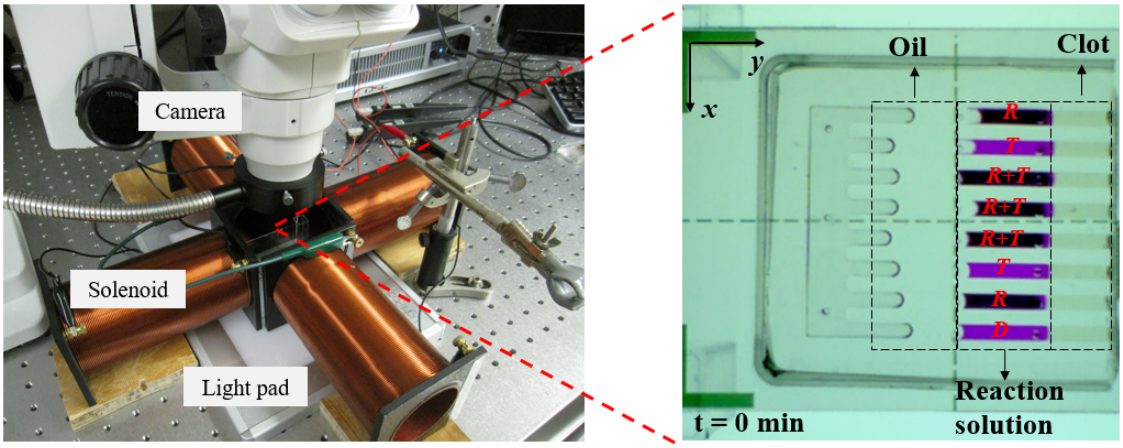

Figure 3.3: Left: *In-vitro* experimental setup consisting of the magnetic field generator, light pad, PDMS plate, and a microscope. Right: a zoom in image of a PDMS channel with clot in experiment.

a light pad (LightPad A920, Artograph, Delano, MN) which could provide a uniform and stable white light illumination for quantitative data extraction. The experimental data were obtained by a digital camera (Infinity 1, Lumenera Corp, Ottawa, Canada) monitoring PDMS channel from the top.

3.2.3 PDMS channel fabrication and artificial blood clot preparation

Both *in-vitro* clotting and thrombolysis were performed in a 8-channel microfluidic plate fabricated by PDMS. The PDMS was mixed with the solidify agent and poured in an aluminum mold after degassing in vacuum. Cured in an oven at 72 °C for 2 hours, the PDMS plate was peered off from the mold. Then, it was covalently bonded with another blanket flat PDMS plate to form the experimental plate with 8 comb-like $2 \times 1\,\text{mm}^2$ rectangular channels as shown in **Figure 3.4(a)**.

Two rows of 1 mm diameter holes were punched at 10 mm and 20 mm from the open ends. The first row of holes was used to inject the reaction solution and the second row was used for the injection of the mineral oil to seal the reaction solution inside the channels and prevent evaporation of reaction solution. To fabricate length-controlled clot in the PDMS channels, all the reagents and the channels were cooled in an ice box at 0 °C for 15 min. Then,

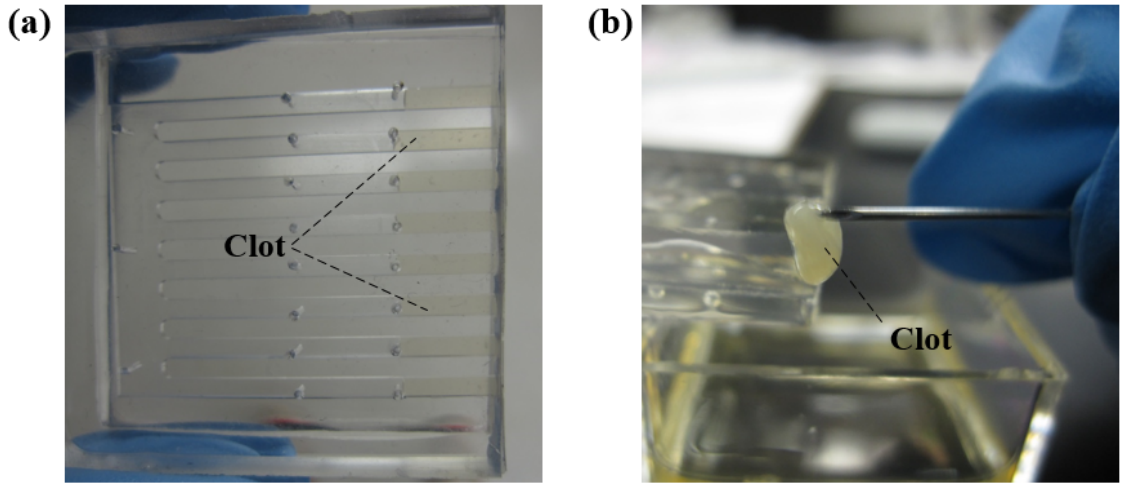

Figure 3.4: Fabricating clot inside PDMS channels. (a) PDMS channels plugged with clot, shown as light-yellow segments. (b) A clot pricked from a PDMS channel after fully reacted.

80 µl 1 µM human thrombin (Thrombin from human plasma, Sigma-Aldrich, St. Louis, MO) was added to 1 ml HPPP (Human Platelet Poor Plasma, Innovative Research, Novi, MI), mixed by vortex. Since the enzyme catalytic reaction was slowed down at the low temperature, the mixture remained as a flow-able "clot" in about 1 min. Within such a time scale, a 20 µl mixture of thrombin and HPPP was injected from the end of each channel one by one to form a 10 mm long clot. Once the mixture was injected in the channels, it could not flow out due to the capillary force. Then the plate was immediately suspended in a pool of 4 ml HPPP at 37 °C for 20 min. This allowed the residual agents in channels continue reacting with HPPP sufficiently and reinforce the clot structures. **Figure 3.4(b)** shows a tangled clot when it is removed from a channel after fully reacted. After this process, the open ends of the device were sealed by epoxy and ready for the injection of reaction solution. The dye added to all the reaction solution was Rhodamine B (RDB, HPLC, Sigma-Aldrich, St. Louis, MO). The tPA solution was liquefied from its lyophilized powder (Alteplase, Genentech, South San Francisco, CA).

3.2.4 Data treatment method

In-vitro experimental data were obtained by a digital camera (Infinity 1, Lumenera Corp, Ottawa, Canada). Image J software (National Institutes of Health, Bethesda, MD) was used to decompose images into Red, Green, and Blue color channels. The boundaries of liquid/clot were identified based on the grayscale value of images in the green channel since RDB absorbs most of the green light and maximized the contrast. It is assumed that the transmitted green light intensity I follows Beer's Law,

$$\frac{I}{I_0} = e^{-alc}, \tag{3.1}$$

where I_0 is the incident green light intensity before the PDMS channel filled with RDB solution, c is the RDB concentration, α is the absorption coefficient, and l is the thickness of RDB solution, or the height of the channel. The grayscale of the image should be proportional to the transmitted light intensity,

$$\frac{G}{G_0} = \frac{I}{I_0} = e^{-alc}, \tag{3.2}$$

where G and G_0 are the corresponding grayscale values of the green channel of the video image. A calibration curve was produced using known concentrations of dye solution in PDMS channels as shown in **Figure 3.5(c)**. During the thrombolysis process, the grayscale value G of each channel was first averaged in y-direction,

$$G(x) = \frac{1}{h}\sum_{y} G(x, y), \tag{3.3}$$

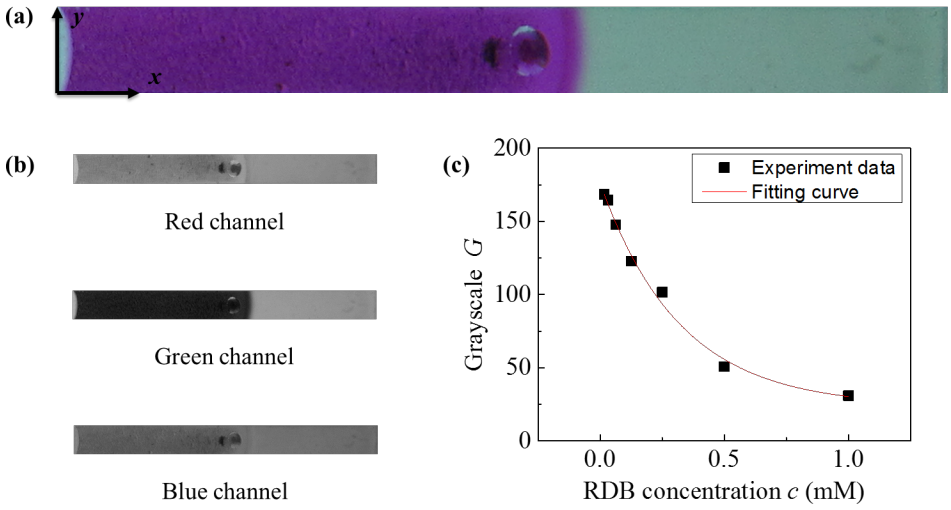

Figure 3.5: Data treatment process of *in-vitro* experiments. (a) Original image of a Dye+MNR channel at the beginning of the experiment with x-y coordinate definition. (b) The individual RGB color channel of the original image. (c) The calibration curve of the grayscale of the green channel G *vs.* RDB concentration c.

where h is the height of the image or channel width. Thus, G is a function of x coordinate only. The concentration of RDB is able to be estimated by,

$$c\left(x\right) = -\frac{1}{al}\ln\frac{G\left(x\right)}{G_0}\,. \tag{3.4}$$

The boundary between the reaction solution and clot interface X_{boundary} is defined at where $\frac{dc}{dx}$ reaches the maximum value. The clot dissolving speed can be extracted by liner fitting of function $X_{\text{boundary}}(t)$ versus time t.

To obtain the diffusion coefficient of RDB, the concentration curve at different time $c(x,t)$ was smoothened by averaging the five neighboring data points (5-point average) except at the two boundaries,

$$c_{smooth}\left(x,t\right) = \frac{1}{5}\sum_{x-2}^{x+2} c\left(x,t\right). \tag{3.5}$$

Since the solution of 1D diffusion equation $\frac{\partial c(x,t)}{\partial x} = D\frac{\partial^2 c(x,t)}{\partial x^2}$ is an error function,

$$c\,(x,t) = A\int_{\frac{x}{\sqrt{Dt}}}^{\infty} e^{-y^2}dy\,, \tag{3.6}$$

it indicates that the first derivative of c with respect to x should follow a Gaussian distribution,

$$\frac{\partial c\,(x,t)}{\partial x} = Ae^{-\frac{x^2}{Dt}} = Ae^{\frac{(x-\mu)^2}{\sigma^2}}\,. \tag{3.7}$$

Thus, the derivative $\frac{\partial c_{smooth}(x,t)}{\partial x}$ could be fitted by a Gaussian function, and the width of the Gauss function follows,

$$\sigma^2 = Dt\,. \tag{3.8}$$

Therefore, the diffusion constant D was obtained by linear fitting of σ^2 versus time t.

3.3 A simple reaction model on thrombolysis process

In plasma with absence of fibrin, tPA activates the plasminogen into plasmin at a very low efficiency and the plasmin cannot survive in plasma due to its strong affinity to the plasmin inhibitor. However, the lysine sites on fibrin attract both tPA and plasminogen molecules and assemble them on fibrin surface where the plasminogen can be activated by tPA at a high efficiency. Furthermore, the activated plasmin can be protected from the plasmin inhibitor in plasma [115–119]. Eventually, the fibrin is cleaved by plasmin into a soluble product. This complicated reaction process can be treated as a classic mass transport governing reaction process and it could be simplified into three sub-process as illustrated in **Figure 3.6**: (1) tPA molecules (T) diffuse to the fibrin surface and bind onto fibrin lysine sites (S) to form tPA-lysine complex (ST); (2) tPA-lysine complex (ST) activates plasminogen into plasmin which cleaves fibrin into soluble product (P); and (3) Product (P) desorbs from the fibrin

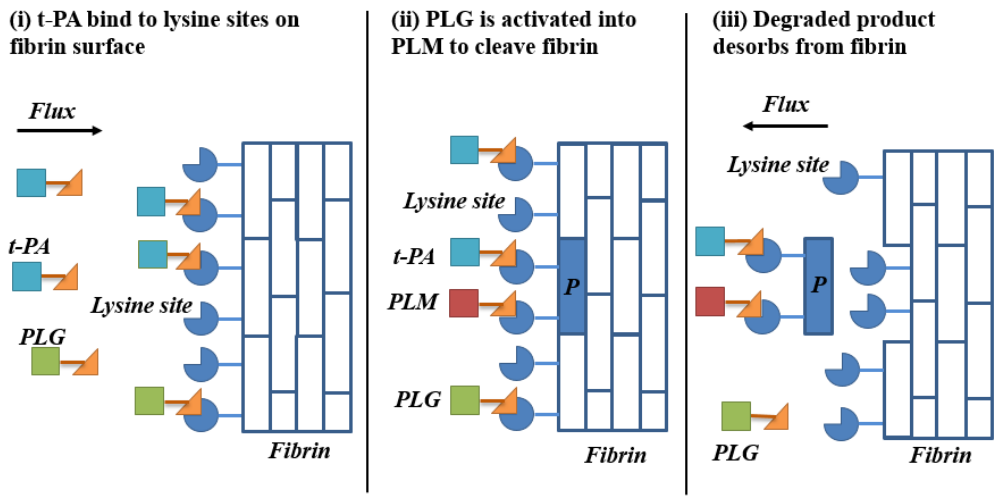

Figure 3.6: Simplified schemes of tPA mediated thrombolytic reaction on clot surface: (i) tPA and plasminogen molecules (PLG) diffuse to clot surface and bind to lysine sites. (ii) PLG molecules on the fibrin surface are activated into plasmin (PLM) by the neighboring tPA molecules. PLM molecules start to cleave the local fibrin fiber into soluble products (P). (iii) Lysis molecules P leave fibrin surface and expose new lysine sites.

surface and exposes new lysine sites. The entire process can be expressed in Equation (3.9),

$$S + T \xrightarrow{\kappa_T} ST \xrightarrow{\kappa_{TP}} SP \xrightarrow{\kappa_P} S + P\,, \tag{3.9}$$

where κ_T is the adsorption rate of tPA molecules on the fibrin surface and κ_P is the desorption rate of product P removing from the fibrin surface. The process $ST \to SP$ involves multiple steps of bio-chemical reactions. We assume that this translation process is very fast and the intrinsic reaction rate is characterized by κ_{TP}. In another word, $\kappa_{TP} \gg \kappa_T$ and $\kappa_{TP} \gg \kappa_P$. The thrombolysis rate is determined by how fast the sub-processes (1) – (3) happen sequentially and is dominated by the slowest sub-process. When the reaction reaches a steady state, the thrombolysis speed is proportional to the reaction rate of desorbed product molecule P, and can be mathematically expressed as,

$$\frac{dN_P}{dt} = \frac{\kappa_T \kappa_P \kappa_{TP}}{\kappa_T \kappa_{TP} + \kappa_{TP} \kappa_P + \kappa_P \kappa_T}\,, \tag{3.10}$$

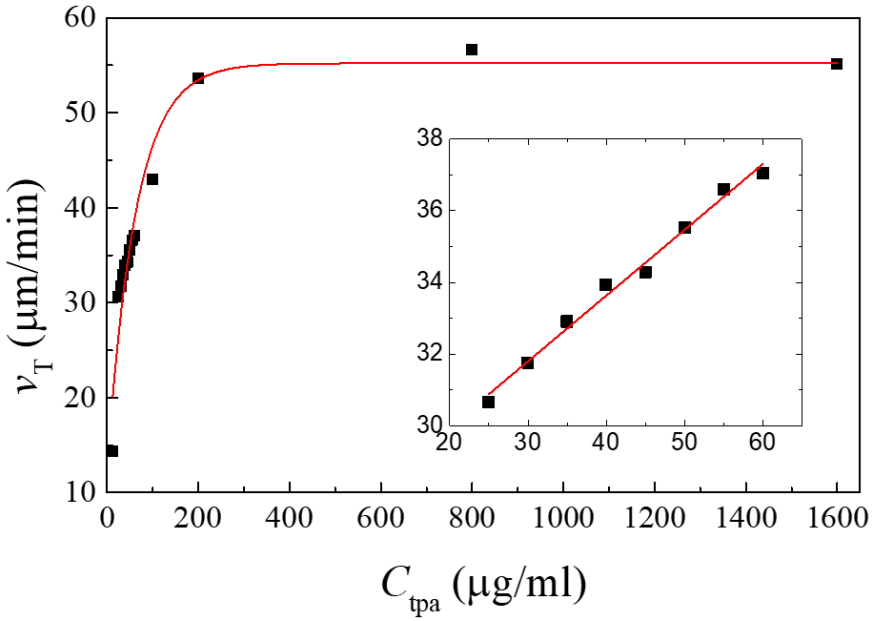

Figure 3.7: The clot boundary moving speed v_{T} versus the tPA concentration C_{tpa}

where N_P is the number of product molecule P. For different C_{tPA}, the overall thrombolysis could either belong to a diffusion limited (κ_T is low) reaction or a reaction limited (κ_P is slowest) process. The rate of diffusion limited reaction would depend closely on the C_{tPA}, while a reaction limited process will be independent on the C_{tPA}. To confirm whether our current experiment condition ($C_{\mathrm{tPA}} = 50\,\mu\mathrm{g\,ml^{-1}}$) belongs to a diffusion- or reaction- limited process, we have conducted a systematic experiment in the eight channels of our fluidic system to establish the relationship between the clot lysis speed (v_T) and C_{tPA}. The result is shown in the **Figure 3.7** below. From **Figure 3.7**, when $C_{\mathrm{tpa}} \geq 200\,\mu\mathrm{g\,ml^{-1}}$ we can see that the clot lysis speed $v_{\mathrm{T}} = 55\,\mu\mathrm{m\,min^{-1}}$ and it reaches a maximum value. At $C_{\mathrm{tpa}} = 50\,\mu\mathrm{g\,ml^{-1}}$, the clot lysis speed v_{T} is about $35\,\mu\mathrm{m\,min^{-1}}$ and depends strongly on C_{tpa}, which is a clear demonstration of a diffusion limited reaction process, *i.e.*, the transport (diffusion) of tPA to the surface of clot is the slowest step to determine the overall reaction rate. Thus with

$\kappa_P \gg \kappa_T$ and $\kappa_{TP} \gg \kappa_T$, Equation (3.10) can be reduced to,

$$\frac{dN_P}{dt} = \kappa_T \,. \tag{3.11}$$

Therefore, the tPA molecular mobility or the diffusion coefficient can be enhanced through the rotating MNRs, thus leads to enhanced reaction rate. If each molecule P produced in the thrombolysis frees a volume V_P from the solid clot, then the thrombolysis speed observed in the channel can be expressed as,

$$V_{R+T} = \frac{V_P}{A_c\,(1-\Phi)}\kappa_T \,, \tag{3.12}$$

where A_c is the cross-section area of the PDMS channel, Φ is the porosity of clot, and both can be assumed to be a constant. According to Equation (1.27), the reaction rate κ_T for a diffusion-limited reaction is given by,

$$\kappa_T = k_D C_{\text{tPA}} = 4\pi D_{\text{tPA}}\,(R_{\text{tPA}} + R_{\text{site}})\,C_{\text{tPA}} \,, \tag{3.13}$$

where D_{tPA} is the effective diffusivity of tPA enhanced by rotating MNRs, R_{tPA} and R_{site} are the radii of tPA molecules and lysine sites.

As discussed in **Section 1.2.3**, tPA's diffusivity D_{tPA} can be enhanced by rotating MNRs, as well the thrombolysis reaction rate. To estimate this effect, we first combine Equations (1.28) to (1.33), and consider experiment conditions such as MNR's length $L = 1\,\mu\text{m}$, diameter $d = 0.5\,\mu\text{m}$ and the RMF's frequency $f = 20\,\text{Hz}$, one can have $Pe \propto C_R^{1/3}$ and Pe varies from 1.6 to 3.1 when C_{Rod} changes from 1 to $7\,\text{mg}\,\text{ml}^{-1}$. According to the convection enhanced diffusion theory as discussed in **Section 1.2.3**, when the Peclet number Pe is small ($Pe < 3$), the flow scaling law is valid for rigid-boundary conditions and the enhanced diffusivity can be estimated as $D_{\text{tPA}} = D^T_{\text{tPA}}\,(1 + aPe^2)$, where a is a constant

($= \frac{2}{3\pi^2}$ in a spatially periodic hydrodynamic flows [120]). Since $Pe \propto C_R^{1/3}$, considering Equations (3.12) and (3.13) the clot boundary moving speed can be estimate as,

$$v_{R+T} = v_T + \alpha C_{\text{Rod}}^{2/3}\,, \tag{3.14}$$

where $v_T = \frac{4\pi(R_{\text{tPA}}+R_{\text{site}})V_P}{A_c(1-\Phi)} C_{\text{tPA}} D_{\text{tPA}}^T$ is the tPA mediated thrombolysis rate without MNRs in the channel, and is proportional to the concentration and thermal diffusivity of tPA. α is a parameter related to the enhancement of thrombolysis and can be obtained experimentally.

3.4 Enhanced tPA reaction by rotating MNRs

3.4.1 *In-vitro* experiment with PDMS channel plate

As schematically illustrated in **Figure 3.1**, we have proposed a strategy to mix tPA solution with MNR suspension, and to rotate the MNRs remotely by a RMF to improve the efficiency of tPA. Here we experimentally demonstrate that the rotating MNRs can enhance the tPA thrombolysis speed through enhanced mass transport. The magnetic rods used in this proof-of-principle study were Nickel MNRs fabricated by OAD method (**Section 1.3.1**) and suspended in PVP as shown in **Figure 3.2**.

To test the effect of rotating MNRs, four different solutions were injected to the PDMS channels at where marked as "Dye+X" in **Figure 3.8(a)**. There were: dye solution, denoted as "D"; tPA mixed with dye solution, denoted as "T"; MNR-dye mixture solution, denoted as "R"; and dye, tPA, and MNR mixture solution, denoted as "R+T", as shown in **Figure 3.8(b)**. The C_{tPA} in "T" and "R+T" channels is designed to be the same, $50\,\mu\text{g}\,\text{ml}^{-1}$. In both "R" and "R+T" channels the MNR concentration C_{Rod} has been changed systematically from 1 to $12.5\,\text{mg}\,\text{ml}^{-1}$. **Figure 3.8(b)** also shows the representative snapshots of the moving tPA and clot interface at different time for $C_{\text{Rod}} = 7\,\text{mg}\,\text{ml}^{-1}$. At the tPA/clot interfaces, all interface fronts in the "R" and "D" channels remain almost fixed while the interfaces at all the "T" and "R+T" channels advance to the right. It is observed that the interfaces of the "R+T" channels

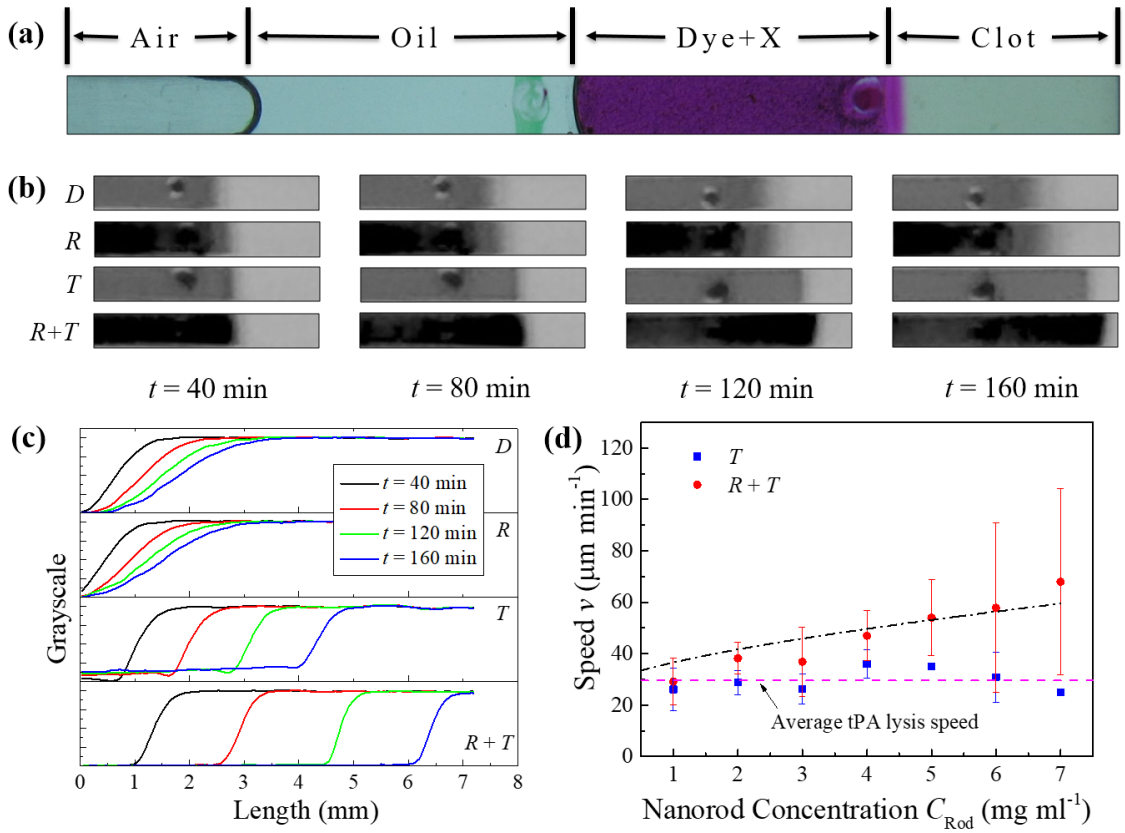

Figure 3.8: Results of *in-vitro* experiments: (a) A representative PDMS channel structure, where "X" represent different mixture. (b) Video clips of green-channel images at the liquid/-clot interface in "D", "R", "T", "R+T" channels (from top to bottom), at different thrombolysis time t = 40, 80, 120, and 160 min (from left to right), respectively. (c) The plot of gray scale versus PDMS channel location in (b). (d) Clot boundary moving speed v_T and v_{R+T} versus MNR concentration C_{Rod}. The blue solid square represents v_T and the red solid circle represents v_{R+T}. The pink dash line is a guide to eyes, and black dash-point curve is a fitting curve based on the proposed theoretical model.

move faster than those of the "T" channels. **Figure 3.8(c)** plots the one-dimensional grayscale distribution of dye along four representative channels at four different time. The lysis speed in each channel was assumed to be proportional to the boundary moving speed. For both the "D" and "R" channels, the gray scale profiles shows diffusion like behavior. The boundaries move slightly, but the profiles become more broadened. From the width versus time plot in "D" channel, we can extract the diffusion coefficient of dye to be $27.7 \pm 0.6\,\mu\text{m}^2\,\text{s}^{-1}$. For the "R" channel, the obtained diffusion coefficient to be $42.4 \pm 0.6\,\mu\text{m}^2\,\text{s}^{-1}$, which is slightly

larger than that in "D" channel. This is an indication of rotating MNRs enhanced molecular diffusion. For both "T" and "R+T" channels, the gray scale profile maintains its overall shape, but advances to the right quickly. Clearly, the "R+T" profile advances faster than the "T" profile. In fact, for $C_{\text{Rod}} = 7\,\text{mg}\,\text{ml}^{-1}$, the average thrombolysis speed v_T for "T" channel is $24.8 \pm 0.5\,\mu\text{m}\,\text{min}^{-1}$, and the average enhanced thrombolysis speed v_{R+T} in "R+T" channel is $68 \pm 36\,\mu\text{m}\,\text{min}^{-1}$, as shown in **Figure 3.8(d)**. This speed is close to the maximum lysis speed at very high tPA concentration ($C_{\text{tPA}} > 100\,\mu\text{g}\,\text{ml}^{-1}$) as shown in **Figure 3.7**. By varying the MNRs concentration C_{Rod} and keep all the other conditions constant, one observes that the thrombolysis speed v_{R+T} increases monotonically as a function of rods concentration C_{Rod}. **Figure 3.8(d)** plots v_T and v_{R+T} versus C_{Rod}. One can see that at different C_{Rod}, v_T fluctuates within $29 \pm 6\,\mu\text{m}\,\text{min}^{-1}$ while v_{R+T} increases monotonically with C_{Rod}. The enhanced thrombolysis rate v_{R+T} could be estimated using Equation (3.14) as shown by the dash-dotted fitting curve in **Figure 3.8(d)**. and we obtain $v_T = 28 \pm 2\,\mu\text{m}\,\text{min}^{-1}$ and $\alpha = (9 \pm 2) \times 10^{-4}\,\text{ml}\,\text{mg}^{-2/3}\,\text{min}^{-1}$.

This enhanced thrombolysis rate v_{R+T} could be due to two possible reasons: (1) mechanically rupture the clot network, or (2) the enhanced mass transport of tPA and lysis products caused by MNR rotation. Both our experimental observation and theoretical estimation based on the force/torque induced by the MNRs and mechanical properties of fibrins suggested that the mechanical induced rupture is too weak to break the clot fiber. Experimentally, there is always a control channel only with MNRs in our experiments like channel "R" in **Figure 3.8(b)**. In this channel, a lysis process has never been observed. Instead, a diffusion process has always been observed as we described before. **Figure 3.9(a)** shows the first derivative of dye concentration profile and the corresponding Gaussian fittings of "R" and "D" channels in **Figure 3.8(b)**. The parameter μ describes the central location of the Gaussian curve and could be treated as the position of clot/dye diffusion boundary. **Figure 3.9(b)** shows the plot of μ versus time t and simple linear fittings are given. Ac-

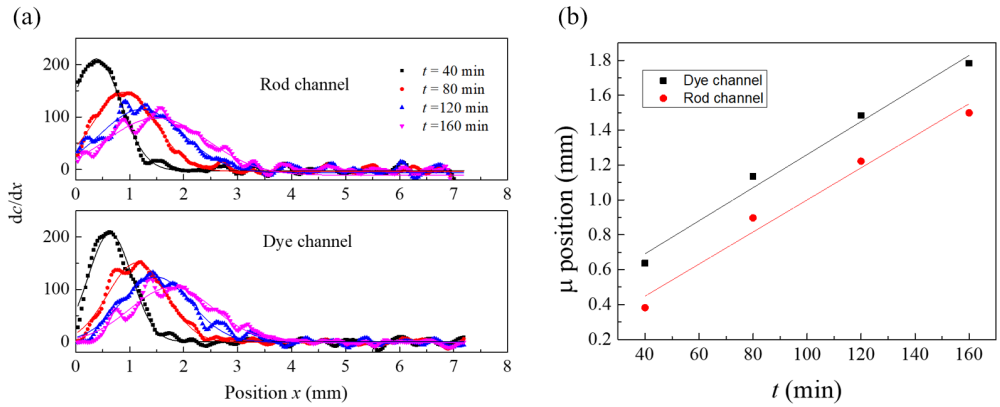

Figure 3.9: Mechanical interaction between MNRs and clot. (a) Change rate of dye concentration along the clot region. (b) Plot of the position of clot interface versus time t.

cording to **Figure 3.9(b)**, the clot/dye boundary is moving in both "D" and "R" channels, and has almost the same speed (about $9\,\mu m\,min^{-1}$). This speed is coming from the staining process of clot since the clot is light yellow color and the stained clot appears a darker color than the dye solution. So the central location of the Gaussian curve will move accordingly. However, this does not mean that the clot is being dissolved. If the mechanical stimulation could enhance the clot lysis, we should expect a very different boundary moving speed in the "R" channel from in the "D" channel (a large slope in **Figure 3.9(b)**), which is not the case in our observation.

Theoretically, the mechanical force on a fibrin fiber by a rotating rod can be estimated using Equation (1.5) if the Ni MNR is modeled as a point-like magnet. The torque is of the maximum magnitude when the dipole moment and the external magnetic flux are perpendicular to each other, and equal to zero when they are aligned with each other. The maximum torque is given by $T_{max} = MVB$, where V is the volume of the MNR. The M is the saturation magnetization of crystalline Ni which is about $58.5\,emu\,g^{-1}$ [121], and that of amorphous Ni is about one half of the value [122]. The mass density of Ni is $8900\,kg\,m^{-3}$. For a Ni MNR with length $l = 5\,\mu m$ and diameter $d = 0.2\,\mu m$, the volume, $V = 50.157\,\mu m^3$. Let us assume $B = 0.1\,T$, which is an overestimation in comparison to the field used in our

experiments ($B = 8\,\mathrm{mT}$). Substituting all these parameters (note M set to be $32.9\,\mathrm{emu\,g^{-1}}$ for amorphous Ni), we can estimate $T_{max} = 4.60\,\mathrm{fN\,m}$. It means that for the characteristic length scale down to the fibers of a fibrin clot, which should be ∼micron, such a MNR/clot interaction can generate forces on the order of Nano Newton. On the other hand, according to the literature, it takes about $100\,\mathrm{pN}$ to unfold a fibril [123], and several thousands of parallel fibrils can be counted in a fiber cross section [124]. It means that it would take a force of $\sim 1\,\mu\mathrm{N}$ to cause any damage to a fibrin fiber. As estimated above, the Ni MNR can only exert a force about $1\,\mathrm{nN}$. Thus, these MNRs cannot do any damage to individual fibers. Therefore, from both experimental and theoretical analyses, we could conclude that the mechanical interaction between the MNRs and clot could hardly play an appreciable role in our present experiments of tPA mediated thrombolysis. Since at $C_{\mathrm{tPA}} = 50\,\mu\mathrm{g\,ml^{-1}}$, the thrombolysis process is mass transport limited, while the rotation of the MNRs could induce local convection flows to enhanced reactant diffusion. It is very likely that the observed enhanced thrombolysis speed is caused by the enhanced mass transport as illustrated in **Figure 1.12**.

Our model (Equation (3.14)) also indicates that the rotation of the MNRs near the clot/solution interface in fact should be more effective compared to locations far away from the interface. This means if the local concentration of the MNRs at the fibrin interface is high, one can obtain similar lysis speed as for a high global concentration, *i.e.*, if the MNRs can be concentrated at the clot/solution interface, one can achieve a high lysis rate at a low global concentration. We have designed an experiment to demonstrate this effect. The *in-vitro* experiment at $C_{\mathrm{Rod}} = 1\,\mathrm{mg\,ml^{-1}}$ was repeated with all the other experimental conditions fixed except adding an iron nail at the right end of the PDMS device, close to the clot segments. Due to the higher magnetic permeability of the nail, there is a local field maximum of magnetic field attracts MNRs toward the clot interface and makes them stay at the clot/solution boundary during the experiment. Thus, the local concentration of rods

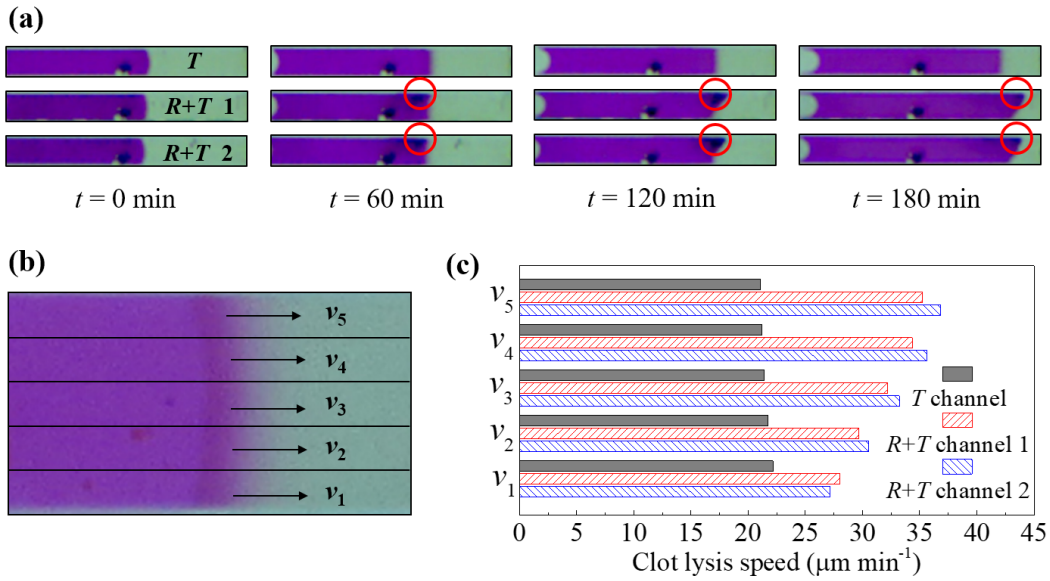

Figure 3.10: Locally enhanced thrombolysis through concentrating Nanorods: (a) Video clips of dye-solution/clot interface evolution in one "T" and two "R+T" channels with $C_{\text{Rod}} = 1\,\text{mg}\,\text{ml}^{-1}$ with a nail presented in the magnetic field. Red circles indicate locations of the concentrated MNRs. (b) Each channel is horizontally divided into 5 sub-channels of equal width, and the moving speed of liquid/clot interface in each sub-channel is labeled as v_1, v_2, v_3, v_4, and v_5, from bottom to top. (c) The local clot lysis rate of three channels. Due to the conjugation of MNR at the top right corner in two "R+T" channels, the lysis rate is increased from v_1 to v_5. The enhanced thrombolysis factor β can be up to 1.75 which is comparable to at $C_{\text{Rod}} = 5\,\text{mg}\,\text{ml}^{-1}$ shown in **Figure 3.8(d)**.

at the clot/solution interface is greatly increased.

As shown in **Figure 3.10(a)**, the rods are uniformly distributed in the "R+T" channels at $t = 0\,\text{min}$. When the magnetic field is on, the rods are concentrated at the clot boundaries and form a taper-shape. To evaluate the location-dependent thrombolysis rate, each channel in **Figure 3.10(a)** is horizontally divided into 5 sub-channels of equal width, as shown in **Figure 3.10(b)** of the "T" channel. The moving speeds of liquid/clot interface at different sub-channels, from bottom to top, are estimated as v_1, v_2, v_3, v_4, and v_5. According to the results shown in **Figure 3.10(c)**, the thrombolysis rates v_T in sub-channels of "T" are very uniform with an average value of $22.2 \pm 0.1\,\mu\text{m}\,\text{min}^{-1}$. Remarkably, the thrombolysis rates v_{R+T} in sub-channels of "R+T" increases from v_1 to v_5 due to the gradual accumulation of MNR

toward the up-right corner at the boundary. The maximum thrombolysis rate v_{R+T} at different location in "R+T" channels is up to $26.8 \pm 0.4\,\mu m\,min^{-1}$. Thus, the enhanced thrombolysis factor $\beta = \frac{v_{R+T}}{v_T}$ can be up to 1.66. However, for $C_{Rod} = 1\,mg\,ml^{-1}$ with uniform MNR distribution shown in **Figure 3.8(d)**, $v_{R+T} = 29 \pm 9\,\mu m\,min^{-1}$ while $v_T = 26 \pm 8\,\mu m\,min^{-1}$, and $\beta = 1.1$. Thus, for the same C_{Rod}, the thrombolysis enhancement by rods concentrated at the clot/solution interface is significantly larger than that when the rods are distributed uniformly and activated over the whole solution. In fact, as shown in **Figure 3.8(d)**, the β of local-concentrated rods with $C_{Rod} = 1\,mg\,ml^{-1}$ is comparable to that of $C_{Rod} = 5\,mg\,ml^{-1}$ with uniform MNR distribution. The results demonstrate that by concentrating MNRs at the clot/liquid interface, even with a low C_{Rod}, the v_{R+T} can be significantly improved. This feature would reduce the potential side-effects caused by MNRs for clinical application [125].

3.4.2 *In-vivo* experiment with rat model

The effect of rotating MNRs to improve tPA efficiency has been tested in animal experiments by our collaborators. As schematically shown in **Figure 3.11(a)**, the RMF was generated by a device consisted of two identical NdFeB magnets of rectangular shape (NdFeB, BY0X08DCS, K&J, Pipersville, PA), a homemade rotating frame and an AC motor (US560-001U2, Oriental Motor, Torrance, CA), of which the rotating speed could be continuously adjusted and digitally read from a indicator/controller (SDM496, Oriental Motor, Torrance, CA). The permanent magnets were symmetrically mounted on the frame with their poles attractively facing each other. The rotating frame was made of aluminum and the mounting position was adjustable. Thus, the magnetic field distribution between the two magnets could be continuously adjusted to a designated value of local magnetic field strength at the infected hindlimb of rat (red-dash circle on rat paint). **Figure 3.11(b)** also plots four representative field distributions induced by the magnets in different locations. From the results, one can see that the field strength is pretty uniform at the center of the magnet system and the value varies from 40 mT to 200 mT, which satisfies the *in-vitro* experimental conditions.

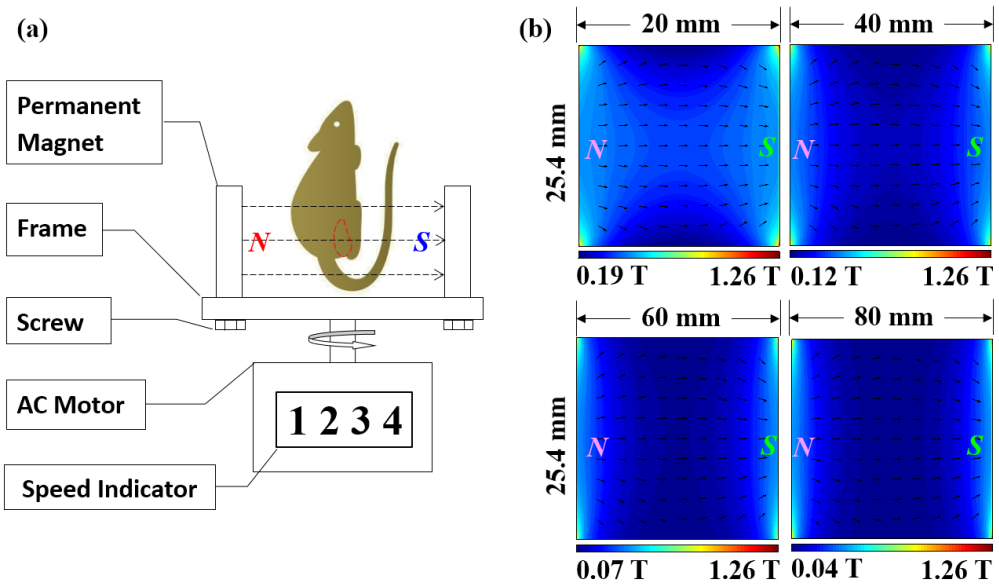

Figure 3.11: *In-vivo* experimental setup. (a) Schematic illustration of the apparatus. (b) Magnetic field distribution between two permanent magnets at different separations marked on the top of each image.

For thrombosis induction, the femoral vessels of C57/BL6 mice (20-25 g) were damaged via solution of ferric chloride ($FeCl_3$) to the outer surface. This resulted in the formation of a thrombus within the vessel, the severity of which is controlled by the concentration of the $FeCl_3$ solution. At 10 min after the induction, retro-orbital intravenous tPA ($10\,mg\,kg^{-1}$) and Nickel rods administration was started. Ni MNR suspension ($10\,mg\,ml^{-1}$) was previously prepared by sonicating in 1% polyacrylic acid solution and was injected into the mouse ($100\,mg\,kg^{-1}$) together with or without tPA. Then the infected hindlimb was put in the center of homemade rotating magnets (20 Hz) with magnetic field strength of 40 mT for 45 minutes, shown in **Figure 3.12(a)**. After 24 hours, the mouse was anesthetized to check the previously formed thrombi in femoral vessel. Mice were randomly divided by 3 groups. Group I ($n = 2$) was just treated intravenously with PBS as control, Group II ($n = 4$) was injected with tPA solution, Group III ($n = 3$) was treated by tPA combining with nickel rods. From the results shown in **Figure 3.12(b)**, the thrombus remained in all the mice of Group I while all the mice in Group II which receive tPA injection had a little residual of thrombus.

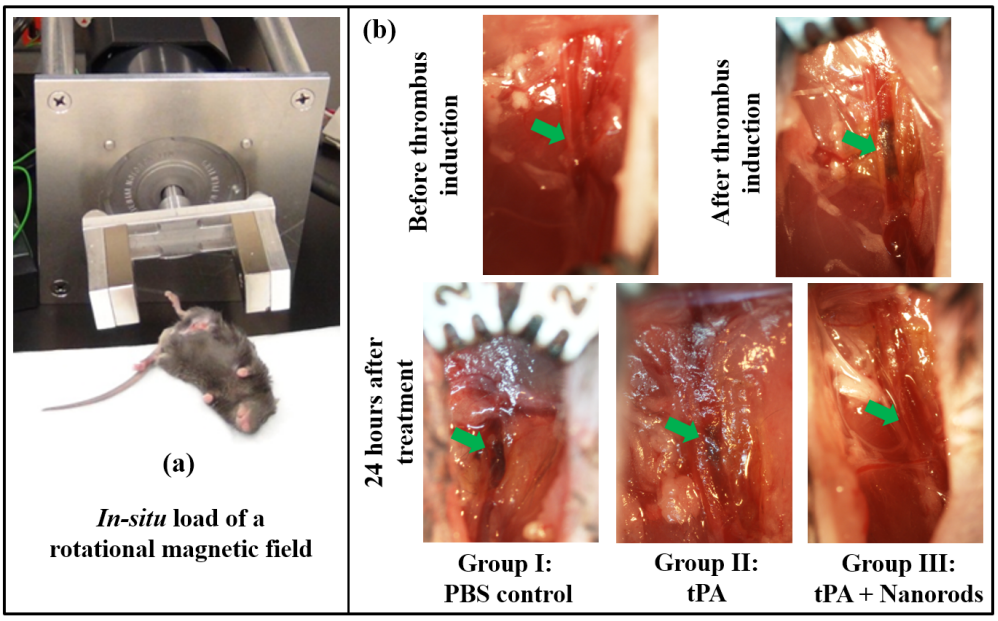

Figure 3.12: Enhanced thrombolysis by active MNRs is demonstrated in mice embolism model. (a) *In-situ* experimental setup; (b) Thrombolysis evaluation in the right femoral vessels of mice belonging to three groups associated with different administrations. The green arrows indicate the inducted region in the femoral vessels of C57/BL6 mice.

But in Group III, with both tPA and Ni MNRs injection and treated in RMF, there were no residual thrombus left. This preliminary result demonstrated higher thrombus removal efficiency of the active MNR method.

3.5 Conclusion

We have developed a novel active MNR-based method to directly enhance tPA mediated thrombolysis. Compared with nano-carrier based strategies that focus on the loading rate of specified drug molecules to specified nano-carriers, active motions of MNRs accelerate the thrombolysis by elevating drug transport through a hydrodynamic convection, which is controlled by many parameters such as MNR concentration, magnetic field, and rotation frequency. The results illustrate that MNRs can be used as an independent input to power the drug's efficacy and develop a safer and more effective medical treatment without immobilizing and encapsulating drug molecules. With further development, drug agitation by MNRs could

be an important step to treat clot in small blood vessel more specifically and safely, and can also be used as a general principle for other disease treatment.

Chapter 4

Targeted Delivery and Improving Stroke Treatment by Magnetic Nanorod Loaded with tPA

4.1 Introduction

As discussed in previous chapter, tPA remains the only proven treatment to improve clinical outcome of patients with acute ischemic stroke. Our previous results (**Chapter 3**) have documented that when Ni MNRs in combination of systematic administration of tPA could breakdown blood clot, which is enhanced when a RMF is applied [106]. However, hemorrhage, neurotoxicity, and short treatment time window comprise the major limitations for this thrombolytic therapy. To further reduce the risks associated with tPA treatment, we

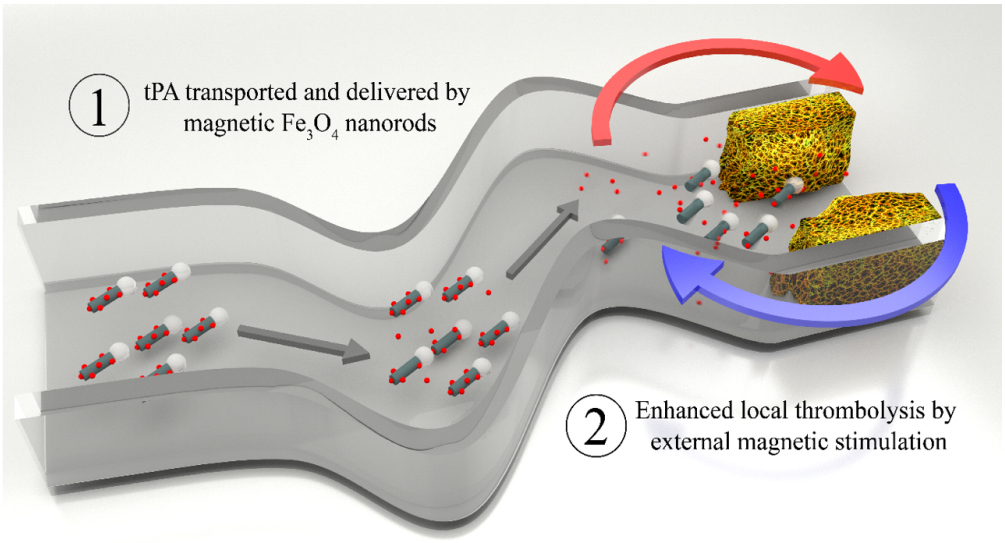

Figure 4.1: Schematic illustration of using biocompatible Fe_3O_4-MNRs conjugated tPA (MNR-tPA) to target blood clots under magnetic guidance. Blood clots can be mechanically pored and loosened by the Fe_3O_4-MNRs under a RMF, and lysed biochemically by tPA released from MNRs, which thus improve thrombolysis beyond the efficiency currently observed for tPA.

have designed iron oxide MNRs that are loaded with tPA through chemical covalent bond for thrombolysis. This method can significantly reduce the amount of tPA administrated in a stroke treatment and also improve tPA-mediated thrombolystic efficiency through targeted drug delivery. As shown in **Figure 4.1**, the proposed approach is using biocompatible Fe_3O_4 MNRs loaded with tPA to guide and deliver to the targeted blood clot site and then release the tPA locally. After the MNRs are delivered to the clot site, the local tPA release can be further increased when an external RMF is applied. The combination of increased tPA release and enhanced mass transport could greatly improve the thrombolytic efficiency, which are further demonstrated in this chapter by a systematic and quantitative study and *in-vitro* thrombolysis assay.

4.2 Experiment methods

4.2.1 Fabrication of Fe_3O_4 nanorods

Similar to the fabrication of Ni nanorods. The magnetic Fe_3O_4 nanorods were fabricated by the OAD. Compare to Ni, Fe_3O_4 is biocompatible and is the only FDA approved magnetic material that can be used in humans. A monolayer of 540 nm diameter SiO_2 beads on Si substrate. Then the bead-coated substrates were then loaded into a custom built electron beam evaporation deposition chamber. Fe_2O_3 was deposited onto the monolayers at a vapor incident angle of 86° and at a rate of $\sim 0.1\,\mu m\,s^{-1}$. The deposition was stopped when QCM reading reached 2 µm so Fe_2O_3 nanorods of length $\sim 1\,\mu m$ were obtained. The as-deposited samples were then annealed in ethanol/nitrogen environment at 350 °C for 1 hour in order to reduce Fe_2O_3 to Fe_3O_4.

A representative SEM image of the as-deposited Fe_2O_3 nanorods on silica bead monolayer is shown in **Figure 4.2(a)**. These tilted, aligned nanorod array has a tilting angle $\beta = 41^\circ$ with respect to surface normal and a length $l = 1.02 \pm 0.03\,\mu m$. The SEM image of an individual Fe_3O_4 nanorod (**Figure 4.2(b)**) reveals that the rod has a cylindrical shape with a diameter $d = 300\,nm$. The transmission electron microscopy (TEM) image of the

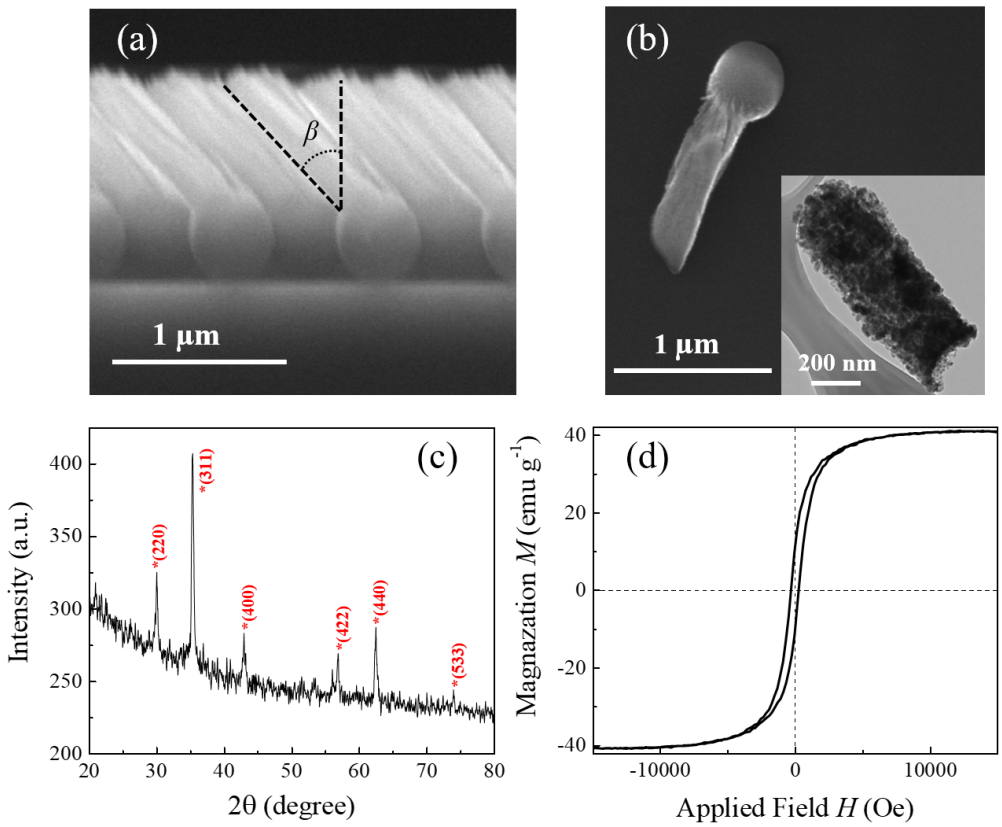

Figure 4.2: (a) A representative SEM image of as-deposited Fe_2O_3 nanorods. (b) A SEM image of an individual Fe_3O_4 nanorod obtained after annealing. Insert: a TEM image of a Fe_3O_4 nanorod. (c) The XRD pattern of Fe_3O_4 nanorods. (d) A magnetization curve of Fe_3O_4 nanorods.

Fe_3O_4 nanorod after removing the SiO_2 bead (insert in **Figure 4.2(b)**) exhibits a porous and granulated structure, made of Fe_3O_4 crystals with size $\sim 30\,\text{nm}$, which is consistent with the XRD data. As shown in **Figure 4.2(c)**, the annealed Fe_3O_4 nanorods have a preferred (311) orientation with a dominant sharp peak at $2\theta = 35.4°$. According to the Scherrer equation, the average crystal size is about 30.3 nm, consistent with the TEM measurement. The magnetic hysteresis loop (**Figure 4.2(d)**) shows that the nanorods' magnetic susceptibility χ is 2.10 and the saturation magnetization m_s is $41\,\text{emu}\,\text{g}^{-1}$, which is about half of the bulk Fe_3O_4 material ($92 - 100\,\text{emu}\,\text{g}^{-1}$) [126]. This is because the small crystal and porosity could reduce both the magnetic susceptibility and saturation magnetization of the nanorods [127].

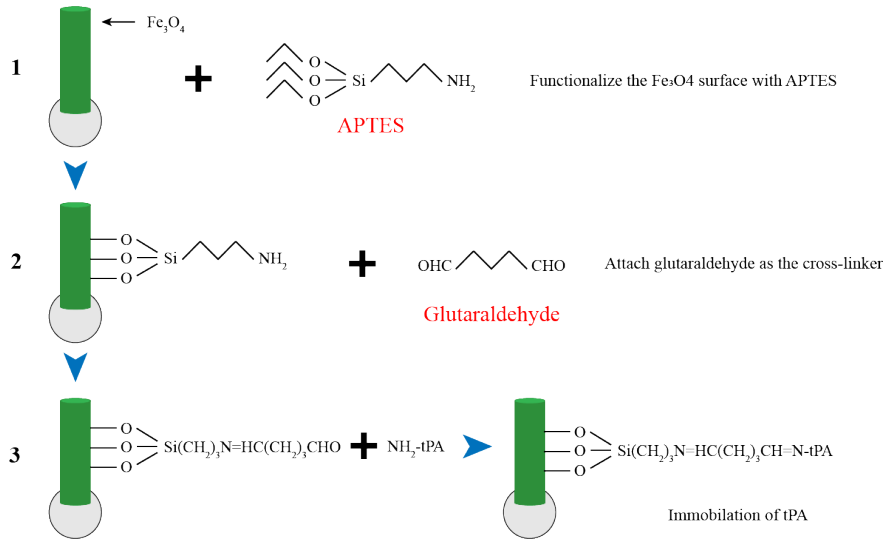

Figure 4.3: A schematic diagram showing the surface modification of Fe_3O_4 MNRs with APTES (step 1), activation with glutaraldehyde (step 2), and immobilization of tPA (step 3).

4.2.2 Immobilization of tPA on MNRs

As shown in **Figure 4.3**, experimentally, to load tPA, Fe_3O_4 MNRs were dispersed in ethanol/water mixture with the volume radio of 4:1. Then 3-aminopropyltriethoxysilane (APTES) and dimethylformamide were added into the solution until the final concentration of each was 5% by volume, respectively. The solution was shaken for 2 hours at room temperature in order to functionalize the Fe_3O_4 MNR surface with amine groups. The amine derived Fe_3O_4 MNRs were then separated from the solution with the help of a magnet and washed with phosphate buffered saline (PBS) solution for 3 times. After the washing, the MNRs were re-dispersed in PBS solution and mixed with 0.5% glutaraldehyde for 30 min with shaking at 30 °C, followed by washing 3 times with PBS. Finally, the glutaraldehyde modified MNRs were mixed with tPA solution at the concentration of 500 µm ml^{-1} for 12 hours at 4 °C to obtain tPA immobilized Fe_3O_4 MNRs. The amount of immobilized tPA was determined by measuring unbound tPA concentration in the supernatant before and after mixed with glutaraldehyde modified MNRs. The protein assay kit from Thermo Scientific (Rockford, IL)

was used in this experiment.

4.3 tPA release experiments

When MNRs are loaded with tPA, the loaded tPA may release from the MNRs due to a diffusion process. The release rate is related to tPA's local concentration and diffusivity thus can also be enhanced using a RMF. Mathematically, in a cylindrical coordinate, the tPA concentration C_{tPA} is a function of t and radius r, governed by the cylindrical form of Equation (1.22),

$$\frac{\partial C_{\mathrm{tPA}}}{\partial t} = D\left(\frac{\partial^2 C_{\mathrm{tPA}}}{\partial t^2} + \frac{2}{r}\frac{\partial C_{\mathrm{tPA}}}{\partial r}\right), \tag{4.1}$$

where D is the diffusion constant of tPA and the boundary conditions are,

$$\begin{aligned} \frac{\partial C_S}{\partial t} &= D\frac{\partial C_{\mathrm{tPA}}}{\partial r}, r = r_0, t > 0 \\ C_{\mathrm{S}} &= C_0, t = 0 \\ C_{\mathrm{tPA}} &= 0, t = 0 \end{aligned} \tag{4.2}$$

where C_S is the tPA concentration at the surface of MNR, C_0 is the initial tPA surface concentration and r_0 is the surface of MNR. When the solution is well stirred, C_{tPA} is only a function of time, and consider the mass conservation of the tPA, Equations (4.1) and (4.2) can be simplified as,

$$\frac{\partial C_{\mathrm{tPA}}}{\partial t} + k\left(\lambda + \eta_s C_{\mathrm{Rod}}\right) C_{\mathrm{tPA}} - \lambda\eta_s C_{\mathrm{Rod}} k C_0 = 0, \tag{4.3}$$

where k is the release constant of the tPA, λ is a function of the tPA's diffusivity D, and it is used to measure the chemical potential difference between C_S and C_{tPA}. λ can be affected by experiment conditions such as the temperature and the rotating speed of MNRs. η_s is the

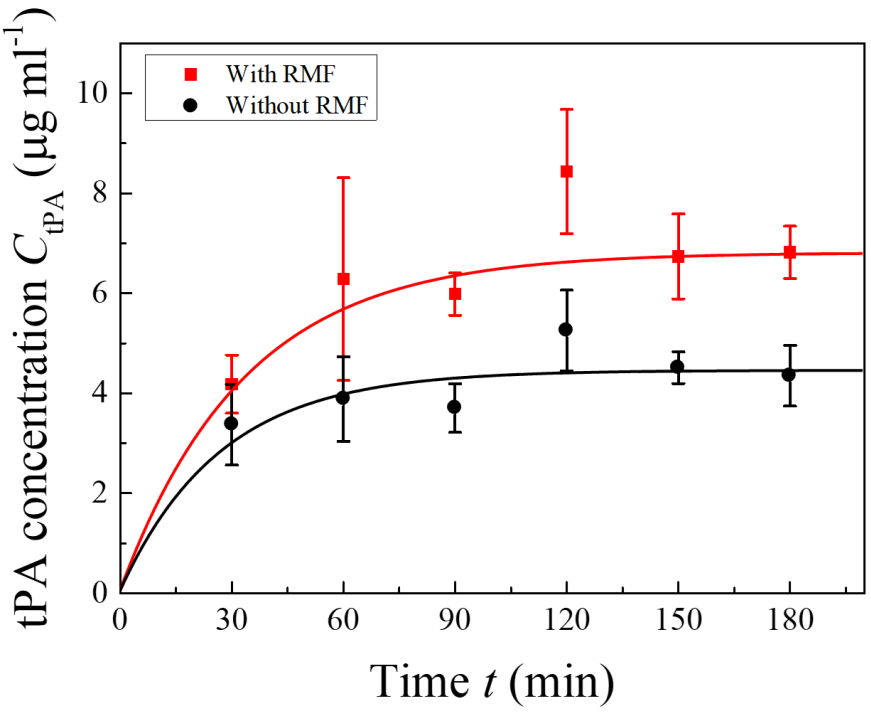

Figure 4.4: The plot of the accumulated tPA concentration C_{tPA} versus release time t. $C_{\mathrm{Rod}} = 1\,\mathrm{mg\,ml^{-1}}$ for all experiments. Each data point was an average from 3 repeated experiments.

surface area of an individual MNR. The tPA concentration in solution can be expressed as,

$$C_{\mathrm{tPA}} = \frac{\lambda \eta_s C_{\mathrm{Rod}}}{\lambda + \eta_s C_{\mathrm{Rod}} C_0 \left(1 - e^{-t/t_0}\right)}, \tag{4.4}$$

where the tPA release time constant $t_0 = \left[k\left(\lambda + \eta_s C_{\mathrm{Rod}}\right)\right]^{-1}$.

Experimentally, the tPA releasing process was determined with and without a 20 Hz external magnetic field of $B \sim 3$ mT in room temperature ($T = 20\,^{\circ}\mathrm{C}$). The tPA-loaded MNRs were dispersed in normal saline solution (NS) and the MNR concentration C_{Rod} was fixed at $1\,\mathrm{mg\,ml^{-1}}$. **Figure 4.4** shows the experimental determined tPA concentration C_{tPA} in NS solution as a function of release time t for both cases. The solid lines are fitting curves using Equation (4.4). During the first 2 hours, the accumulated tPA concentration C_{tPA} in bulk solution increased gradually, then became saturated. The saturated tPA concentration,

$C^s_{\text{tPA}} = 6.8 \pm 0.4\,\mu\text{g}\,\text{ml}^{-1}$ and $4.4 \pm 0.2\,\mu\text{g}\,\text{ml}^{-1}$ were different from the case with and without the RMF. Two conclusions can be drawn from **Figure 4.4**. First, with the RMF, the C^s_{tPA} is about 50% higher than the that without the RMF, which suggests that RMF can be used to stimulate and accelerate the tPA release, and be used as a mechanism to enhance tPA-mediated thrombolysis. Second, tPA molecules are immobilized onto MNR's surface through not only covalent bonds but also physical absorption. Since the tPA-APTES conjugates are considered physically stable and would release tPA only when the linker molecule is cleaved, the physically absorbed drug is released from the surface due to desorption and diffusion. Compared to the tPA mass loading ratio of 6% on MNRs, the releasing ratio (mass of released tPA over mass of loaded tPA) is about 11.3% and 7.3% for the MNRs with and without the RMF, respectively.

The experimental results agree with the simple tPA release model (Equation (4.4)), and the solid curves in **Figure 4.4** show the fitting results for both cases using Equation (4.4). This property of dynamic release of tPA is important in clinical setting. Efficient thrombolysis requires timely systemic administration of high-dose tPA. However, high C_{tPA} in circulatory system may leads to fatal hemorrhagic complications or other serious neurological deficit even when patient is survival [11, 128–131]. It takes about 1 min to circulate the total amount of blood in the normal situation. If during a few circulations, the tPA-loaded MNRs can be captured at the clot site, then only a small amount of tPA will be released during the transportation process. Without the RMF, the tPA release time constant $t_0^0 = 34 \pm 8\,\text{min}$, while with the magnetic field, $t_0^B = 30 \pm 10\,\text{min}$, suggesting that the release process was slightly faster. In both cases, t_0 is about 30 min. Thus, the tPA-loaded MNRs could help effectively prevent incising the circulating tPA concentration in blood steam and reducing the risk of hemorrhage. In addition, tPA can covalently bind to MNRs and retains the enzyme activity. The tPA-bound MNRs can target to the ischemic site *in-vivo* under the guidance of an external magnet; therefore, bound tPA can subsequently be efficiently delivered at the

site of embolism at a high concentration to facilitate thrombolysis, so that lower doses of tPA can be applied in ischemic stroke. Meanwhile, the concentration of tPA is significantly reduced in the circulation of the non-targeted regions. Furthermore, since tPA is released faster and more from MNRs when a RMF is applied, the tPA release dosage can purposely be manipulated. The desirable tPA concentration for effective clot lysis is achieved by increasing administrated MNR concentration and applying the RMF once most of the MNRs have reached the clot site.

4.4 Thrombolysis experiment with tPA loaded Fe_3O_4 MNRs

4.4.1 *In-vitro* experiment with PDMS channels

To demonstrate that tPA-loaded Fe_3O_4 MNRs could indeed enhance thrombolytic efficiency, we performed quantitatively experiments in the 8-channel PDMS plate with artificial blood clot as described in **Section 3.2.3**. When the other parameters were fixed, the tPA-loaded MNR concentration C_{rod} was systematically changed from 1 to 6 mg ml^{-1}, indicating that the maximum concentration of tPA released in the solution was around 6 to 36 µg ml^{-1}. The MNRs were dispersed in dye solution without any additional tPA. The control experiment was performed with a tPA only solution at $C_{\text{tPA}} = 20\,\mu\text{g}\,\text{ml}^{-1}$. At such a tPA concentration, the clot lysis process is a diffusion limited reaction as shown in **Figure 3.7**. **Figure 4.5** shows the clot lysis speed v_T as a function of C_{rod} with and without the RMF. Without a RMF and when $C_{\text{rod}} < 2\,\text{mg}\,\text{ml}^{-1}$, the tPA-mediated thrombolytic speed v_T is slower than that of the pure tPA reference group since the tPA release ratio is small (7.3%). When C_{rod} increased to 3 - 5 mg ml^{-1}, the tPA-loaded MNRs could lyse clot with a speed comparable to that of $C_{\text{tPA}} = 20\,\mu\text{g}\,\text{ml}^{-1}$ tPA solution.

According to Equation (4.4), the averaged clot lysis speed v_T^0 without a RMF can be expressed as,

$$v_T^0 = \alpha C_{\text{tPA}} = \alpha \frac{\lambda \eta_s C_{\text{rod}} C_0}{\lambda + \eta_s C_{\text{rod}}} \left(1 - e^{-t/t_0}\right) . \tag{4.5}$$

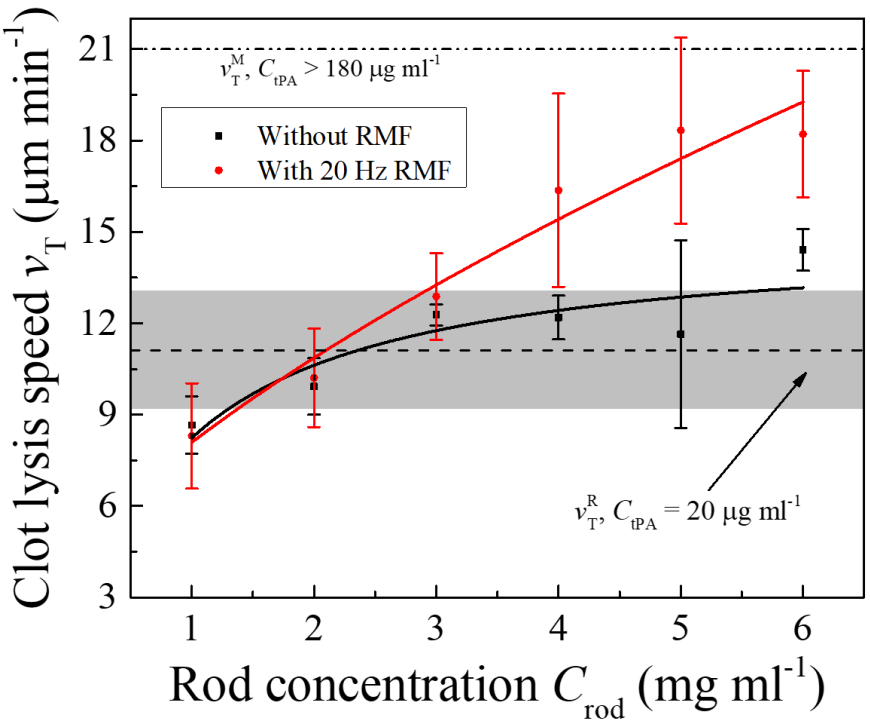

Figure 4.5: The plot of clot lysis speed v_T versus the MNR concentration $C_textrod$ with and without a RMF (20 Hz, 3 mT). The dashed line represents the reference tPA speed v_T^R at $C_{\mathrm{tPA}} = 20\,\mu\mathrm{g\,ml^{-1}}$ and the shadow area represents the standard derivation, and the dash-dotted line represents the maxima saturated tPA speed v_T^M at $C_{\mathrm{tPA}} = 180\,\mu\mathrm{g\,ml^{-1}}$. Each data point was an average from 3 repeated experiments.

When $t \gg t_0$, C_{tPA} reaches a maximum saturation concentration, and the clot lysis speed becomes time independent, but is a function of C_{rod},

$$v_T^0 = \alpha \frac{\lambda \eta_s C_{\mathrm{rod}} C_0}{\lambda + \eta_s C_{\mathrm{rod}}}\,. \tag{4.6}$$

Such an expression fits the experiment data well, as shown by the black solid curve in **Figure 4.5**. When a RMF is applied, the average lysis speed v_T^B is larger than v_T^0 at the same C_{rod}. Especially when $C_{\mathrm{rod}} = 5 \sim 6\,\mathrm{mg\,ml^{-1}}$, $v_T^B \approx 18\,\mu\mathrm{m\,min^{-1}}$, which is equivalent to the lysis speed v_T of a pure tPA solution with $C_{\mathrm{tPA}} = 100\,\mu\mathrm{g\,ml^{-1}}$. Based on our tPA releasing experiment, the maxima released concentration for $C_{\mathrm{rod}} = 5 \sim 6\,\mathrm{mg\,ml^{-1}}$ is around $C_{\mathrm{tPA}} = 36\,\mu\mathrm{g\,ml^{-1}}$, which corresponds to $v_T^0 = 13\,\mu\mathrm{m\,min^{-1}}$, as compared to $v_T^B = 18\,\mu\mathrm{m\,min^{-1}}$.

Clearly, with the acceleration of magnetic field, the clot lysis speed can be boosted by about 40%, with less than 12% of total loaded tPA released. The underlying mechanism for such an enhanced thrombolysis might be complicated, with the following possible reasons. First, tPA that covalently bonded to MNRs, retains its enzymatic activity, and thrombolysis is enhanced when tPA-loaded MNRs can be delivered into the clot. To demonstrate this, tPA loaded MNRs were first dispersed in water at $C_{\text{rod}} = 1\,\text{mg}\,\text{ml}^{-1}$ to release physisorbed tPAs (non-bonded tPAs). And the water was replaced every 24 hours. After 48 hours, both MNRs and supernatant were collected separately with the help of a magnet. The clot lysis speed of the supernatant was measured to be about $4.2\,\mu\text{m}\,\text{min}^{-1}$, which was much lower than that of the reference $20\,\mu\text{m}\,\text{ml}^{-1}$ tPA solution ($v_T^R \approx 11\,\mu\text{m}\,\text{min}^{-1}$ in **Figure 4.5** gray area), suggesting that most of the physically adsorbed tPAs have been released. Meanwhile, under 20 Hz magnetic field, the MNRs collected by magnet after multiple washing could achieve $\sim 80\%$ average lysis speed compared to that of fresh tPA-loaded MNRs, demonstrating that covalently bonded tPA on MNRs can still lysis the clot. Second, the rotating MNRs could mechanically disrupt the fibrin network of clot. Third, at high C_{rod}, the collisions among MNRs during rotating could further increase tPA release. Finally, such an enhancement in v_T could be due to the enhanced mass transport effect because of the rotating MNRs. According to Equation (3.14) [106], the rotating rods give,

$$v_T^B = \alpha C_{\text{tPA}} + A C_{\text{tPA}} C_{\text{rod}}^{2/3}\,, \tag{4.7}$$

where A is a parameter related to the enhancement of thrombolysis. Considering both the tPA releasing effect (Equation (4.4)) and the enhanced mass transport,

$$v_T^B = \frac{k_1 C_{\text{rod}}^{2/3} + k_2 C_{\text{rod}}^{5/3}}{k_3 + C_{\text{rod}}}\,, \tag{4.8}$$

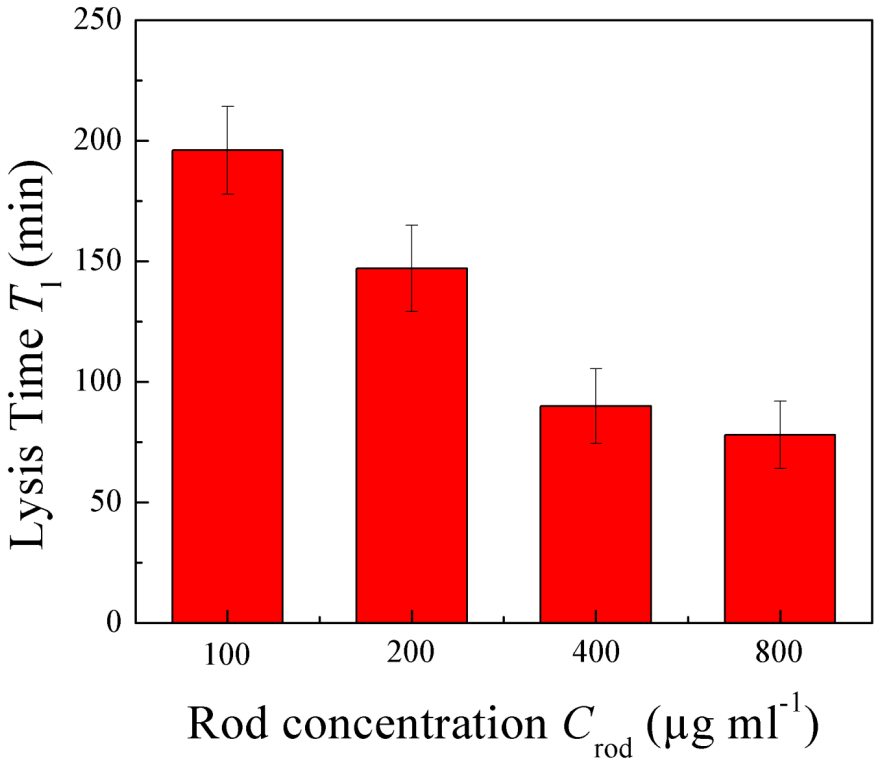

Figure 4.6: The plot of clot lysis time T_l versus the tPA loaded MNR concentration C_{rod} using PE50 catheter based blood clot model under a RMF (20 Hz, 40 mT).

where $k_1 = a\lambda$, $k_2 = A\lambda$ and $k_3 = \dfrac{\lambda}{\eta_s}$ are fitting constants and the red solid fitting curve is shown in **Figure 4.5** which gives relatively good fitting.

4.4.2 *In-vitro* experiment with small catheters

The enhanced lysis effect of tPA loaded MNRs has been further validated by in vitro thrombolysis assay. PE 50 catheters (with an approximate diameter of 0.58 mm) containing a rat blood clot (length $\sim$ 5 mm) were used as the vascular thrombosis model to mimic *in-vivo* thrombotic condition. Four different nanorod concentrations, $C_{\text{rod}} = 100\,\mu\text{m ml}^{-1}$, $200\,\mu\text{m ml}^{-1}$, $400\,\mu\text{m ml}^{-1}$ and $800\,\mu\text{m ml}^{-1}$ were used to determine the optimal C_{rod} for thrombolytic efficiency with a RMF (20 Hz, 40 mT) at room temperature.

As shown in **Figure 4.6**, the lysis time T_l, which is defined as the time duration to totally lyse the 5-mm long blood clot in PE 50 catheter, was decreased with C_{rod}. As expected,

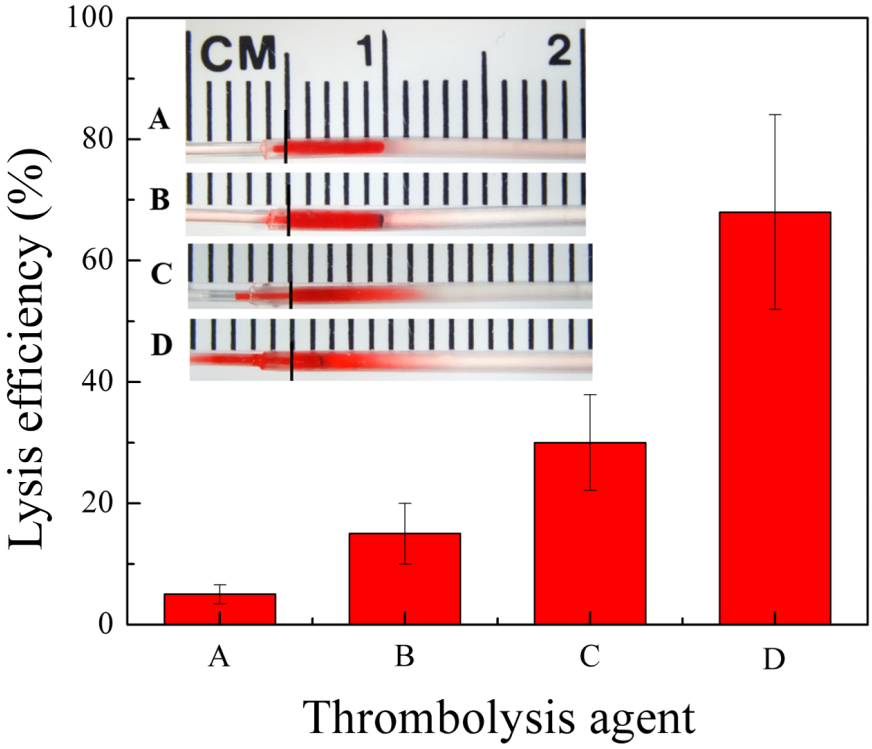

Figure 4.7: The plot of lysis efficiency in the PE 50 catheter-based blood clot model under different thrombolytic condition for 60 min under a RMF (20 Hz, 40 mT): A - normal saline, B - 400 µg ml^{-1} MNRs in normal saline, C - 40 µg ml^{-1} tPA solution, and D - 400 µg ml^{-1} tPA loaded MNRs in normal saline. The insert shows a photo after 60 min in the PE50 catheter-based blood clot model.

$C_{\text{rod}} = 400\,\mu\text{g ml}^{-1}$ has a significantly shorter T_l compared to that of $C_{\text{rod}} = 200\,\mu\text{g ml}^{-1}$. Interestingly, there is no significant difference in T_l for $C_{\text{rod}} = 400\,\mu\text{g ml}^{-1}$ and $800\,\mu\text{g ml}^{-1}$, suggesting that $C_{\text{rod}} = 400\,\mu\text{g ml}^{-1}$ is an optimal tPA-MNR concentration for blood clot lysis, and at $C_{\text{rod}} = 400\,\mu\text{g ml}^{-1}$ the maximum clot lysis speed is achieved, the thrombolysis kinetics changes from diffusion limited to reaction limited. The ferromagnetic behavior of Fe_3O_4 MNRs used in this study may be aggregated, and consequently block capillaries as discussed in Ref. [106]. The size of the clusters is positively related to the size of MNR and its magnetization.

Figure 4.7 demonstrates the lysis efficiency, which is defined as the ratio of blood clot mass before and after thrombolysis for a fixed time duration $T = 60\,\text{min}$ by different lysis

assays: normal saline, 400 µg ml^{-1} MNRs (without tPA) in normal saline, 40 µg ml^{-1} tPA solution or 400 µg ml^{-1} tPA-loaded MNRs in normal saline (equivalent to 24 µg ml^{-1} tPA). We found that the rotating tPA-loaded MNRs achieved 70% of lysis efficiency, which is more efficient than that (30%) of tPA solution. In agreement with another study [132], rotating tPA-loaded MNRs could significantly increase thrombolytic efficiency. Notably, even without tPA loading, the rotating MNRs in NS can also achieve a lysis efficiency of 15%, suggesting that the mechanical rotation of MNRs could lyse clot mechanically. Previous studies have elucidated that the tPA penetration depth and lysis zone is restricted to the top layer of the thrombus due to the presence of a tight fibrin meshwork [21, 133, 134], yet the mechanical rotation of MNRs could effectively increase the tPA penetration depth and improve clot lysis efficiency.

4.5 Conclusion

Successful thrombolysis depends on the joint effects of conversion of activated plasminogen to plasmin (the major enzyme responsible for clot breakdown) and effective exposure of both the substrate and the plasminogen activator to the entire blood clot. The delivery of tPA into the center of a blood clot is either dependent merely on passive diffusion or the pressure facilitated (bulk) flow, as the rate of lysis is increased up to 100-times when plasminogen activator and plasminogen are introduced into cylindrical clots by pressure-induced bulk flow in comparison with diffusion alone. However, pressure-induced bulk flow is often weakened by inadequate collateral circulation or systemic hemodynamic compromise. In addition, progression of tPA-mediated clot lysis in the blood vessel proceeds gradually and stepwise, allowing the thrombolytic zone to only move slowly, layer-by-layer through the clot, progressively restricting the amounts of tPA available and, thus, reducing lysis efficiency at deeper thrombus sections. This study extends our previous work: we developed a novel, magnetically guided Fe_3O_4-MNRs loaded with tPA instead of Nickel MNRs for enhance thrombolytic efficiency. Since the MNRs can target the clot by a magnetic guidance and be spanned under a RMF,

the mechanical rotation of the MNRs as well as the enhanced mass transport in the fluid can help more tPA be delivered into the clot, which allow plasminogen to reach the new binding sites and enhances the susceptibility of clots to lysis. As a result, usage of the total dose of tPA is lower, tPA-mediated hemorrhagic complications is thus dramatically reduced, and the time window for tPA treatment could be longer. We note there are some limitation of this study, including, efficiency of tPA release and magnetic clustering, which may limit the clinical application. For example, large size of MNRs may not pass the capillary and cause server side effect in clinic setting. While, smaller MNRs would lead to large surface area/volume ratio thus can load more drug and greatly reduce the cluster size. On the other hand, some thrombotic disorders including stroke and cardiovascular ischemia, in which large blood vessels are occluded, are fatal diseases. These side effect may be ignored if the patients can be rescued using tPA-MNRs. Of course, it will be critical to optimize the size of MNRs and tPA release condition from MNRs. This study provides a proof of concept for developing a novel, magnetically guided MNRs to enhance thrombolysis. Since the tPA-MNRs can target the clot in the brain by a magnetic guidance and be spanned under a RMF, the clot can be pored with mechanical force and tPA can be delivered into the clot, which allow plasminogen to reach the new binding sites and enhances the susceptibility of clots to lysis. As a result, usage of the total dose of tPA will be lower, and tPA-mediated hemorrhagic complications will thus dramatically be reduced. If successful, this approach could revolutionize not only just for the treatment of ischemic stroke but also have major impact on other deadly thrombotic diseases such as myocardial infarction and pulmonary embolism.

Chapter 5

Conclusions and Future Work

Traditional stroke treatment therapies require mechanically remove blood clot by medical surgery or directly infuse tPA drug through a catheter placed within the blocked vessel. The challenges and disadvantages of the traditional stroke treatment methods are obvious: (1) Small and fragile brain blood vessels which normally characterized in sub-millimeter ($100 \sim 1000\,\mu m$) make surgery method impossible. (2) Free diffusion of tPA can cause SIH thus need the tPA to be administrated within the first 3 hours of stroke. Otherwise, the probability of SIH induced death will increase. (3) The treatment needs specific tools and experienced doctors which only available in the large hospitals.

In order to improve the traditional stroke treatment therapy, we attempted to develop simple but effective technique to help the treatment using magnetic nanomotors. In particular, we first introduced a method to manipulate magnetic particles and clusters in liquid environment near a substrate surface using a nuAMF. Unlike a permanent magnet pulling a magnetic particle, under such nuAMF, the particle moves away from the magnetic source with a periodic fluctuation in its trajectory that varies with a frequency that is twice that of the field frequency. The moving speed can be tuned by varying the magnetic field strength and gradient, its alternating frequency, and the particle size. A hydrodynamic model is developed that can qualitatively explain all of the phenomena we have observed. The manipulation of magnetic particles is the fundamental technique of more advanced applications, such as targeted drug delivery. Major part of the dissertation is dedicated to study how to improve tPA drug's effectiveness while reduce the amount of tPA used in a stroke treatment as same time. First, we investigated the acceleration of tPA mediated thrombolysis with magnetic Ni

nanorods. *In-vitro* experiments showed that Ni nanorods moved by a rotating magnetic field could accelerate the thrombolysis rate of low concentration tPA up to two-fold. A theoretical hydrodynamic model revealed the fundamental physical processes was developed to qualitatively explain the experimental results. To further reduce the risks of tPA treatment, Fe_3O_4 nanorods were fabricated and chemically loaded with tPA. This method could significantly reduce the amount of tPA administrated in a stroke treatment. We managed to load 6% (mass percentage) tPA onto Fe_3O_4 nanorods and the loaded tPA could be released within several hours. An external rotating magnetic field could significantly accelerate the release. The validity and efficiency of these enhanced stroke treatment methods had also been demonstrated *in-vivo* by our medical school collaborators. All these works lay a solid foundation for using magnetic nanomotors to effectively treat stroke.

The future research should be focusing on how to further improve the safety of the MNR method. For example, during the past experiments, we have observed that the MNRs will naturally aggregate together to form large clusters. The size of NMRs is very important because large MNRs may not only be unable to reach target area through small blood vessels, but also may directly block the blood flow. Thus, the research on MNR surface modification or the fabrication technique for superparamagnetic NRs to prevent aggregation are needed. Beside the aggregation problem, we have also observed that the MNRs will stick on the PDMS walls and blood vessels. How to prevent such sticking is another major challenge. On clinical side of view, one big problem demanding to solve is after the treatment is finished, how to safely collect and remove all the MNRs from the circulatory system? These are only parts of the challenges that future researchers have to face. The study of nanotechnology based stroke treatment is promising for future clinical applications.

References

[1] W. H. Organization et al., *Global status report on noncommunicable diseases 2010*, Geneva: World Health Organization, **2011**.

[2] B. Furie, B. C. Furie, "Mechanisms of thrombus formation", *New England Journal of Medicine* **2008**, *359*, 938–949.

[3] http://www.stroke.org/understand-stroke/what-stroke.

[4] H. Jørgensen, H. Nakayama, H. Raaschou, T. S. Olsen, "Stroke. Neurologic and functional recovery the Copenhagen Stroke Study.", *Physical medicine and rehabilitation clinics of North America* **1999**, *10*, 887–906.

[5] A. Ogawa, E. Mori, K. Minematsu, W. Taki, A. Takahashi, S. Nemoto, S. Miyamoto, M. Sasaki, T. Inoue, et al., "Randomized trial of intraarterial infusion of urokinase within 6 hours of middle cerebral artery stroke", *Stroke* **2007**, *38*, 2633–2639.

[6] http://uncovercalifornia.com/content/22711-intra-arterial-procedure-can-remove-stroke-causing-blood-clot-study.

[7] A. Laverdure, J. Surbeck, M. North, J. Tritto, "Growth, development, reproduction, physiological and behavioural studies on living organisms, human adults and children exposed to radiation from video displays", *Indoor and Built Environment* **2001**, *10*, 306–309.

[8] A. V. Alexandrov, C. A. Molina, J. C. Grotta, Z. Garami, S. R. Ford, J. Alvarez-Sabin, J. Montaner, M. Saqqur, A. M. Demchuk, L. A. Moyé, et al., "Ultrasound-enhanced systemic thrombolysis for acute ischemic stroke", *New England Journal of Medicine* **2004**, *351*, 2170–2178.

[9] J. Mohr, "Thrombolytic therapy for ischemic stroke: from clinical trials to clinical practice", *Jama* **2000**, *283*, 1189–1191.

[10] T. Brott, J. Bogousslavsky, "Treatment of acute ischemic stroke", *New England Journal of Medicine* **2000**, *343*, 710–722.

[11] H. P. Adams, G. Del Zoppo, M. J. Alberts, D. L. Bhatt, L. Brass, A. Furlan, R. L. Grubb, R. T. Higashida, E. C. Jauch, C. Kidwell, et al., "Guidelines for the early management of adults with ischemic stroke", *Circulation* **2007**, *115*, e478–e534.

[12] W. M. Clark, S. Wissman, G. W. Albers, J. H. Jhamandas, K. P. Madden, S. Hamilton, A. S. Investigators, et al., "Recombinant tissue-type plasminogen activator (alteplase) for ischemic stroke 3 to 5 hours after symptom onset: the ATLANTIS study: a randomized controlled trial", *Jama* **1999**, *282*, 2019–2026.

[13] G. J. Del Zoppo, J. L. Saver, E. C. Jauch, H. P. Adams, et al., "Expansion of the time window for treatment of acute ischemic stroke with intravenous tissue plasminogen activator", *Stroke* **2009**, *40*, 2945–2948.

[14] J. Feldschuh, Y. Enson, "Prediction of the normal blood volume. Relation of blood volume to body habitus.", *Circulation* **1977**, *56*, 605–612.

[15] P. Tanswell, E. Seifried, E. Stang, J. Krause, "Pharmacokinetics and hepatic catabolism of tissue-type plasminogen activator.", *Arzneimittel-Forschung* **1991**, *41*, 1310–1319.

[16] E. Seifried, P. Tanswell, D. Ellbrück, W. Haerer, A. Schmidt, "Pharmacokinetics and haemostatic status during consecutive infusions of recombinant tissue-type plasminogen activator in patients with acute myocardial infarction.", *Thrombosis and haemostasis* **1989**, *61*, 497–501.

[17] S. D. Kumbasar, E. Semiz, C. Ermis, S. Yalçinkaya, N. Deger, G. Pamir, D. Oral, "Effect of intraaortic balloon counter-pulsation on QT dispersion in acute anterior myocardial infarction", *International journal of cardiology* **1998**, *65*, 169–172.

[18] J.-H. Wu, K. Siddiqui, S. L. Diamond, "Transport phenomena and clot dissolving therapy: an experimental investigation of diffusion-controlled and permeation-enhanced fibrinolysis.", *Thrombosis and haemostasis* **1994**, *72*, 105–112.

[19] R. M. Prewitt, S. Gu, P. J. Garber, J. Ducas, "Marked systemic hypotension depresses coronary thrombolysis induced by intracoronary administration of recombinant tissue-type plasminogen activator", *Journal of the American College of Cardiology* **1992**, *20*, 1626–1633.

[20] P. J. Garber, A. L. Mathieson, J. Ducas, J. N. Patton, J. S. Geddes, R. M. Prewitt, "Thrombolytic therapy in cardiogenic shock: Effect of increased aortic pressure and rapid tPA administration: Can J Cardiol 1995; 11/1: 30–36", *Resuscitation* **1995**, *30*, 184.

[21] S. L. Diamond, S. Anand, "Inner clot diffusion and permeation during fibrinolysis", *Biophysical journal* **1993**, *65*, 2622–2643.

[22] S. Anand, J.-H. Wu, S. L. Diamond, "Enzyme-mediated proteolysis of fibrous biopolymers: Dissolution front movement in fibrin or collagen under conditions of diffusive or convective transport", *Biotechnology and bioengineering* **1995**, *48*, 89–107.

[23] X. Hua, L. Zhou, P. Liu, Y. He, K. Tan, Q. Chen, Y. Gao, Y. Gao, "In vivo thrombolysis with targeted microbubbles loading tissue plasminogen activator in a rabbit femoral artery thrombus model", *Journal of thrombosis and thrombolysis* **2014**, *38*, 57–64.

[24] B. Petit, F. Yan, F. Tranquart, E. Allemann, "Microbubbles and ultrasound-mediated thrombolysis: a review of recent in vitro studies", *Journal of Drug Delivery Science and Technology* **2012**, *22*, 381–392.

[25] N. Korin, M. Kanapathipillai, B. D. Matthews, M. Crescente, A. Brill, T. Mammoto, K. Ghosh, S. Jurek, S. A. Bencherif, D. Bhatta, et al., "Shear-activated nanotherapeutics for drug targeting to obstructed blood vessels", *Science* **2012**, *337*, 738–742.

[26] J. Myerson, L. He, G. Lanza, D. Tollefsen, S. Wickline, "Thrombin-inhibiting perfluorocarbon nanoparticles provide a novel strategy for the treatment and magnetic resonance imaging of acute thrombosis", *Journal of Thrombosis and Haemostasis* **2011**, *9*, 1292–1300.

[27] A. Abdalla, K. Mäder, "ESR studies on the influence of physiological dissolution and digestion media on the lipid phase characteristics of SEDDS and SEDDS pellets", *International journal of pharmaceutics* **2009**, *367*, 29–36.

[28] A. Rosengart, M. Kaminski, A. Ghebremeskel, L. Johns, K. Kaza, R. Novakovic, C. Wardrip, J. Frank, R. Macdonald in Stroke, *Vol. 35*, **2004**, pp. 299–299.

[29] E. Voros, M. Cho, M. Ramirez, A. L. Palange, E. De Rosa, J. Key, Z. Garami, A. B. Lumsden, P. Decuzzi, "TPA immobilization on iron oxide nanocubes and localized magnetic hyperthermia accelerate blood clot lysis", *Advanced Functional Materials* **2015**, *25*, 1709–1718.

[30] J.-P. Chen, P.-C. Yang, Y.-H. Ma, S.-J. Tu, Y.-J. Lu, "Targeted delivery of tissue plasminogen activator by binding to silica-coated magnetic nanoparticle", *International journal of nanomedicine* **2012**, *7*, 5137.

[31] Y. Xie, M. D. Kaminski, M. D. Torno, M. R. Finck, X. Liu, A. J. Rosengart, "Physicochemical characteristics of magnetic microspheres containing tissue plasminogen activator", *Journal of Magnetism and Magnetic Materials* **2007**, *311*, 376–378.

[32] H. Kempe, M. Kempe, "The use of magnetite nanoparticles for implant-assisted magnetic drug targeting in thrombolytic therapy", *Biomaterials* **2010**, *31*, 9499–9510.

[33] M. D. Kaminski, Y. Xie, C. J. Mertz, M. R. Finck, H. Chen, A. J. Rosengart, "Encapsulation and release of plasminogen activator from biodegradable magnetic microcarriers", *european journal of pharmaceutical sciences* **2008**, *35*, 96–103.

[34] https://www.nde-ed.org/EducationResources/CommunityCollege/MagParticle/Physics/HysteresisLoop.htm.

[35] S. S. Shevkoplyas, A. C. Siegel, R. M. Westervelt, M. G. Prentiss, G. M. Whitesides, "The force acting on a superparamagnetic bead due to an applied magnetic field", *Lab on a Chip* **2007**, *7*, 1294–1302.

[36] R. Rosensweig, *Ferrohydrodynamics*, Cambridge University Press, **1985**.

[37] M. Zborowski, J. J. Chalmers, "Magnetophoresis: fundamentals and applications", *Wiley Encyclopedia of Electrical and Electronics Engineering* **2015**.

[38] M. P. Hughes, H. Morgan, "Dielectrophoretic trapping of single sub-micrometre scale bioparticles", *Journal of Physics D: Applied Physics* **1998**, *31*, 2205.

[39] N. G. Green, H. Morgan, "Dielectrophoretic investigations of sub-micrometre latex spheres", *Journal of Physics D: Applied Physics* **1997**, *30*, 2626.

[40] M. Talary, J. Burt, J. Tame, R. Pethig, "Electromanipulation and separation of cells using travelling electric fields", *Journal of Physics D: Applied Physics* **1996**, *29*, 2198.

[41] F. Scherer, M. Anton, U. Schillinger, J. Henke, C. Bergemann, A. Krüger, B. Gänsbacher, C. Plank, "Magnetofection: enhancing and targeting gene delivery by magnetic force in vitro and in vivo", *Gene therapy* **2002**, *9*, 102.

[42] A. S. Lübbe, C. Alexiou, C. Bergemann, "Clinical applications of magnetic drug targeting", *Journal of surgical research* **2001**, *95*, 200–206.

[43] J.-M. Nam, C. S. Thaxton, C. A. Mirkin, "Nanoparticle-based bio-bar codes for the ultrasensitive detection of proteins", *science* **2003**, *301*, 1884–1886.

[44] P. Vavassori, M. Gobbi, M. Donolato, M. Cantoni, R. Bertacco, V. Metlushko, B. Ilic, "Magnetic nanostructures for the manipulation of individual nanoscale particles in liquid environments", *Journal of Applied Physics* **2010**, *107*, 09B301.

[45] X. Zhu, P. Grütter, "Imaging, manipulation, and spectroscopic measurements of nanomagnets by magnetic force microscopy", *MRS bulletin* **2004**, *29*, 457–462.

[46] E. Mirowski, J. Moreland, A. Zhang, S. E. Russek, M. J. Donahue, "Manipulation and sorting of magnetic particles by a magnetic force microscope on a microfluidic magnetic trap platform", *Applied Physics Letters* **2005**, *86*, 243901.

[47] G. Vieira, A. Chen, T. Henighan, J. Lucy, F. Yang, R. Sooryakumar, "Transport of magnetic microparticles via tunable stationary magnetic traps in patterned wires", *Physical Review B* **2012**, *85*, 174440.

[48] A. Sarella, A. Torti, M. Donolato, M. Pancaldi, P. Vavassori, "Two-Dimensional Programmable Manipulation of Magnetic Nanoparticles on-Chip", *Advanced Materials* **2014**, *26*, 2384–2390.

[49] S. Floyd, C. Pawashe, M. Sitti in Intelligent Robots and Systems, 2009. IROS 2009. IEEE/RSJ International Conference on, IEEE, **2009**, pp. 528–533.

[50] C. Lee, H. Lee, R. Westervelt, "Microelectromagnets for the control of magnetic nanoparticles", *Applied physics letters* **2001**, *79*, 3308–3310.

[51] P. Rinklin, H.-J. Krause, B. Wolfrum, "Actuation and tracking of a single magnetic particle on a chip", *Applied physics letters* **2012**, *100*, 014107.

[52] B. Senyuk, M. C. Varney, J. A. Lopez, S. Wang, N. Wu, I. I. Smalyukh, "Magnetically responsive gourd-shaped colloidal particles in cholesteric liquid crystals", *Soft Matter* **2014**, *10*, 6014–6023.

[53] U. K. Cheang, D. Roy, J. H. Lee, M. J. Kim, "Fabrication and magnetic control of bacteria-inspired robotic microswimmers", *Applied Physics Letters* **2010**, *97*, 213704.

[54] W. Gao, K. M. Manesh, J. Hua, S. Sattayasamitsathit, J. Wang, "Hybrid nanomotor: A catalytically/magnetically powered adaptive nanowire swimmer", *Small* **2011**, *7*, 2047–2051.

[55] P. Garstecki, M. Cieplak, "Swimming at low Reynolds numbers—motility of micro-organisms", *Journal of Physics: Condensed Matter* **2009**, *21*, 200301.

[56] T. Honda, K. Arai, K. Ishiyama, "Micro swimming mechanisms propelled by external magnetic fields", *IEEE Transactions on Magnetics* **1996**, *32*, 5085–5087.

[57] H. Lamb, *Hydrodynamics*, Cambridge university press, **1932**.

[58] T. Zhu, D. J. Lichlyter, M. A. Haidekker, L. Mao, "Analytical model of microfluidic transport of non-magnetic particles in ferrofluids under the influence of a permanent magnet", *Microfluidics and Nanofluidics* **2011**, *10*, 1233–1245.

[59] L. Zhang, J. J. Abbott, L. Dong, B. E. Kratochvil, D. Bell, B. J. Nelson, "Artificial bacterial flagella: Fabrication and magnetic control", *Applied Physics Letters* **2009**, *94*, 064107.

[60] L. Zhang, K. E. Peyer, B. J. Nelson, "Artificial bacterial flagella for micromanipulation", *Lab on a Chip* **2010**, *10*, 2203–2215.

[61] H. Choi, K. Cha, J. Choi, S. Jeong, S. Jeon, G. Jang, J.-o. Park, S. Park, "EMA system with gradient and uniform saddle coils for 3D locomotion of microrobot", *Sensors and Actuators A: Physical* **2010**, *163*, 410–417.

[62] W. Gao, S. Sattayasamitsathit, K. M. Manesh, D. Weihs, J. Wang, "Magnetically powered flexible metal nanowire motors", *Journal of the American Chemical Society* **2010**, *132*, 14403–14405.

[63] R. Dreyfus, J. Baudry, M. L. Roper, M. Fermigier, H. A. Stone, J. Bibette, "Microscopic artificial swimmers", *Nature* **2005**, *437*, 862–865.

[64] E. Lauga, T. R. Powers, "The hydrodynamics of swimming microorganisms", *Reports on Progress in Physics* **2009**, *72*, 096601.

[65] S. Tottori, L. Zhang, F. Qiu, K. K. Krawczyk, A. Franco-Obregón, B. J. Nelson, "Magnetic helical micromachines: fabrication, controlled swimming, and cargo transport", *Advanced materials* **2012**, *24*, 811–816.

[66] J. M. Yeomans, D. O. Pushkin, H. Shum, "An introduction to the hydrodynamics of swimming microorganisms", *The European Physical Journal Special Topics* **2014**, *223*, 1771–1785.

[67] M. Silverman, M. Simon, "Flagellar rotation and the mechanism of bacterial motility", *Nature* **1974**, *249*, 73–74.

[68] J. Happel, H. Brenner, *Low Reynolds number hydrodynamics: with special applications to particulate media*, *Vol. 1*, Springer Science & Business Media, **2012**.

[69] C. E. Sing, L. Schmid, M. F. Schneider, T. Franke, A. Alexander-Katz, "Controlled surface-induced flows from the motion of self-assembled colloidal walkers", *Proceedings of the National Academy of Sciences* **2010**, *107*, 535–540.

[70] P. McCarty, W. Horsthemke, "Effective diffusion coefficient for steady two-dimensional convective flow", *Physical Review A* **1988**, *37*, 2112.

[71] D. F. Calef, J. Deutch, "Diffusion-controlled reactions", *Annual Review of Physical Chemistry* **1983**, *34*, 493–524.

[72] A. T. Chwang, T. Y.-T. Wu, "Hydromechanics of low-Reynolds-number flow. Part 2. Singularity method for Stokes flows", *Journal of Fluid Mechanics* **1975**, *67*, 787–815.

[73] A. A. Noyes, W. R. Whitney, "The rate of solution of solid substances in their own solutions.", *Journal of the American Chemical Society* **1897**, *19*, 930–934.

[74] J. Méndez, A. Monteagudo, K. Griebenow, "Stimulus-responsive controlled release system by covalent immobilization of an enzyme into mesoporous silica nanoparticles", *Bioconjugate chemistry* **2012**, *23*, 698–704.

[75] J. Lu, E. Choi, F. Tamanoi, J. I. Zink, "Light-Activated Nanoimpeller-Controlled Drug Release in Cancer Cells", *Small* **2008**, *4*, 421–426.

[76] C. W. Song, R. Griffin, H. J. Park in *Cancer drug resistance*, Springer, **2006**, pp. 21–42.

[77] K. H. Min, J.-H. Kim, S. M. Bae, H. Shin, M. S. Kim, S. Park, H. Lee, R.-W. Park, I.-S. Kim, K. Kim, et al., "Tumoral acidic pH-responsive MPEG-poly (β-amino ester) polymeric micelles for cancer targeting therapy", *Journal of Controlled Release* **2010**, *144*, 259–266.

[78] M. Talelli, M. Iman, A. K. Varkouhi, C. J. Rijcken, R. M. Schiffelers, T. Etrych, K. Ulbrich, C. F. van Nostrum, T. Lammers, G. Storm, et al., "Core-crosslinked polymeric micelles with controlled release of covalently entrapped doxorubicin", *Biomaterials* **2010**, *31*, 7797–7804.

[79] C. Chang, H. Wei, C.-Y. Quan, Y.-Y. Li, J. Liu, Z.-C. Wang, S.-X. Cheng, X.-Z. Zhang, R.-X. Zhuo, "Fabrication of thermosensitive PCL-PNIPAAm-PCL triblock copolymeric micelles for drug delivery", *Journal of Polymer Science Part A: Polymer Chemistry* **2008**, *46*, 3048–3057.

[80] R. A. Siegel, M. J. Rathbone in *Fundamentals and Applications of Controlled Release Drug Delivery*, Springer, **2012**, pp. 19–43.

[81] C. G. Varelas, D. G. Dixon, C. A. Steiner, "Zero-order release from biphasic polymer hydrogels", *Journal of controlled release* **1995**, *34*, 185–192.

[82] H. Maeda, M. Brandon, A. Sano, "Design of controlled-release formulation for ivermectin using silicone", *International journal of pharmaceutics* **2003**, *261*, 9–19.

[83] M. E. Zugasti, A. Zornoza, M. del Mar Goñi, J. R. Isasi, I. Vélaz, C. Martin, M. Sánchez, M. C. Martinez-Ohárriz, "Influence of soluble and insoluble cyclodextrin polymers on drug release from hydroxypropyl methylcellulose tablets", *Drug development and industrial pharmacy* **2009**, *35*, 1264–1270.

[84] R. K. Malcolm, A. D. Woolfson, C. F. Toner, R. J. Morrow, S. D. McCullagh, "Long-term, controlled release of the HIV microbicide TMC120 from silicone elastomer vaginal rings", *Journal of Antimicrobial Chemotherapy* **2005**, *56*, 954–956.

[85] D. Sahana, G. Mittal, V. Bhardwaj, M. Kumar, "PLGA nanoparticles for oral delivery of hydrophobic drugs: influence of organic solvent on nanoparticle formation and release behavior in vitro and in vivo using estradiol as a model drug", *Journal of pharmaceutical sciences* **2008**, *97*, 1530–1542.

[86] A. A. Aimetti, A. J. Machen, K. S. Anseth, "Poly (ethylene glycol) hydrogels formed by thiol-ene photopolymerization for enzyme-responsive protein delivery", *Biomaterials* **2009**, *30*, 6048–6054.

[87] S. Kitazawa, I. Johno, Y. Ito, S. Teramura, J. Okada, "Effects of hardness on the disintegration time and the dissolution rate of uncoated caffeine tablets", *Journal of Pharmacy and Pharmacology* **1975**, *27*, 765–770.

[88] S. Kitazawa, I. Johno, T. Minouchi, J. Okada, "Interpretation of dissolution rate data from in vitro testing of compressed tablets", *Journal of Pharmacy and Pharmacology* **1977**, *29*, 453–459.

[89] M. Gibaldi, D. Perrier, Pharmacokinetics (Drugs and the pharmaceutical sciences), 2nd edn, vol. 15, **1982**.

[90] A. Hixson, J. Crowell, "Dependence of reaction velocity upon surface and agitation", *Industrial & Engineering Chemistry* **1931**, *23*, 1160–1168.

[91] R. W. Korsmeyer, R. Gurny, E. Doelker, P. Buri, N. A. Peppas, "Mechanisms of solute release from porous hydrophilic polymers", *International journal of pharmaceutics* **1983**, *15*, 25–35.

[92] F. Langenbucher, "Linearization of dissolution rate curves by the Weibull distribution", *Journal of Pharmacy and Pharmacology* **1972**, *24*, 979–981.

[93] T. Higuchi, "Rate of release of medicaments from ointment bases containing drugs in suspension", *Journal of pharmaceutical sciences* **1961**, *50*, 874–875.

[94] D. R. Paul, F. W. Harris, *Controlled release polymeric formulations*, ACS Publications, **1976**.

[95] T. Seki, T. Kawaguchi, H. Endoh, K. Ishikawa, K. Juni, M. Nakano, "Controlled release of 3, 5-diester prodrugs of 5-fluoro-2-deoxyuridine from poly-L-lactic acid microspheres", *Journal of pharmaceutical sciences* **1990**, *79*, 985–987.

[96] B. Ren, A. Ruditskiy, J. H. Song, I. Kretzschmar, "Assembly behavior of iron oxide-capped Janus particles in a magnetic field", *Langmuir* **2011**, *28*, 1149–1156.

[97] A. Ghosh, P. Fischer, "Controlled propulsion of artificial magnetic nanostructured propellers", *Nano letters* **2009**, *9*, 2243–2245.

[98] Y.-P. Zhao, S.-H. Li, S. Chaney, S. Shanmukh, J.-G. Fan, R. Dluhy, W. Kisaalita, "Designing nanostructures for sensor applications", *Journal of electronic materials* **2006**, *35*, 846–851.

[99] S. Larson, W. Huang, Y. Zhao, "Combinatorial fabrication of composite nanorods using oblique angle co-deposition", *Nanotechnology* **2016**, *27*, 365304.

[100] S. Sheng-Nan, W. Chao, Z. Zan-Zan, H. Yang-Long, S. S. Venkatraman, X. Zhi-Chuan, "Magnetic iron oxide nanoparticles: Synthesis and surface coating techniques for biomedical applications", *Chinese Physics B* **2014**, *23*, 037503.

[101] W. Qin, C. Yang, R. Yi, G. Gao, "Hydrothermal synthesis and characterization of single-crystalline α-Fe 2 O 3 nanocubes", *Journal of Nanomaterials* **2011**, *2011*, 3.

[102] W. Zhang, L. Gai, Z. Li, H. Jiang, W. Ma, "Low temperature hydrothermal synthesis of octahedral Fe3O4 microcrystals", *Journal of Physics D: Applied Physics* **2008**, *41*, 225001.

[103] D. Kagan, R. Laocharoensuk, M. Zimmerman, C. Clawson, S. Balasubramanian, D. Kang, D. Bishop, S. Sattayasamitsathit, L. Zhang, J. Wang, "Rapid delivery of drug carriers propelled and navigated by catalytic nanoshuttles", *Small* **2010**, *6*, 2741–2747.

[104] I. Paprotny, S. Bergbreiter, *Small-Scale Robotics From Nano-to-Millimeter-Sized Robotic Systems and Applications: First International Workshop, microICRA 2013, Karlsruhe, Germany, May 6-10, 2013, Revised and Extended Papers*, *Vol. 8336*, Springer, **2014**.

[105] J. Hu, W. Huang, S. Huang, Q. ZhuGe, K. Jin, Y. Zhao, "Magnetically active Fe3O4 nanorods loaded with tissue plasminogen activator for enhanced thrombolysis", *Nano Research* **2016**, *9*, 2652–2661.

[106] R. Cheng, W. Huang, L. Huang, B. Yang, L. Mao, K. Jin, Q. ZhuGe, Y. Zhao, "Acceleration of tissue plasminogen activator-mediated thrombolysis by magnetically powered nanomotors", *ACS nano* **2014**, *8*, 7746–7754.

[107] W.-M. Zhang, X.-L. Wu, J.-S. Hu, Y.-G. Guo, L.-J. Wan, "Carbon Coated Fe3O4 Nanospindles as a Superior Anode Material for Lithium-Ion Batteries", *Advanced Functional Materials* **2008**, *18*, 3941–3946.

[108] Y. He, J. Fu, Y. Zhang, Y. Zhao, L. Zhang, A. Xia, J. Cai, "Multilayered Si/Ni nanosprings and their magnetic properties", *Small* **2007**, *3*, 153–160.

[109] G. K. Larsen, Y. He, W. Ingram, Y. Zhao, "Hidden chirality in superficially racemic patchy silver films", *Nano letters* **2013**, *13*, 6228–6232.

[110] J. G. Gibbs, N. A. Fragnito, Y. Zhao, "Asymmetric Pt/Au coated catalytic micromotors fabricated by dynamic shadowing growth", *Applied Physics Letters* **2010**, *97*, 253107.

[111] R. M. Erb, J. J. Martin, R. Soheilian, C. Pan, J. R. Barber, "Actuating Soft Matter with Magnetic Torque", *Advanced Functional Materials* **2016**, *26*, 3859–3880.

[112] B. J. Kirby, *Micro-and nanoscale fluid mechanics: transport in microfluidic devices*, Cambridge University Press, **2010**.

[113] S. A. Khashan, E. P. Furlani, "Effects of particle–fluid coupling on particle transport and capture in a magnetophoretic microsystem", *Microfluidics and nanofluidics* **2012**, *12*, 565–580.

[114] Y.-P. Zhao, D.-X. Ye, G.-C. Wang, T.-M. Lu, "Novel nano-column and nano-flower arrays by glancing angle deposition", *Nano Letters* **2002**, *2*, 351–354.

[115] D. Collen, H. R. Lijnen, "The tissue-type plasminogen activator story", *Arteriosclerosis thrombosis and vascular biology* **2009**, *29*, 1151–1155.

[116] A. Kaplan, F. Castellino, D. Collen, B. Wiman, F. Taylor Jr, "Molecular mechanisms of fibrinolysis in man.", *Thrombosis and haemostasis* **1978**, *39*, 263–283.

[117] D. Collen in Therapie, *Vol. 43*, **1988**, pp. 69–69.

[118] D. Collen, "Molecular mechanisms of fibrinolysis and their application to fibrin-specific thrombolytic therapy", *Journal of cellular biochemistry* **1987**, *33*, 77–86.

[119] G. Cesarman-Maus, K. A. Hajjar, "Molecular mechanisms of fibrinolysis", *British journal of haematology* **2005**, *129*, 307–321.

[120] F. Sagues, W. Horsthemke, "Diffusive transport in spatially periodic hydrodynamic flows", *Physical Review A* **1986**, *34*, 4136.

[121] H. Danan, A. Herr, A. Meyer, "New determinations of the saturation magnetization of nickel and iron", *Journal of Applied Physics* **1968**, *39*, 669–670.

[122] J. Rojo, A. Hernando, M. El Ghannami, A. Garcia-Escorial, M. Gonzalez, R. Garcia-Martinez, L. Ricciarelli, "Observation and characterization of ferromagnetic amorphous nickel", *Physical review letters* **1996**, *76*, 4833.

[123] E. B. André, R. I. Litvinov, D. E. Discher, J. W. Weisel, "Forced unfolding of coiled-coils in fibrinogen by single-molecule AFM", *Biophysical journal* **2007**, *92*, L39–L41.

[124] J.-P. Collet, H. Shuman, R. E. Ledger, S. Lee, J. W. Weisel, "The elasticity of an individual fibrin fiber in a clot", *Proceedings of the National Academy of Sciences of the United States of America* **2005**, *102*, 9133–9137.

[125] A. Radomski, P. Jurasz, D. Alonso-Escolano, M. Drews, M. Morandi, T. Malinski, M. W. Radomski, "Nanoparticle-induced platelet aggregation and vascular thrombosis.", *British journal of pharmacology* **2005**, *146*, 882–893.

[126] R. M. Cornell, U. Schwertmann, *The iron oxides: structure, properties, reactions, occurrences and uses*, John Wiley & Sons, **2003**.

[127] H. Lu, W. Zheng, Q. Jiang, "Saturation magnetization of ferromagnetic and ferrimagnetic nanocrystals at room temperature", *Journal of Physics D: Applied Physics* **2007**, *40*, 320.

[128] W. Hacke, M. Kaste, E. Bluhmki, M. Brozman, A. Dávalos, D. Guidetti, V. Larrue, K. R. Lees, Z. Medeghri, T. Machnig, et al., "Thrombolysis with alteplase 3 to 4.5 hours after acute ischemic stroke", *New England Journal of Medicine* **2008**, *359*, 1317–1329.

[129] P. W. Armstrong, D. Collen, "Fibrinolysis for acute myocardial infarction", *Circulation* **2001**, *103*, 2987–2992.

[130] W. Chandler, M. Alessi, M. Aillaud, P. Henderson, P. Vague, I. Juhan-Vague, "Clearance of tissue plasminogen activator (TPA) and TPA/plasminogen activator inhibitor type 1 (PAI-1) complex", *Circulation* **1997**, *96*, 761–768.

[131] H. A. Cameron, B. S. McEwen, E. Gould, "Regulation of adult neurogenesis by excitatory input and NMDA receptor activation in the dentate gyrus", *Journal of Neuroscience* **1995**, *15*, 4687–4692.

[132] J.-P. Chen, P.-C. Yang, Y.-H. Ma, T. Wu, "Characterization of chitosan magnetic nanoparticles for in situ delivery of tissue plasminogen activator", *Carbohydrate Polymers* **2011**, *84*, 364–372.

[133] S. L. Diamond, "Engineering design of optimal strategies for blood clot dissolution", *Annual review of biomedical engineering* **1999**, *1*, 427–461.

[134] C. Pleydell, T. David, S. Smye, D. Berridge, "A mathematical model of post-canalization thrombolysis", *Physics in medicine and biology* **2002**, *47*, 209.

Appendix A

Cluster Tracking Program

Experimental videos of moving MCs in this dissertation have been analyzed using a lab-developed Matlab object tracking program. Most of the core algorithms used in this program are provided by the Matlab's Computer Vision Toolbox. The basic work flow of this program is described below:

1. Read movie frame if movie has not ended.

2. Convert frame into Lab color space and use the threshold method to obtain a black-white mask with clusters showing in write color, background showing in black color. Threshold value is different from movies and must be given when calling *ClustersTracking* function.

3. Perform blob analysis to find connected white pixels (clusters) that larger than certain size.

4. Compute the distance between the clusters in current frame and last frame. Store the distance in a cost matrix.

5. If the minimal of the cost is smaller than certain threshold, assign these two clusters with same tracker ID. Otherwise, initiate a new tracker.

6. Delete the lost trackers and move back to **Step 1**.

Information such as the center coordinate, the width, and the height of each cluster will be extracted. **Figure A.1(a)** shows an example frame of the processed experiment video. We placed the magnetic solenoid on the right-hand side. The frequency of driven field $f_H = 5\,\mathrm{Hz}$ and this video was recorded at 200 fps. After turned on the magnetic field, we observed that

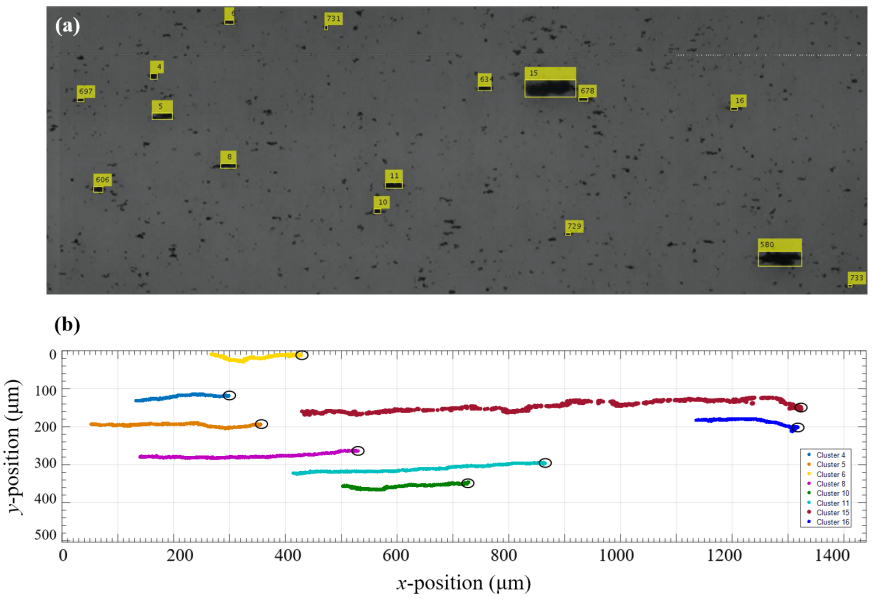

Figure A.1: (a) The example of a tracked movie frame with a $f_H = 5\,\mathrm{Hz}$, $I_0 = 2\,\mathrm{A}$ driven field. (b) Tracked trajectories for selected clusters. The black circle marks the initial position.

almost all clusters moved from right to the left side with different speed. Clusters larger than certain threshold size ($40\,\mu\mathrm{m}^2$ for current experiment setup) was recognized by our tracking program and assigned with a unique track ID. The yellow frame box indicates the width and height of each tracked cluster. Trajectories of selected clusters are shown in **Figure A.1(b)** with black circles marking their initial positions.

Listing A.1: Source code for clusters tracking

```
%% Motion-Based Multiple Object Tracking
function ClustersTracking(videoname, th)
    obj = setupSystemObjects(videoname);
    % Create an empty array of tracks.
    tracks = initializeTracks();
    % ID of the next track
    nextId = 1;
    % Save the results. (tracker ID, frame#, [1,2: x,y position. 3: cluster
   area. 4,5: W,H box size])
    Results = zeros(1,1,5);
```

```
    CurrentFrame = 0;
    % Detect moving objects, and track them across video frames.
    while ~isDone(obj.reader)
        frame = readFrame();
        CurrentFrame=CurrentFrame+1;
        Results(:,CurrentFrame,:) = zeros;
        [~,centroids, bboxes, mask] = detectObjects(frame);
        predictNewLocationsOfTracks();
        [assignments, unassignedTracks, unassignedDetections] = ...
            detectionToTrackAssignment();
        updateAssignedTracks();
        updateUnassignedTracks();
        deleteLostTracks();
        createNewTracks();
        displayTrackingResults();
    end
    close(obj.Result_out);
    close(obj.Mask_out);

%% Create System Objects
% Create System objects used for reading the video frames, detecting
   foreground objects, and displaying results.
    function obj = setupSystemObjects(fname)
        % Initialize Video I/O
        % Create objects for reading a video from a file, drawing the tracked
   objects in each frame, and playing the video.
        obj.reader = vision.VideoFileReader(fname,'ImageColorSpace','RGB','
   VideoOutputDataType','uint8');

        % Create two video players, one to display the video, and one to
   display the foreground mask.
```

```
        obj.videoPlayer = vision.VideoPlayer('Position', [20, 400, 700, 400]);
        obj.maskPlayer = vision.VideoPlayer('Position', [740, 400, 700, 400]);
        fn=strsplit(char(fname),'.');
        res_out = strcat(char(fn(1)),'_Result.',char(fn(2)));
        msk_out = strcat(char(fn(1)),'_Mask.',char(fn(2)));
        obj.Result_out = VideoWriter(res_out,'Motion JPEG AVI');
        obj.Mask_out = VideoWriter(msk_out,'Motion JPEG AVI');
        obj.Result_out.FrameRate = 20;
        obj.Mask_out.FrameRate = 20;
        open(obj.Result_out);
        open(obj.Mask_out);
        obj.blobAnalyser = vision.BlobAnalysis(...
            'BoundingBoxOutputPort', true, ...
            'AreaOutputPort', true, 'CentroidOutputPort', true, ...
            'MinimumBlobArea', 15, 'MaximumCount', 150);
    end

%% Initialize Tracks
    function tracks = initializeTracks()
        % create an empty array of tracks
        tracks = struct(...
            'id', {}, ...
            'bbox', {}, ...
            'kalmanFilter', {}, ...
            'age', {}, ...
            'totalVisibleCount', {}, ...
            'consecutiveInvisibleCount', {});
    end

% Read the next video frame from the video file.
    function frame = readFrame()
```

```
        frame = obj.reader.step();
    end

%% Detect Objects
    function [area, centroids, bboxes, mask] = detectObjects(frame)
        % Detect foreground.
        % Convert RGB image to chosen color space.
        RGB = im2double(frame);
        cform = makecform('srgb2lab', 'AdaptedWhitePoint', whitepoint('D65'));
        I = applycform(RGB,cform);
        % Define thresholds for channel 1 based on histogram settings.
        channel1Min = th;
        channel1Max = 100.000;
        % Create mask based on chosen histogram thresholds.
        mask = ~((I(:,:,1) >= channel1Min ) & (I(:,:,1) <= channel1Max));
        % Apply morphological operations to remove noise and fill in holes.
        mask = imfill(mask, 'holes');
        mask = imclearborder(mask);
        mask = imopen(mask, strel('square', 3));
        % Perform blob analysis to find connected components.
        [area, centroids, bboxes] = obj.blobAnalyser.step(mask);
    end

%% Predict New Locations of Existing Tracks
% Use the Kalman filter to predict the centroid of each track in the current
   frame, and update its bounding box accordingly.
    function predictNewLocationsOfTracks()
        for i = 1:length(tracks)
            bbox = tracks(i).bbox;
            % Predict the current location of the track.
            predictedCentroid = predict(tracks(i).kalmanFilter);
```

```
            % Shift the bounding box so that its center is at the predicted
    location.
            predictedCentroid = int32(predictedCentroid) - bbox(3:4) / 2;
            tracks(i).bbox = [predictedCentroid, bbox(3:4)];
        end
    end

%% Assign Detections to Tracks
    function [assignments, unassignedTracks, unassignedDetections] = ...
            detectionToTrackAssignment()
        nTracks = length(tracks);
        nDetections = size(centroids, 1);
        % Compute the cost of assigning each detection to each track.
        cost = zeros(nTracks, nDetections);
        for i = 1:nTracks
            cost(i, :) = distance(tracks(i).kalmanFilter, centroids);
        end
        % Solve the assignment problem.
        costOfNonAssignment = 20;
        [assignments, unassignedTracks, unassignedDetections] = ...
            assignDetectionsToTracks(cost, costOfNonAssignment);
    end

%% Update Assigned Tracks
    function updateAssignedTracks()
        numAssignedTracks = size(assignments, 1);
        for i = 1:numAssignedTracks
            trackIdx = assignments(i, 1);
            detectionIdx = assignments(i, 2);
            centroid = centroids(detectionIdx, :);
            bbox = bboxes(detectionIdx, :);
```

```
            % Correct the estimate of the object's location using the new
    detection.
            correct(tracks(trackIdx).kalmanFilter, centroid);
            % Replace predicted bounding box with detected bounding box.
            tracks(trackIdx).bbox = bbox;
            % Update track's age.
            tracks(trackIdx).age = tracks(trackIdx).age + 1;
            % Update visibility.
            tracks(trackIdx).totalVisibleCount = ...
                tracks(trackIdx).totalVisibleCount + 1;
            tracks(trackIdx).consecutiveInvisibleCount = 0;
        end
    end

%% Update Unassigned Tracks
% Mark each unassigned track as invisible, and increase its age by 1.
    function updateUnassignedTracks()
        for i = 1:length(unassignedTracks)
            ind = unassignedTracks(i);
            tracks(ind).age = tracks(ind).age + 1;
            tracks(ind).consecutiveInvisibleCount = ...
                tracks(ind).consecutiveInvisibleCount + 1;
        end
    end

%% Delete Lost Tracks
    function deleteLostTracks()
        if isempty(tracks)
            return;
        end
        invisibleForTooLong = 5;
```

```
        ageThreshold = 10;
        % Compute the fraction of the track's age for which it was visible.
        ages = [tracks(:).age];
        totalVisibleCounts = [tracks(:).totalVisibleCount];
        visibility = totalVisibleCounts ./ ages;
        % Find the indices of 'lost' tracks.
        lostInds = (ages < ageThreshold & visibility < 0.7) | ...
            [tracks(:).consecutiveInvisibleCount] >= invisibleForTooLong;
        % Delete lost tracks.
        tracks = tracks(~lostInds);
    end

%% Create New Tracks
% Create new tracks from unassigned detections.
    function createNewTracks()
        centroids = centroids(unassignedDetections, :);
        bboxes = bboxes(unassignedDetections, :);
        for i = 1:size(centroids, 1)
            centroid = centroids(i,:);
            bbox = bboxes(i, :);
            % Create a Kalman filter object.
            kalmanFilter = configureKalmanFilter('ConstantVelocity', ...
                centroid, [5, 2], [5, 2], 3);
            % Create a new track.
            newTrack = struct(...
                'id', nextId, ...
                'bbox', bbox, ...
                'kalmanFilter', kalmanFilter, ...
                'age', 1, ...
                'totalVisibleCount', 1, ...
                'consecutiveInvisibleCount', 0);
```

```
            % Add it to the array of tracks.
            tracks(end + 1) = newTrack;
            % Increment the next id.
            nextId = nextId + 1;
        end
    end

%% Display Tracking Results
    function displayTrackingResults()
        % Convert the frame and the mask to uint8 RGB.
        frame = im2uint8(frame);
        mask = uint8(repmat(mask, [1, 1, 3])) .* 255;
        minVisibleCount = 8;
        if ~isempty(tracks)
            % Noisy detections tend to result in short-lived tracks.
            % Only display tracks that have been visible for more than a
   minimum number of frames.
            reliableTrackInds = [tracks(:).totalVisibleCount] >
   minVisibleCount;
            reliableTracks = tracks(reliableTrackInds);
            % Display the objects. If an object has not been detected in this
   frame, display its predicted bounding box.
            if ~isempty(reliableTracks)
                % Get bounding boxes.
                bboxes = cat(1, reliableTracks.bbox);
                % Get ids.
                ids = int32([reliableTracks(:).id]);
                Results(ids,CurrentFrame,1) = bboxes(:,1)+bboxes(:,3)/2;
                Results(ids,CurrentFrame,2) = bboxes(:,2)+bboxes(:,4)/2;
                Results(ids,CurrentFrame,4) = bboxes(:,3);
                Results(ids,CurrentFrame,5) = bboxes(:,4);
```

```
                % Create labels for objects indicating the ones for which we
    display the predicted rather than the actual location.
                labels = cellstr(int2str(ids'));
                predictedTrackInds = [reliableTracks(:).
    consecutiveInvisibleCount] > 0;
                isPredicted = cell(size(labels));
                isPredicted(predictedTrackInds) = {' predicted'};
                labels = strcat(labels, isPredicted);
                % Draw the objects on the frame.
                frame = insertObjectAnnotation(frame, 'rectangle', ...
                    bboxes, labels);
                % Draw the objects on the mask.
                mask = insertObjectAnnotation(mask, 'rectangle', ...
                    bboxes, labels,'Color', 'cyan');
            end
        end
        assignin('base','Result',Results);
        % Display and save the mask and the frame.
        obj.maskPlayer.step(mask);
        writeVideo(obj.Mask_out,mask);
        obj.videoPlayer.step(frame);
        writeVideo(obj.Result_out,frame);
    end
end
```

Appendix B

Manipulation by Keyboards

The manipulation system is consisted of a computer with multi-channel sound card, two dual channel power amplifiers and 4 solenoids placed in 4 directions as shown in **Figure B.1**. A Matlab program which can detect the keyboard key press and generate strings of low frequency (5 - 100 Hz) sound signals is running on the computer. Based on the key that the user is pressed, the computer would output a sinusoidal signal with a fixed frequency (input value) through different sound output channels. For example, when the "w" key is being pressed, the motion control program will generate sinusoidal signals through the output channel responsible for the up movement. And when the key is released, the sinusoidal signal is terminated. In another word, the amplified sinusoidal signal are used to drive the solenoid placed at the bottom. The flow chart of the motion control program is shown in **Figure B.2**. The source code for *motioncontrol.m* is shown below. It requires Matlab's Data Acquisition Toolbox and appropriate sound card driver in order to run.

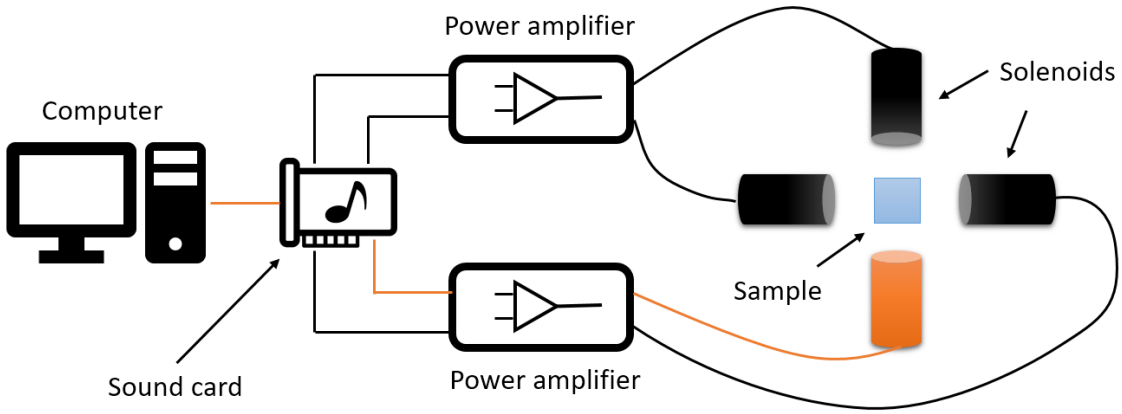

Figure B.1: Illustration of motion control system. Orange color marks the components that are activated when user press 'Up' key.

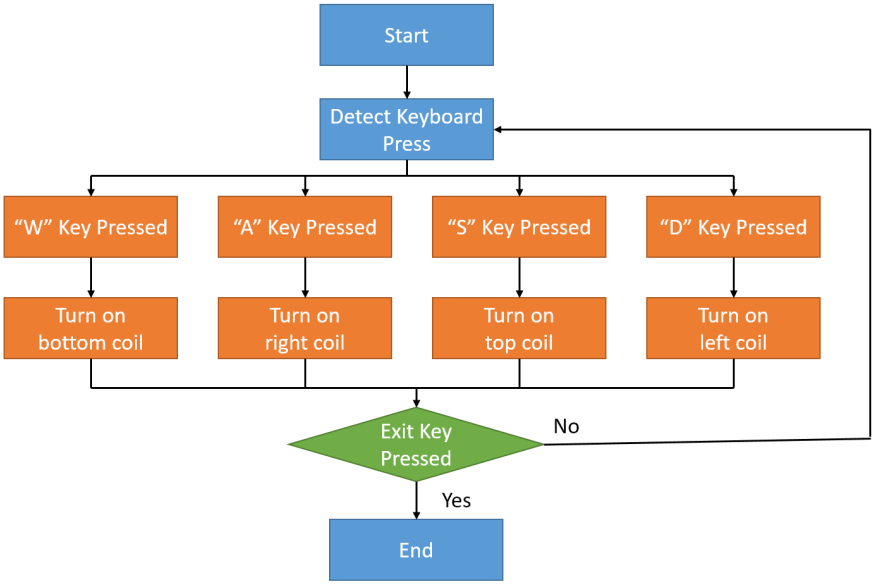

Figure B.2: The flow chart of motion control program.

Listing B.1: Source code for keyboard motion control

```
function varargout = MotionControl(varargin)
% Begin initialization code - DO NOT EDIT
gui_Singleton = 1;
gui_State = struct('gui_Name',       mfilename, ...
                   'gui_Singleton',  gui_Singleton, ...
                   'gui_OpeningFcn', @MotionControl_OpeningFcn, ...
                   'gui_OutputFcn',  @MotionControl_OutputFcn, ...
                   'gui_LayoutFcn',  [] , ...
                   'gui_Callback',   []);
if nargin && ischar(varargin{1})
    gui_State.gui_Callback = str2func(varargin{1});
end
if nargout
    [varargout{1:nargout}] = gui_mainfcn(gui_State, varargin{:});
else
    gui_mainfcn(gui_State, varargin{:});
```

```
end
% End initialization code - DO NOT EDIT

% --- Executes just before MotionControl is made visible.
function MotionControl_OpeningFcn(hObject, eventdata, handles, varargin)
% This function has no output args, see OutputFcn.
% hObject    handle to figure
% eventdata  reserved - to be defined in a future version of MATLAB
% handles    structure with handles and user data (see GUIDATA)
% varargin   command line arguments to MotionControl (see VARARGIN)

% Choose default command line output for MotionControl
handles.output = hObject;

duration = 30;
fs = 8192;
frequency = 10;
t = 0:1/fs:duration;
mask = sin(2*pi*frequency*t);
s = daq.createSession('directsound');
noutchan = 4;
addAudioOutputChannel(s, 'Audio7', 1:noutchan);
s.Rate = fs;

up_sound(:,1) = mask;
up_sound(:,2) = 0;
up_sound(:,3) = 0;
up_sound(:,4) = 0;
right_sound(:,2) = mask;
right_sound(:,3) = 0;
right_sound(:,4) = 0;
```

```
left_sound(:,3) = mask;
left_sound(:,4) = 0;
down_sound(:,4) = mask;

handles.sound_device = s;
handles.up_sound = up_sound;
handles.right_sound = right_sound;
handles.left_sound = left_sound;
handles.down_sound = down_sound;
handles.keyhold = 0;
% Update handles structure
guidata(hObject, handles);

% UIWAIT makes MotionControl wait for user response (see UIRESUME)
% uiwait(handles.figure1);

% --- Outputs from this function are returned to the command line.
function varargout = MotionControl_OutputFcn(hObject, eventdata, handles)
% varargout  cell array for returning output args (see VARARGOUT);
% hObject    handle to figure
% eventdata  reserved - to be defined in a future version of MATLAB
% handles    structure with handles and user data (see GUIDATA)

% Get default command line output from handles structure
varargout{1} = handles.output;

% --- Executes on key press with focus on figure1 or any of its controls.
function figure1_WindowKeyPressFcn(hObject, eventdata, handles)
% hObject    handle to figure1 (see GCBO)
% eventdata  structure with the following fields (see MATLAB.UI.FIGURE)
%   Key: name of the key that was pressed, in lower case
```

```
%   Character: character interpretation of the key(s) that was pressed
%   Modifier: name(s) of the modifier key(s) (i.e., control, shift) pressed
% handles    structure with handles and user data (see GUIDATA)
if (handles.keyhold == 0)
    handles.keyhold = 1;
    guidata(hObject, handles);
    switch eventdata.Key
      case 'w'
           set(handles.text2, 'String', 'Up');
           queueOutputData(handles.sound_device, handles.up_sound);
           startBackground(handles.sound_device);
      case 'd'
           set(handles.text2, 'String', 'Right');
           queueOutputData(handles.sound_device, handles.right_sound);
           startBackground(handles.sound_device);
      case 'a'
           set(handles.text2, 'String', 'Left');
           queueOutputData(handles.sound_device, handles.left_sound);
           startBackground(handles.sound_device);
      case 's'
           set(handles.text2, 'String', 'Down');
           queueOutputData(handles.sound_device, handles.down_sound);
           startBackground(handles.sound_device);
    end
end


% --- Executes on key release with focus on figure1 or any of its controls.
function figure1_WindowKeyReleaseFcn(hObject, eventdata, handles)
% hObject    handle to figure1 (see GCBO)
% eventdata  structure with the following fields (see MATLAB.UI.FIGURE)
%   Key: name of the key that was released, in lower case
```

```
%   Character: character interpretation of the key(s) that was released
%   Modifier: name(s) of the modifier key(s) (i.e., control, shift) released
% handles    structure with handles and user data (see GUIDATA)
set(handles.text2, 'String', 'Stop');
handles.keyhold = 0;
guidata(hObject, handles);
stop(handles.sound_device);
```